

# **Carbon Nanotube/Polymer Composites: Kinetics, Stability and Applications for Biofuel Cells and Sensors**

By

William Cheung

A dissertation submitted to the

Graduate School-Newark

Rutgers, The State University of New Jersey

In partial fulfillment of the requirements

For the degree of

Doctor of Philosophy

Graduate Program in Chemistry

Written under the direction of

Professor Huixin He

And approved by

---

---

---

---

Newark, New Jersey

October 2012

©2012

William Cheung

ALL RIGHTS RESERVED

# **Abstract**

## **Carbon Nanotube/Polymer Composites: Kinetics, Stability and Applications in Biofuel Cells and Sensors**

**By William Cheung**

**Thesis Director:**

**Professor Huixin He**

It is well known that carbon nanotubes (CNT) exhibit remarkable electrical, mechanical and optical properties. In addition, conducting polymers have also been used for molecular sensors, electronic energy generation and storage devices due to their interesting electronic and electrochemical properties. In an effort to synergistically combine the advantages of both materials, conducting CNT/polymer composites have been fabricated. However, due to the highly hydrophobic surface and their strong intertube interactions, it is necessary to properly modify the carbon nanotube surface either covalently or non-covalently to prevent them from forming bundles and disperse them into solutions or polymer matrices to fabricate genuine polymer/CNT composites.

Blending pre-formed polymers with carbon nanotubes has been demonstrated to be the most straightforward approach to fabricate carbon nanotube composites. However, recent studies in our group have demonstrated that *in-situ* polymerization of the respective monomers in the presence of

dispersed and functionalized carbon nanotubes could form conducting polymer/CNT composites with much more enhanced functions. Different surface modification imparts carbon nanotubes with different electronic structures and surface chemistries. This can greatly impact the monomer/CNT interaction, and therefore influence the polymerization process and the CNT/polymer interaction after polymerization.

Extensive studies reported have shown that the enhanced functions of a composite are largely determined by the interactions between the polymer and the CNTs. Studies on the impact of electronic structure and surface chemistry on the monomer/CNT interaction and its subsequent effect on the polymerization kinetics as well as the quality of the formed composites are limited. These studies are essential for developing more efficient and green fabrication approaches of high quality composites with enhanced functions.

In this thesis, we will also systematically study how the surface chemistry and electronic structures of carbon nanotubes influence the electronic performance of carbon nanotube/conducting polymer composites and their stabilizing effect against UV degradation. The knowledge learned from these fundamental studies will be used to fabricate highly conductive and stable composites for constructing efficient biofuel cells. Along the same line, we will also study how the electronic structures of carbon nanotubes influence the development of sensitive and selective molecular detection devices.

Chapter 1 will be a general introduction to carbon nanotubes, their structure, properties, and surface chemistry. Conducting polymers such as polyaniline and their properties will also be introduced. The available approaches to fabricate conducting polymer/CNT composites, their application for biofuel cells, and the current issues of biofuel cells will be summarized. In this chapter electrical and optical approaches for molecule detections based on carbon nanotubes are also elaborated.

The aim of Chapter 2 is to systematically study how the electronic structure and surface chemistry of carbon nanotubes influence the kinetics of ABA polymerization. The electronic properties of CNTs will be altered through surface modification using double stranded DNA and single stranded DNA with different sequences. After surface modification, their effect on the polymerization process and the formed composites will be studied.

Chapter 3 will be focused on a detailed study of the stabilizing effects that carbon nanotubes have in self doped polyaniline composites. CNTs have been shown to mitigate the environmental degradation effects imposed on conducting polymers. This study is important for developing stable devices such as biofuel cells using conducting polymer composites. In this work, a new stabilization mechanism against UV irradiation will also be proposed.

Slow electron transfer rate is a fundamental problem that exists in biosensors and biological fuel cells. This is usually due to the lack or inefficient direct electron transfer between redox enzymes and the electrode support.

Chapter 4 applies the knowledge gained from chapters 2 and 3 to modify an electrode surface with highly conductive CNT/polymer composites to construct an efficient anode for a biofuel cell. Optimization was performed to realize direct electron transfer between the redox center of glucose oxidase and the electrode surface with a dramatic enhancement in electron transfer rate and glucose oxidation efficiency. Furthermore, the enzyme will be reconstructed onto the surface of the electrode in different orientations and their electrobiocatalytic oxidation of glucose will be studied.

In Chapter 5, the strong plasmon absorption of single walled carbon nanotubes (SWNTs) was explored to develop a new sensing platform for metallic ions. Compared to previously reported electronic and NIR fluorescence detection approaches, the new sensing platform can reach the same or better detection sensitivity and detection limits simply by using UV absorption spectroscopy. The detection sensitivity was studied using modified SWNTs with different electronic structures. The detection selectivity is realized by modifying the surface of SWNTs with molecular ligands with high specificity for metal ions. As a demonstration, the new method is applied to selectively detect iron ions ( $\text{Fe}^{3+}$ ) in aqueous solution.  $\text{Fe}^{3+}$  was chosen because it is an essential element for the growth and metabolism of all marine organisms. Therefore the ability to selectively and sensitively detection  $\text{Fe}^{3+}$  is critical to study of carbon sequestration in the ocean and consequently climate change.

Chapter 6 is a preliminary study on how the electronic structures of SWNTs can influence its Raman scattering properties, which in turn influence

their sensitivity for the detection of cancer cells and their capability to destroy them using NIR light radiation.

*Dedicated to family and  
friends*



## **Acknowledgements**

I would like to take this opportunity to offer my thanks to a number of people whose help and support have guided me through my graduate studies and who have made this possible.

First and foremost, I would like to thank my advisor Professor Huixin He for allowing me the opportunity to pursue my doctoral studies in the field of nanomaterials. I would also like to thank her for her unwavering support and guidance throughout my graduate studies.

I would also like to express my gratitude to Prof. Philip Huskey, Prof. Agostino Pietrangelo, and Prof. Chunsheng Wang for their time devoted to reading and correcting my thesis and their valuable suggestions.

I also would like thank Dr. Yufeng Ma and Dr. Shashidhar Ranganathan from Polestar Technology, and Dr. Yan Xiao from the National Institute of Standards and Technology for their collaboration, valuable discussions, and help on the biofuel cell project and cancer detection project, respectively.

I would also like to thank all the professors of the chemistry department for their help and their valuable knowledge imparted to me. In addition, I would like to thank all the staff members of the chemistry department for their assistance throughout my graduate studies. I would also like to thank the graduate students for their friendship and support, especially the current and former members of Prof. Huixin He's group. The memories that I have here will be with me forever.

Finally, I would like to express my appreciation to my family and friends for their continuous support and encouragement.

## List of Abbreviations

ABA	3-aminophenylboronic acid
AFM	Atomic Force Microscopy
ANI	aniline
APS	Ammonium persulfate
a.u.	Arbitrary units
°C	Celsius degree
cm	centimeter
CNT	Carbon nanotubes
CV	Cyclic Voltammetry
DFO	Deferoxamine
DNA	Deoxyribonucleic acid
dsDNA	double stranded DNA
EDC	1-ethyl-3-(3-dimethylaminopropyl)carbodiimide
EIS	Electrochemical Impedance Spectroscopy
FTIR	Fourier Transform Infrared Spectroscopy
KF	Potassium fluoride

mL	milliliters
$\mu$ A	microamps
$\mu$ M	micromolar
M	Molar
MES	2-(N-morpholino)ethanesulfonic acid
MD-SWNT	microwave dispersed SWNT
mV	millivolts
MWNT	Multi-walled carbon nanotubes
NHS	N-Hydroxysuccinimide
NIR	Near infrared
PABA	poly(aniline boronic acid)
PANI	Polyaniline
PRET	Plasmon resonance energy transfer
PBS	Phosphate buffered saline
PL-PEG	Phospholipid-Polyethylene glycol
S	Siemens
ssDNA	single stranded DNA

UV-Vis

Ultraviolet-Visible

V

Volts

# Table of Contents

<b>Abstract</b>	<b>ii</b>
<b>Acknowledgements</b>	<b>viii</b>
<b>List of Abbreviations</b>	<b>x</b>
<b>Table of Contents</b>	<b>xiii</b>
<b>List of Figures</b>	<b>xvii</b>
<b>List of Tables</b>	<b>xxiii</b>
<b><u>Chapter 1: Introduction</u></b>	<b>1</b>
<b>1.1 Carbon Nanomaterials</b>	<b>1</b>
<b>1.2 Carbon Nanotubes</b>	<b>2</b>
<b>1.3 Surface Engineering of Carbon Nanotubes</b>	<b>7</b>
<b>1.4 Conducting Conjugated Polymers</b>	<b>9</b>
<b>1.5 Polyaniline</b>	<b>12</b>
<b>1.6 Polyaniline Polymerization Mechanism</b>	<b>16</b>
<b>1.7 Self-Doped Polyaniline</b>	<b>21</b>
<b>1.8 Carbon Nanotube Composites</b>	<b>22</b>
<b>1.8.1. Polymerization Kinetics</b>	<b>22</b>
<b>1.8.2. Stabilization of polymers from degradation</b>	<b>24</b>
<b>1.9 Enzymatic Biofuel Cells</b>	<b>25</b>
<b>1.9.1. Types of biofuel cells</b>	<b>25</b>
<b>1.9.2. Types of enzymes used in enzymatic biofuel cells</b>	<b>26</b>
<b>1.9.3. Electron transfer pathways</b>	<b>27</b>
<b>1.9.4. Biofuel cell applications and problems</b>	<b>29</b>

1.9.4.1. Enzyme stability	30
1.9.4.2. Mass transfer	30
1.9.4.3. Enzyme immobilization and power density	31
1.10 Carbon nanotubes for molecular detection	33
1.10.1. Electronic and optical detection	33
1.10.2. Raman scattering of carbon nanotubes for molecular detection and imaging	36
1.11 Objective of Thesis	38
1.12 References	39
<b><u>Chapter 2: DNA Functionalized SWNTs as Molecular Catalytic Templates: DNA Sequence Dependent Catalytic Efficacy</u></b>	<b>47</b>
2.1 Introduction	47
2.2 Results and Discussion	52
2.2.1. Dispersion of carbon nanotubes	52
2.2.2. Monolayer formation of ABA on CNT surface	54
2.2.3. Polymerization kinetics of DNA-CNT/ABA	56
2.2.4. Origin of catalytic effect	65
2.2.4.1. Catalytic role of SWNT and DNA	65
2.2.4.1.1. Catalytic role of dsDNA and ssDNA	68
2.2.4.1.2. Catalytic role of metallic and semiconducting SWNT	69
2.2.4.1.3. Catalytic role of different sequence of DNA	76
2.2.4.2. Catalytic role of SWNT and MWNT	78
2.2.5. Quality of produced CNT-PABA composite	78
2.3 Conclusion	80
2.4 Experimental	82
2.5 References	85

<b><u>Chapter 3: DNA Functionalized SWNTs as Active Stabilizers: Enhanced Stability of Conducting Polymer Composites</u></b>	<b>89</b>
3.1 Introduction	89
3.2 Results and Discussion	93
3.2.1. Stabilization of PABA monitored using spectroscopic methods	93
3.2.2. Stabilization of PABA monitored using conductance measurements	98
3.2.3. Stabilization of PABA monitored using FTIR spectroscopy	100
3.2.4. Roles of ssDNA/SWNT in stabilization of PABA	103
3.2.4.1. UV absorber	103
3.2.4.2. Proposed stabilization mechanism	104
3.3 Conclusion	108
3.4 Experimental	109
3.5 References	113
 <b><u>Chapter 4: Doped Polyaniline/Carbon Nanotube Composite for Construction of Efficient Enzyme Based Biofuel Cells</u></b>	 <b>116</b>
4.1 Introduction	116
4.2 Results and Discussion	119
4.2.1. Fabrication, optimization, and characterization of composite modified electrodes for glucose oxidation	119
4.2.2. Glucose oxidation of reconstituted enzyme modified electrode	131
4.2.3. Glucose oxidation of enzyme immobilized MWNT arrays	135
4.2.4. Effect of enzyme orientation on glucose oxidation	139
4.3 Conclusion	142
4.4 Experimental	144
4.5 References	152



<b><u>Chapter 5: Carbon Nanotube Plasmon: Sensitive and selective detection of Fe (III)</u></b>	<b>155</b>
5.1 Introduction	155
5.2 Results and Discussion	158
5.2.1. DFO iron chelator	158
5.2.2. Preparation and characterization of PL-PEG-COOH/SWNT	160
5.2.3. Sensitive detection of Fe (III) using PL-PEG-COOH/SWNT/DFO complex	164
5.2.4. Proposed Mechanism	166
5.2.5. Detection of Fe (III) using MF-SWNT/DFO complex	167
5.2.6. Sensitive detection of Fe (III)	170
5.2.7. Fe (III) detection of natural rainwater	175
5.3 Conclusion	176
5.4 Experimental	177
5.5 References	183
 <b><u>Chapter 6: Enhanced Selective Detection and Destruction of Cancer Cells via a Noncovalent Functionalization Approach</u></b>	 <b>185</b>
6.1 Introduction	185
6.2 Results and Discussion	188
6.2.1. Functionalization effects on the electronic structure of SWNT	188
6.2.2. Effect of surface modification of SWNT on Raman	189
6.2.3. Raman intensity of anti-HER2/PEG-SWNT	192
6.2.4. Selective destruction of cancer cells	194
6.3 Conclusion	195
6.4 Experimental	197
6.5 References	200
Curriculum Vitae	201

## List of Figures

<b>Scheme 1.1.</b> Schematic representation of (a) SWNT and (b) MWNT (specific case shown is double walled carbon nanotube).....	<b>3</b>
<b>Figure 1.1.</b> The unrolled honeycomb lattice of a carbon nanotube. $n$ is the chiral angle and $L$ is the chiral vector.....	<b>5</b>
<b>Figure 1.2.</b> Scheme showing different ways of covalently functionalizing carbon nanotubes.....	<b>8</b>
<b>Figure 1.3.</b> Structures of various conjugated polymers.....	<b>10</b>
<b>Figure 1.4.</b> Various applications of conducting polymers.....	<b>11</b>
<b>Figure 1.5.</b> General structure of polyaniline.....	<b>12</b>
<b>Figure 1.6.</b> Different oxidation states of polyaniline.....	<b>14</b>
<b>Figure 1.7.</b> Polaron charge carrier formation by acid doping.....	<b>16</b>
<b>Figure 1.8.</b> Aniline polymerization mechanism using anilinium cation-radical as cationic initiator.....	<b>17</b>
<b>Figure 1.9.</b> Aniline polymerization mechanism using an N-phenylphenazine type structural unit as cationic initiator.....	<b>20</b>
<b>Figure 1.10.</b> Different types of enzymes used as biofuel cell catalysts. (a) Weakly bound active sites, (b) active site located near surface, and (c) active site buried inside enzyme.....	<b>27</b>
<b>Figure 1.11.</b> Electron transfer mechanism in biofuel cells. (a) Mediated electron transfer using redox mediators (b) Direct electron transfer from active site of enzyme to electrode surface.....	<b>29</b>
<b>Figure 2.1.</b> Typical UV-Visible spectrum of (a) DNA dispersed single-walled carbon nanotube (b) DNA dispersed multi-walled carbon nanotube.....	<b>54</b>
<b>Figure 2.2.</b> UV-Vis-NIR spectrum showing interaction between 70mg/L ssDNA(30T)-SWNT solution with different concentrations of ABA monomers. 0mM (black), 2mM (red), 4mM (magenta), 5mM (blue).....	<b>56</b>
<b>Figure 2.3.</b> Typical UV-Visible spectra of ABA polymerization in the presence of DNA– CNT. The arrows indicate the increase and red shift of the emeraldine absorption peak.....	<b>57</b>

**Figure 2.4.** Kinetic profile of ABA polymerization in the presence of ssDNA–MWNT (red), ssDNA(30T) –SWNT (cyan), ssDNA(15GT) –SWNT (blue), ssDNA(30T) (green), and no CNTs (pristine PABA, black) in acidic medium.....59

**Figure 2.5.** UV-Visible spectrum showing pure PABA polymerized with an APS to ABA molar ratio of 0.25 (blue), 0.16 (black), and 0.11 (red).....63

**Figure 2.6.** Kinetic profile of ABA polymerization in the presence of ssDNA–MWNT (red), dsDNA–SWNT (magenta), ssDNA(15GT)–SWNT (blue), ssDNA(30T)–SWNT (cyan), ssDNA(30T) (green), and no CNTs (pristine PABA, black) in neutral medium.....66

**Figure 2.7.** (left) UV-Visible spectrum of ssDNA(15GT)-SWNT at different microwave irradiation times. 0 min (black), 1 min (red), 3 min (blue). (right) Zoomed in image of shaded area.....70

**Figure 2.8.** Raman spectrum showing (a) the D-band and G band of ssDNA(15GT)-SWNT (b) the radial breathing mode for ssDNA(30T)-SWNT at different microwave irradiation times. 0 min (black), 1 min (red), 3 mins (blue).....73

**Figure 2.9.** Kinetic profile of ABA polymerization in the presence of ssDNA(30T)-SWNT (cyan), ssDNA(15GT)-SWNT (blue), ssDNA(30T)-SWNT after microwave treatment (violet), and ssDNA(15GT)-SWNT after microwave treatment (green) in (a) acidic medium and (b) neutral medium.....74

**Figure 2.10.** Raman spectrum of (a) ssDNA(30T)-SWNT and (b) ssDNA(15GT)-SWNT with different concentrations of ABA monomers. 0mM ABA (black), 3mM ABA (red), 5mM ABA (blue).....77

**Figure 2.11.** (a) FTIR spectrum showing the “electronic-like” band (shaded area) of various DNA-CNT/PABA in acidic medium. UV-Visible-NIR spectra of various in-situ polymerized DNA-CNT/PABA in (b) acidic medium and (c) neutral medium. The curves corresponds to. ssDNA-MWNT/PABA (red), ssDNA(30T)-SWNT/PABA (black), ssDNA-SWNT(15GT)/PABA (blue), and pure PABA (cyan).....79

**Figure 3.1.** UV-Vis spectra of ssDNA/SWNT/PABA irradiated using (a) 254nm light, (b) 365nm light, and (c) 800nm light at different irradiation times. (black curve) 0hr and (red) 5hrs.....94

**Figure 3.2.** UV spectra of (a) pure PABA, (b) 0.2% ssDNA/SWNT/PABA, (c) 1% ssDNA/SWNT/PABA after irradiation for (black) 0hrs, (red) 5hrs, (blue) 20hrs, (green) 35hrs, (magenta) 50hrs, (olive) 65hrs. For all three spectra, UV irradiation causes the intensity of the emeraldine peak at ~800nm to decrease and to blue shift.....96

**Figure 3.3.** (a) Normalized wavelength changes and (b) normalized intensity changes for (black) pure PABA, (red) 0.2% ssDNA/SWNT/PABA, and (blue) 1% ssDNA/SWNT/PABA.....**97**

**Figure 3.4.** Fluorescence spectrum of pure PABA at different irradiation times (black) 0hrs, (red) 5hrs, (blue) 35hrs, (olive) 50hrs, and (magenta) 65hrs.....**98**

**Figure 3.5.** (a) I-V curve of pure PABA irradiated for 0 (black), 60 (red), and 150 mins (green). (b) Normalized relative conductance decrease for pure PABA (black), 0.2% ssDNA/SWNT/PABA (red), 1% ssDNA/SWNT/PABA (blue).....**99**

**Figure 3.6.** (a) FTIR spectra of pure PABA after exposure to UV light irradiation for 0 (black), 5 (red), 20 (blue), 35 (green), 50 (magenta), and 65 hours (olive). (b) Quinoid to benzenoid ratio ( $I_{1596}/I_{1440}$ ) at different irradiation times for pure PABA (black), 0.2% ssDNA/SWNT/PABA (red), 1% ssDNA/SWNT/PABA (blue).....**101**

**Figure 3.7.** (a) Wavelength decrease and (b) absorption decrease of 1% ssDNA-SWNT/PABA (black), postmixture composite (red), and pure PABA (green) after different irradiation times.....**104**

**Scheme 3.1.** Proposed stabilization mechanism of ssDNA/SWNT during the in-situ polymerization process.....**105**

**Figure 3.8.** (a) Normalized intensity changes and (b) normalized wavelength changes for (magenta) MD-SWNT/PABA, (black) pure PABA, (red) 0.2% ssDNA/SWNT/PABA, (blue) 1% ssDNA/SWNT/PABA, and (green) “thin skin” ssDNA/SWNT/PABA.....**107**

**Scheme 4.1.** Illustration showing the assembly of the anode. The gold substrate was first modified with a ligand which allows electrostatic binding to negatively charged ssDNA/MWNT. After immobilization of ssDNA/MWNT, a thin layer of PABA was formed on its surface. A reconstitution approach was used to immobilize glucose oxidase to the gold surface. The FAD cofactor was immobilized via the boronic acid moiety of PABA. Apo-glucose oxidase was finally used to reactivate the enzyme for bioelectrocatalysis.....**120**

**Figure 4.1.** Conductance profile for in-situ polymerized ssDNA/MWNT/PABA composite with ABA concentrations of (blue) 0.75mM, (red) 1.5mM, (green) 2.25mM, and (black) 4.5mM .....**122**

**Figure 4.2.** AFM images of ssDNA/MWNT/PABA with ABA concentrations of (a) 1.5mM, (b) 2.25mM, and (c) 4.5mM.....**123**

<b>Figure 4.3.</b> (a) Cyclic voltammogram of FAD modified electrode at different scan rates. Scan rates range from 9-20V/s. The direction of the arrow in the figure indicates increasing scan rate. (b) Differential pulse voltammogram of the FAD modified electrode.....	<b>124</b>
<b>Figure 4.4.</b> (a) Typical Laviron analysis plot of FAD oxidation peak (b) peak current as a function of scan rate.....	<b>126</b>
<b>Figure 4.5.</b> Nyquist plot of FAD immobilization on polymer composite modified gold electrode at different time intervals. (red) 0 mins, (blue) 30 mins, (brown) 60 mins.....	<b>130</b>
<b>Figure 4.6.</b> Nyquist plot of apo-glucose reconstitution on FAD modified gold electrode at different time intervals. (black) 1hr, (magenta) 2 hrs, (green) 4 hrs, (blue) 5hrs, and (red) 17hrs.....	<b>131</b>
<b>Scheme 4.2.</b> Scheme showing the glucose oxidation of the assembled anode.....	<b>132</b>
<b>Figure 4.7.</b> CV showing glucose oxidation of the assembled anode at different glucose concentrations. (black) 0mM, (red) 1mM, (blue) 5mM, (green) 10mM, (pink) 20mM, (brown) 50mM.....	<b>133</b>
<b>Figure 4.8.</b> Biocatalytic oxidation of glucose with different densities of boronic acid groups. (magenta) ABA/ANI = 1, (green) ABA/ANI = 0.75, (blue) ABA/ANI = 0.5, (red) ABA/ANI = 0.25 and (black) 0% ABA/ANI = 0.....	<b>135</b>
<b>Figure 4.9.</b> SEM image of MWNT array.....	<b>136</b>
<b>Figure 4.10.</b> CV of FAD modified MWNT array at different scan rates. Scan rates are from 9-20V/s. The direction of the arrow in the figure indicates increasing scan rate.....	<b>137</b>
<b>Figure 4.11.</b> (a) Biocatalytic oxidation of glucose using the MWNT array at different glucose concentrations. (black) 0mM, (red) 1mM, (blue) 5mM, (green) 10mM, (magenta) 20mM, (olive) 50mM, (blue) 200mM, (brown) 400mM, and (pink) 800mM. The inset shows a zoom in image of the biocatalytic oxidation at lower glucose concentrations. (b) Michaelis-Menten graph of biocatalytic oxidation of glucose using the MWNT array.....	<b>138</b>
<b>Figure 4.12.</b> Chemical structure of (a) FAD and (b) FAD-NH <sub>2</sub> .....	<b>140</b>
<b>Figure 4.13.</b> Michaelis-Menten graphs of enzyme modified gold electrodes using (a) ABA monomers and (b) ANI-COOH monomers.....	<b>141</b>

**Figure 5.1.** Structures of DFO, PL-PEG-COOH, and DFO-Fe (III) chelate complex.....**159**

**Figure 5.2.** UV-Visible spectrum showing (black) DFO dissolved in nitric acid, (blue) DFO with 10nM Fe (III) in nitric acid and (red) DFO with 300μM Fe (III) in nitric acid.....**160**

**Scheme 5.1.** Scheme showing the surface modification of carbon nanotubes for sensitive and selective detection of Fe(III). Pristine SWNTs are first dispersed with PL-PEG-COOH by probe sonication method followed by EDC/NHS coupling with DFO. This method ensures that the electronic properties of the SWNTs are intact and high concentrations of DFO are on the SWNT surface.....**161**

**Figure 5.3.** (a) AFM image of PL-PEG-COOH dispersed SWNT. (b) UV-Vis spectrum of PL-PEG-COOH dispersed SWNT .....**163**

**Figure 5.4.** UV spectrum of PL-PEG-COOH/SWNT/DFO in the presence of (black) 0pM, (red) 10pM, (green) 30pM, (blue) 50pM, (cyan) 70pM, and (magenta) 90pM of Fe (III) standard solution.....**165**

**Scheme 5.2.** Scheme showing the surface modification of carbon nanotubes for the detection of Fe(III) using microwave radiation approach. Pristine SWNTs are first treated with microwave radiation in concentrated acid. This allows the formation of –COOH groups on the surface of the SWNT. Unlike the approach in scheme 1, the surface of the SWNTs is destroyed using microwave radiation. Carboxylation of SWNT was followed by EDC/NHS coupling with DFO. ....**168**

**Figure 5.5.** UV spectrum showing MF-SWNT/DFO in the presence of (black) 0pM  $\text{Fe}^{3+}$ , (red) 120pM  $\text{Fe}^{3+}$ , (blue) 240pM  $\text{Fe}^{3+}$ , (pink) 480pM  $\text{Fe}^{3+}$ , (navy) 720pM  $\text{Fe}^{3+}$ , (magenta) 960pM  $\text{Fe}^{3+}$ , (green) 1.08nM  $\text{Fe}^{3+}$ , (violet) 1.08nM  $\text{Fe}^{3+}$  + mixture, and (orange) 1.20nM  $\text{Fe}^{3+}$ . The mixture contains. 3.3nM  $\text{Fe}^{2+}$ , 3.3nM  $\text{Cu}^{2+}$ , 3.3nM  $\text{Mg}^{2+}$ , 3.3nM  $\text{Pb}^{2+}$ , and 3.3nM  $\text{Ni}^{2+}$ . Baseline used is PL-PEG-COOH/DFO, therefore absorptions are negative.....**170**

**Figure 5.6.** (a) UV spectrum of PL-PEG-COOH/SWNT/DFO in the presence of (black) 0pM, (red) 10pM, (green) 30pM, (blue) 50pM, (cyan) 70pM, and (magenta) 90pM of aluminum standard solution. (b) Comparison between the relative intensity decrease of (black) Fe(III)-DFO complex and (blue) Al(III)-DFO complex. The red line represents the best fit curve.....**172**

**Figure 5.7.** UV spectrum of PL-PEG-COOH/SWNT/DFO in the presence of (black) 0pM Fe (III), (red) 10pM Fe(III), (green) 100pM Al(III), (blue) 30pM Fe(III), and (cyan) 300pM Al(III) solution.....**173**

**Figure 5.8.** UV spectrum of PL-PEG-COOH/SWNT/DFO in the presence of (black) 0pM  $\text{Fe}^{3+}$ , (red) 10pM  $\text{Fe}^{3+}$ , (blue) 10uM  $\text{Ca}^{2+}$ , (dark blue) 10uM  $\text{Mg}^{2+}$ ,

(pink) 30pM  $\text{Fe}^{3+}$ , (olive) 10nM  $\text{Cu}^{2+}$ , (violet) 10nM  $\text{Zn}^{2+}$ , (brown) 50pM  $\text{Fe}^{3+}$ , (magenta) 10nM  $\text{Cd}^{2+}$ , (green) 10nM  $\text{Pb}^{2+}$  .....174

**Figure 5.9.** UV spectrum of PL-PEG-COOH/SWNT/DFO in the presence of (black) 0pM, (red) 10pM, (green) 30pM, (blue) 50pM, (cyan) 70pM, and (magenta) 90pM of Fe (III) rain water.....175

**Figure 6.1.** UV-Vis-NIR spectrum of (a) PL-PEG-COOH/SWNT and (b) MF-SWNT.....188

**Figure 6.2.** Raman spectrum of (red) PL-PEG-COOH/SWNT and (black) MF-SWNT.....190

**Figure 6.3.** Raman spectra of (blue) SKBR3 cell line treated with antibody/SWNT complex, (brown) SKBR3 cell line treated with PL-PEG-COOH/SWNT, (magenta) untreated SKBR3 cell line, and (brown) MCF7 cell line treated with antibody/SWNT complex.....191

**Scheme 6.1.** schematic approach for the noncovalent functionalization of SWNT and anti-HER2 IgY antibody.....192

**Figure 6.4.** Raman spectra of (blue) SKBR3 cells treated with anti-HER2/PEG-SWNT, (red) MCF7 cells treated with anti-HER2/MF-SWNT, (green) SKBR3 cells treated with PL-PEG-COOH/SWNTs only without conjugation of the anti-HER2, and (cyan) untreated SKBR3 cells.....193

**Figure 6.5:** Fluorescence images of (a) SKBR3 cells treated with anti-HER2/SWNT complex (b) SKBR3 cells treated with PL-PEG-COOH/SWNT (no antibody), (c) untreated SKBR3 cells (d) Receptor negative MCF7 cells treated with anti-HER2/SWNT complex. Cells with green fluorescence are alive and cells with red fluorescence are dead.....195

## List of Tables

<b>Table 2.1.</b> Comparison of polymerization rate constants for the acidic polymerization of ABA in the presence of different CNTs and different sequences of DNA.....	<b>64</b>
<b>Table 2.2.</b> Comparison of polymerization rate constants for the neutral polymerization of ABA in the presence of different CNTs and different sequences of DNA.....	<b>67</b>
<b>Table 4.1.</b> Table of different parameters and their calculated FAD electron transfer rate constant.....	<b>127</b>
<b>Table 5.1.</b> Stability constants for different DFO-metal ion complex.....	<b>170</b>



# **Chapter 1**

## **Introduction**

### **1.1 Carbon Nanomaterials**

Carbon is one of the most abundant elements found on Earth and has been known for hundreds of years. Up until about 30 years ago, there were only three forms of carbon that existed in nature: diamond, graphite, and amorphous carbon [1-2]. Due to their unique atomic orbital hybridization, carbon can form different types of bonds leading to these various structural forms. Although they are all allotropes of carbon and they differ only in the arrangement of atoms in its crystal lattice, their properties are very different. Diamond is known to be transparent, one of the hardest substance in the world, and an excellent insulator whereas graphite is opaque, used as pencil lead for its softness, and used in electrical cells for their high conductivity [3].

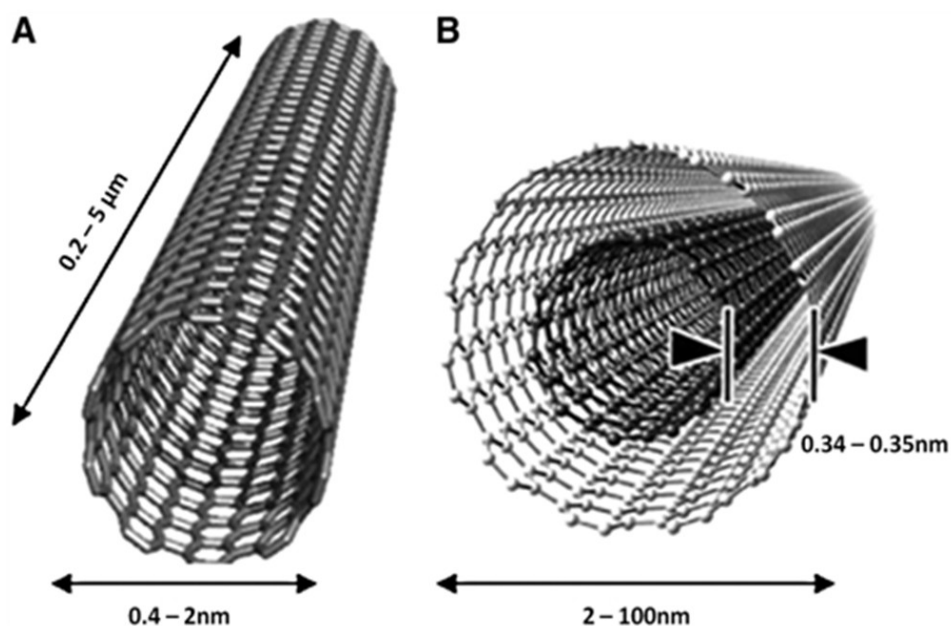
Research in the field of carbon nanostructure materials have been of great interest since the discovery of fullerenes in 1985 [4], carbon nanotubes in 1991[5], and graphene in 2004 [6], and is still one of the most highly researched fields today. The interest is mainly due to their nanoscale properties which are size dependent and are very different from that of their macroscale counterpart [7]. As materials decrease to the nanoscale, properties such as melting point, color, electrical conductivity, and chemical reactivity changes as a function of

particle size. As a classic example, bulk gold is known to have a yellowish color and is stable in air. However, as we approach the nanoscale, gold nanoparticles are red in color and are highly reactive unless stabilized with surfactants. It is these unique and remarkable nanoscale properties that have made carbon nanomaterials attractive for many applications in different fields of science.

Another property of interest is the change in electronic properties as materials are reduced down to the nanoscale. For example, bulk diamond and graphite have different dimensions compared with the fullerenes, carbon nanotubes, and graphene. Fullerenes are considered 0-dimensional, carbon nanotubes are 1-dimensional, and graphene are 2-dimensional. The dimensions of a solid state material are extremely important because it affects its density of states, which in turn affects its band structure and its electronic properties [8]. Therefore, by changing the dimensions it can give rise to materials with different electronic properties which can be used in various applications.

## **1.2 Carbon Nanotubes**

One of the most studied carbon nanomaterials today are carbon nanotubes. Their superior optical, thermal, mechanical, and electronic properties have been exploited for various applications. These applications include, but are not limited to, structural reinforcements for composite material, chemical sensing, and biological sensing.



**Scheme 1.1:** Schematic representation of (a) SWNT and (b) MWNT (specific case shown is double walled carbon nanotube). Image reproduced from ref. [10]

Carbon nanotubes are well-ordered, all carbon hollow graphitic nanomaterials with very high aspect ratios. There are two different types of carbon nanotubes: single-walled carbon nanotubes (SWNT) and multi-walled carbon nanotubes (MWNT). SWNTs are usually several hundred nm to several μm in length and 0.4 – 2 nm in diameter [9] (Scheme 1.1). Similarly, MWNT lengths can also be several μm long but their diameters typically range from 2 to 100nm. Conceptually, the structure of SWNTs can be viewed as “wrapping” a graphene sheet into a seamless hollow cylinder (graphene is a one-atom-thick planar sheet of  $sp^2$ -bonded carbon atoms that are densely packed in a honeycomb crystal lattice). The structure of MWNTs can be pictured as several

co-axially arranged SWNTs of different radii with an inter-tube separation of 3.4 – 3.5Å [9].

There are a number of ways of rolling a graphene sheet to form a single-walled carbon nanotube. The large number of ways to roll the graphene sheet provides a family of nanotubes with different diameters and chirality, which are significant in determining the physical properties of SWNTs [11]. The direction in which the tubes are rolled up is usually labeled in terms of the lattice vectors by a pair of indices  $(n, m)$  (Figure 1.1), where  $(n, m) = \mathbf{L} = x\mathbf{a} + y\mathbf{b}$ . In this equation  $x$  and  $y$  denote the number of unit vectors ( $\mathbf{a}$  and  $\mathbf{b}$ ) along two directions in the honeycomb crystal lattice of graphene and  $\mathbf{L}$  is the chiral vector [12]. The diameter of the nanotube is related to the chiral vector by

$$d = \frac{L}{\pi} = \frac{Ac\sqrt{x^2 + xy + y^2}}{\pi}$$

where  $d$  is the diameter of the nanotube and  $Ac$  is the carbon-carbon distance between two neighboring atoms. The chiral angle ( $\eta$ ) which determines the hexagonal network arrangement of the nanotube, and thus the chirality, is given by

$$\eta = \tan^{-1}\left(\frac{x\sqrt{3}}{x + 2y}\right)$$

Depending on how the SWNTs are rolled up along the chiral vector they can be classified into three distinct classes. For a given  $(n, m)$ , if  $m = 0$  then the

SWNTs are known as zigzag nanotubes. If  $m = n$  then the SWNTs are armchair nanotubes, otherwise they are chiral nanotubes. The chiral vector can also be used to determine the electronic behaviors of the SWNTs. SWNTs are known to be either semiconducting or metallic. It has been shown that for a given  $(n, m)$ , the nanotube is metallic if  $n = m$  or if  $n - m$  is a multiple of 3, otherwise the nanotube is semiconducting [11-18]. By varying the nanotube diameter and/or chiral angle, different types of nanotubes with various properties can be obtained. Since MWNTs are made up of concentric SWNTs, they are essentially metallic in nature due to inter-tube interactions [19].

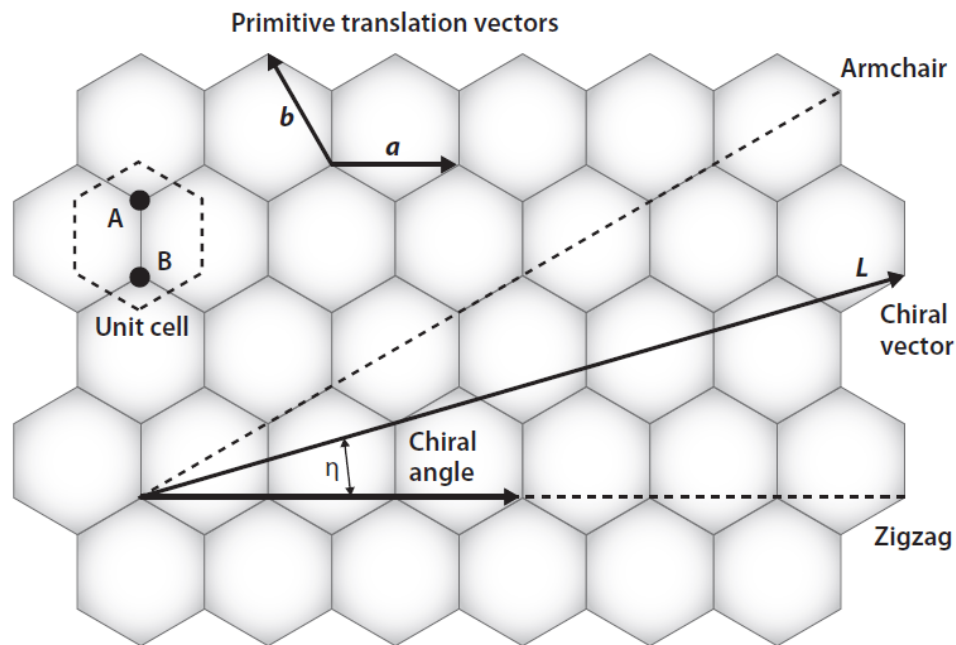


**Figure 1.1:** The unrolled honeycomb lattice of a carbon nanotube.  $\eta$  is the chiral angle and  $L$  is the chiral vector. Image reproduced from ref. [20]

Carbon nanotubes display exceptional and unusual electrical, mechanical and optical properties because of their one dimensional structure. They have excellent electronic properties: metallic nanotubes can carry an electrical current density of  $4 \times 10^9 \text{ A/cm}^2$ , which is three orders of magnitude higher than a typical metal, such as copper or aluminum [21]. Individual semiconducting SWNTs are known to possess an extremely high carrier mobility of  $10,000 \text{ cm}^2/\text{Vs}$  at room temperature, and can be operated at high frequencies (2.6 GHz). These values exceed those for all known semiconductors, such as silicon [22], which bodes well for application of nanotubes in high-speed transistors, single- and few-electron memories, and chemical/ biochemical sensors [23-24]. Moreover, they are flexible owing to their small diameter. SWNTs are therefore also an ideal candidate material for high-performance, high-power, and flexible electronics [25-26]. They are also the strongest and stiffest materials discovered in terms of tensile strength and elastic modulus, respectively. The Young's modulus is over 1 Tera Pascal; it is stiff as diamond and the estimated tensile strength is 200 Giga Pascal [27]. The strength results from the covalent  $\text{sp}^2$  bonds formed between the individual carbon atoms and these properties are ideal for reinforced composites [28-31] and nanoelectromechanical systems (NEMS) [32]. Furthermore, the heat transmission capacity of individual CNTs at room temperature has been shown to exceed  $3000 \text{ Wm}^{-1}\text{K}^{-1}$ , which is greater than that of natural diamond, and are excellent for thermal management [33]. Equally important, both SWNTs and MWNTs are now produced in substantial quantities making them highly attractive for these commercial applications.

## 1.3 Surface Engineering of Carbon Nanotubes

Like diamond and graphite, carbon nanotubes are hydrophobic in nature and in order to exploit their unique properties, it is necessary to modify them. A unique feature of carbon nanotubes is that every atom is at its surface and therefore surface chemistry or modification is expected to be critical and can affect their properties [34-36]. Surface modification of carbon nanotubes have been used to solubilize them in different media [34, 36], self assembled them on different types of surfaces for certain applications [35], and for sensing applications [35, 37].

There are two approaches to functionalize the surface of carbon nanotubes. Based on the mechanism of attachment to the surface, they can be covalently or noncovalently functionalized. In covalent surface functionalization, functional groups are attached to either the sidewalls, nanotube ends, or at defect sites [38-39]. This can be accomplished by a variety of ways. Ros *et al.* [40] have shown that effective modification can be achieved by surface oxidation of carbon nanotubes by a mixture of concentrated nitric and sulfuric acid. This method creates oxygen containing groups such as aldehydes, ketones, carboxylic acids, epoxides, and alcohols on the defect sites [40] which can be used for further modification for different applications. Surface modification of carbon nanotubes can also be accomplished by fluorination and subsequent derivatization [41]. Figure 1.2 shows the many pathways carbon nanotubes can be covalently functionalized.

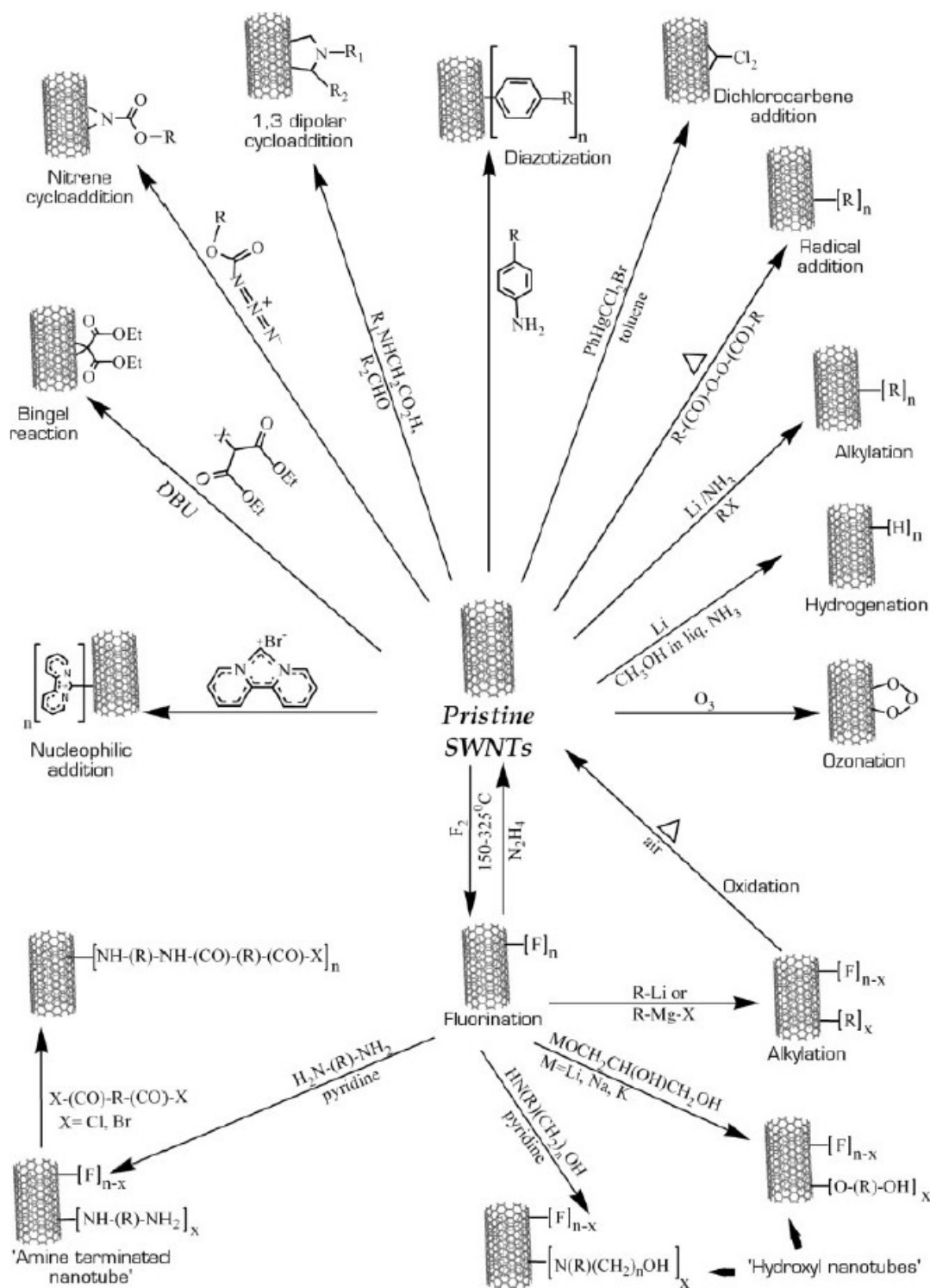


**Figure 1.2:** Scheme showing different ways of covalently functionalizing carbon nanotubes. Image reproduced from ref. [39]



Noncovalent functionalization of the carbon nanotube surface is also possible. Examples of noncovalent functionalization of carbon nanotubes include “wrapping” of linear water soluble polymers around its surface [39]. In this method, the polymer helps solubilize the carbon nanotubes in aqueous solution and also prevents the carbon nanotube from aggregation. In a similar manner, single stranded DNA have also been used to modify the carbon nanotube surface [42]. The nucleobases form  $\pi$ -stacking interactions with the carbon nanotube surface while the hydrophilic phosphates groups on the DNA are exposed to the aqueous solution [42]. One of the main advantages of noncovalent functionalization compared with covalent functionalization is the preservation of the carbon nanotube electronic structure by avoiding the disruption of the  $sp^2$  hybridized structure and its conjugation.

## 1.4 Conjugated Conducting Polymers

Up until 40 years ago, all polymers that were developed had high electrical resistance and were mainly used as insulating material. It was not until the 1970s that polyacetylene was shown to exhibit a dramatic increase in electrical conductivity upon a process called doping. Normally polyacetylene is resistive but when doped with iodine vapor, the conductivity was shown to increase by 12 orders of magnitude [43]. This increase in conductivity was attributed to charge carriers formed by charge transfer from the acetylene chain (donor) to iodine (acceptor). The charge carriers were allowed to freely move along the polymer

chain, leading to its metallic-like behavior. This discovery launched a new field of research and a new class of material which are highly attractive due to their processability, high conductivity, low cost, flexibility, and nontoxicity [44]. Figure 1.3 shows the structures of some of these types of polymers.

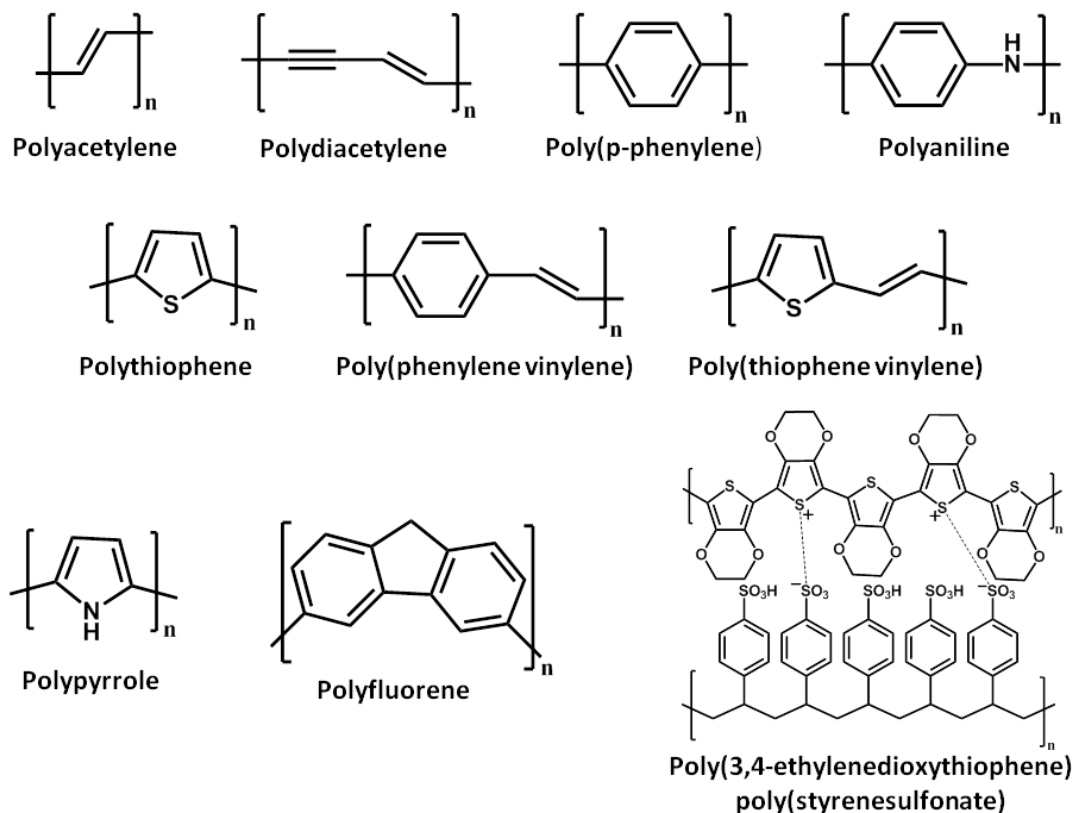


**Figure 1.3:** Structures of various conjugated polymers.

The intrinsic conductive nature of polymers like polyacetylene originates from the overlapping p orbitals of the conjugated system. This causes electrons to delocalize along the conjugated chain of the polymer. However, the conjugated polymer itself is normally not conductive. In order for it to be

conductive, electrons must be either added (reduction, n-type doping) or removed (oxidation, p-type doping) from the polymer chain. This process is called doping. Depending on the doping degree and the dopant, dramatic changes to the conducting polymer's properties can be induced. The conductivity of conjugated polymers can be controlled from the undoped insulating form to a fully doped highly conducting form. Conducting polymers have been shown to have conductivities ranging from  $<10^{-7}$  S/cm to as high as  $10^5$  S/cm [45].



**Figure 1.4:** Various applications of conducting polymers

Due to their interesting properties conducting polymers have potential applications in electronic devices, sensors, and biosensors [45]. Some of these applications can be seen in Figure 1.4. Some of the most studied conducting polymers include polypyrrole, polythiophene, poly (3,4 ethylenedioxythiophene), and polyaniline due to their high conductivities and relatively good stability.

## 1.5 Polyaniline

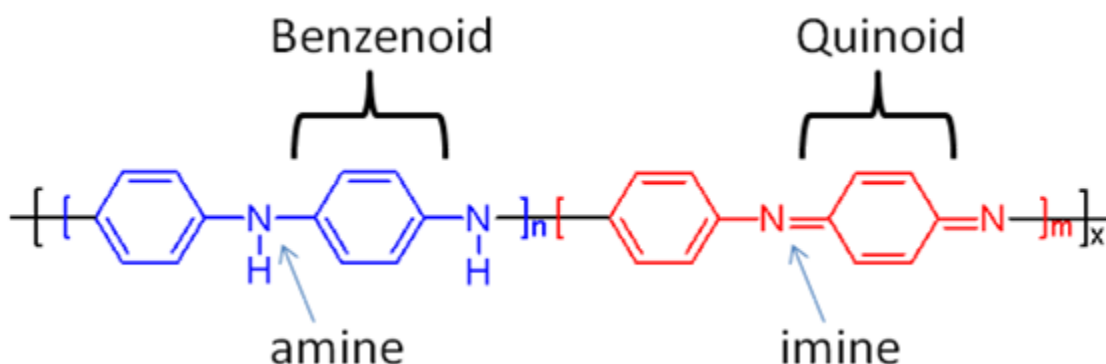


**Figure 1.5:** General structure of polyaniline

Since its discovery as a conducting polymer, polyaniline has been intensely researched due to its ease of synthesis, its relatively high conductivity ( $10^2$  S/cm) [46], and interesting properties. The structure of polyaniline is made up of a combination of benzenoid, quinoid, imine, and amine units (Figure 1.5). The benzenoid units are normally connected to amine units (which shall now be referred to as reduced unit) and the quinoid units to imine units (oxidized unit).

When oxidized, the “reduced units” are converted to the “oxidized units”. Therefore, by changing the ratio of “reduced units” to “oxidized units”, various oxidation states of polyaniline can be formed. From Figure 1.5,  $n$  and  $m$  represents the number of “reduced units” and “oxidized units” in the polymer chain, respectively. In addition  $n$  and  $m$  can only have values ranging from 0 to 1 and must satisfy the equation  $n + m = 1$ . If  $m=0$  and  $n=1$ , then no quinoid units are present in the polyaniline chain. Therefore the polymer is considered to be in the 100% reduced form and is called the leucoemeraldine base oxidation state. If  $m = 0.5$  and  $n= 0.5$ , then the polymer is in the half oxidized and half reduced and is known as the emeraldine base oxidation state. If  $m = 1$  and  $n = 0$ , the polymer is in the fully oxidized form and is known as the pernigraniline base oxidation state. It is possible that  $m$  and  $n$  have other values besides the ones stated; however, the three oxidation states mentioned are the ones that are most studied. In the base form, all polyaniline oxidation states are nonconductive. The three polyaniline bases can be converted to their salt forms by protonation, however, studies have shown that only the protonation of the emeraldine base form to give the emeraldine salt oxidation state is conductive [47]. The different oxidation states of polyaniline are shown in Figure 1.6.

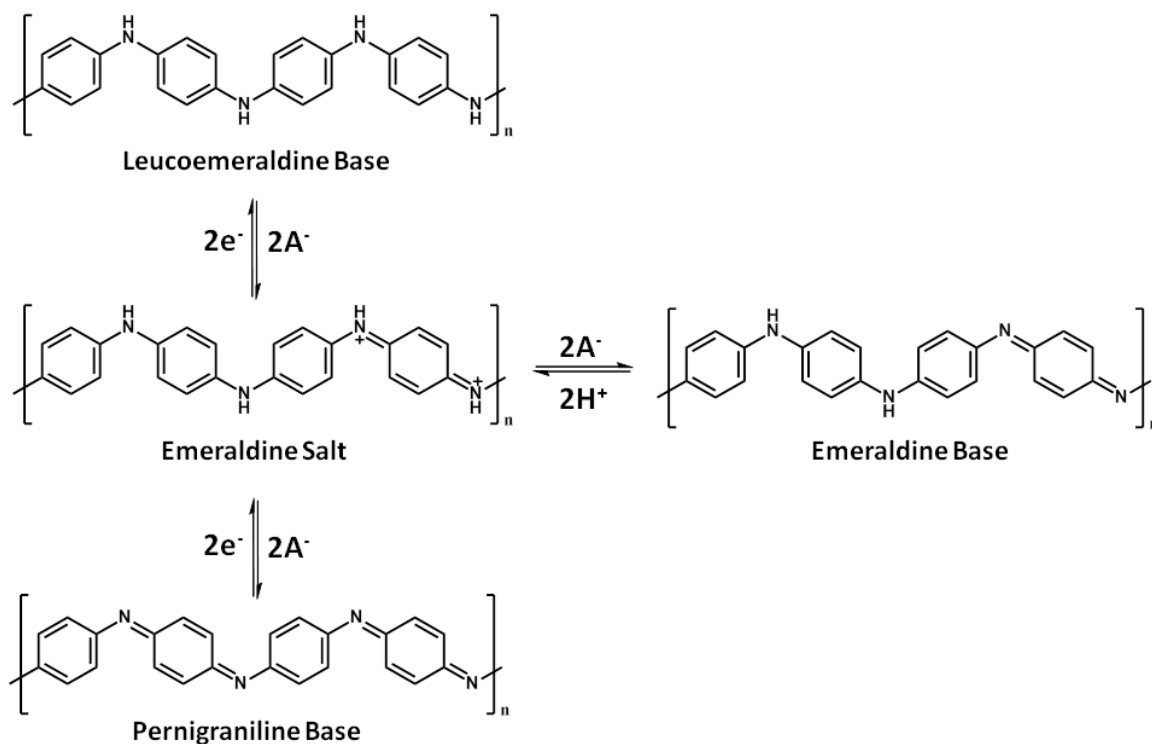


**Figure 1.6:** Different oxidation states of polyaniline

Doping of emeraldine base can be accomplished by an oxidative approach or by proton doping [48]. Upon doping with acid, the imine units ( $pK_a = 5.5$ ) of the emeraldine base are more susceptible to be protonated compared with amine units ( $pK_a = 2.5$ ) due to their basicity [49]. When both imines of the quinoid unit are protonated (Figure 1.7a), it forms a bipolaron charge carrier which is represented as two positive charges (Figure 1.7b). To stabilize the positive charges, polyaniline undergoes an internal redox reaction to form two separate polaron charge carriers (Figure 1.7c). Finally the two polaron charge

carriers travel along the conjugated polymer chain to further stabilize itself (Figure 1.7d).

Oxidative doping of polyaniline can be explained in a similar context. Partial oxidation of the polymer chain causes the removal of an electron. This causes a polaron charge carrier to be formed on the polymer chain. When the polymer is oxidized again, another polaron charge carrier is formed. At this stage, the two polaron charges can either form a bipolaron or migrate along the polymer chain to stabilize itself.

The unique properties of polyaniline have made it attractive for potential applications in various fields. The ability of polyaniline to exist in different oxidation states, which are all different in color, allows it to be used in electrochromic devices, toxic gas sensors, and for bacteria detection [50-52]. Their oxidation / reduction ability have been exploited in rechargeable batteries [53] and their doping/dedoping process have been used for gas, chemical, and pH sensors [54-56].

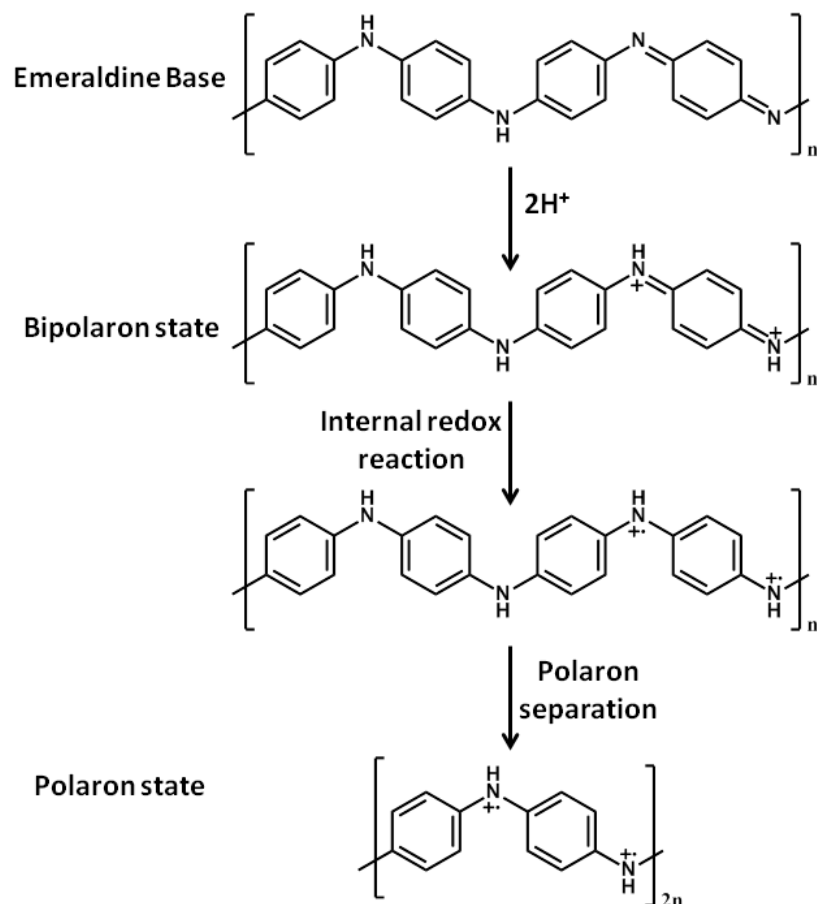


**Figure 1.7:** Polaron charge carrier formation by acid doping

## 1.6 Polyaniline Polymerization Mechanisms

The polymerization of aniline to form polyaniline can be carried out chemically or electrochemically. In the chemical oxidative approach, aniline (ANI) is usually oxidized by an oxidizing agent such as ammonium persulfate in acidic conditions to form polyaniline (PANI). In the electrochemical approach, aniline is also oxidized in acidic conditions to form polyaniline. However, the difference is



that the oxidizing agent is either an applied constant current, constant potential, or a repetitive cycling between a certain potential range.

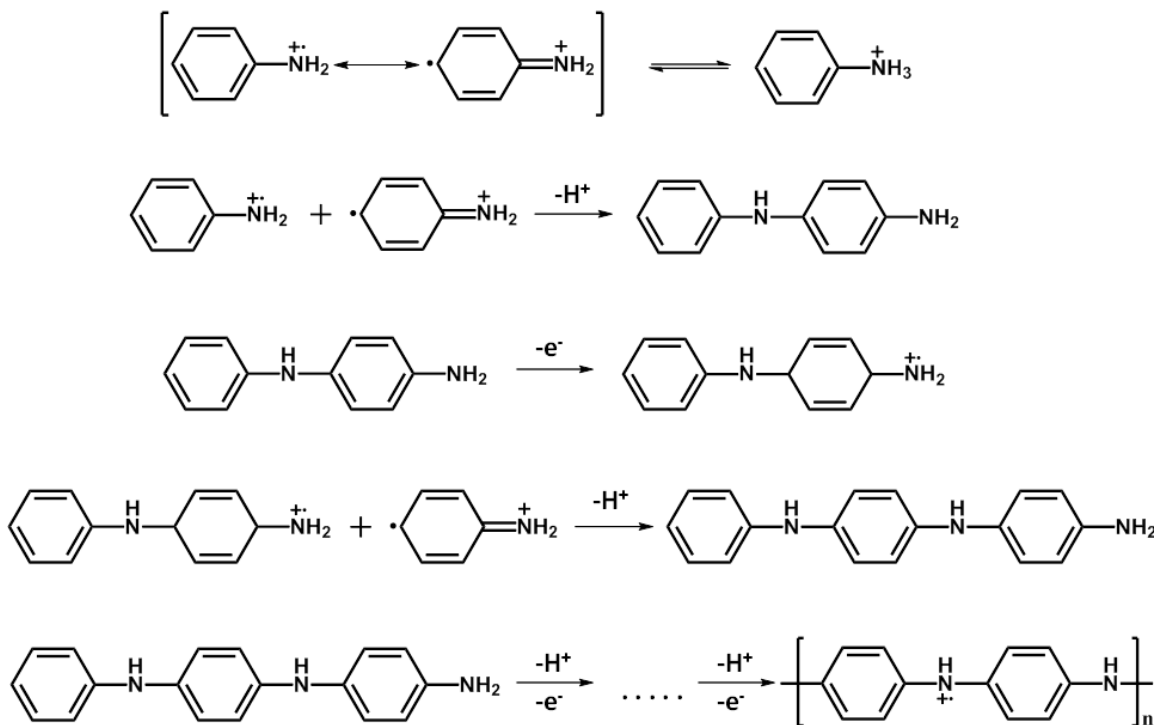


**Figure 1.8:** Aniline polymerization mechanism using anilinium cation-radical as cationic initiator.

Although it is generally accepted that ANI polymerization follows a cationic polymerization approach, the actual mechanism of forming the cationic initiator itself has been widely debated. One of the mechanisms that is accepted in literature for ANI polymerization in acidic medium is shown in Figure 1.8. As shown, the ANI monomer is first partially oxidized by a strong oxidant to form an

anilinium cation-radical initiator. This initiator further reacts with ANI monomers at the para position while transferring its charge until the polymer is produced. From basic organic chemistry, it is known that aniline is an ortho, para director. However, in order for the polymer to be highly conductive, the PANI chain must be linear, long, and highly conjugated. Thus in order for a highly conductive PANI to form, the ANI monomers must undergo continuous para coupling.

As opposed to the mechanism shown previously where the cationic initiator is an anilinium cation-radical, there have been other accounts where the cationic initiator is a phenazine-like structure formed from “mixed” oxidative coupling of ANI monomers [57-59]. Similar to the previous mechanism, the ANI monomer is also partially oxidized to form an anilinium molecule (Figure 1.9). However, the anilinium molecule formed undergoes ortho coupling rather than para coupling as shown in the previous case (Figure 1.8). After the dimer (A) is formed, the third monomer undergoes para coupling to form a trimeric structure (B). Upon further oxidative coupling, a N-phenylphenazine (C) structural unit is formed. This phenazine-like molecule has been detected during the polymerization of ANI by various groups using electrochemistry [60], Raman spectroscopy [61], mass spectrometry [62], FTIR spectroscopy [62], and NMR studies [63]. However, its role during polymerization has been a subject of debate. Some attribute the N-phenylphenazine molecule as an initiation point for polymerization [58-59] while others attributed it as a degradation product from overoxidation [60].

Notice at this point, the phenazine-like molecule (C) is uncharged and thus cannot undergo cationic polymerization. The introduction of an additional ANI monomer, however, causes the whole structure to adopt a positive charge and thus creates the cationic initiator that is necessary for cationic polymerization. The positive charge is formed by protonation of the primary amine unit after reaction of N-phenylphenazine unit with an ANI monomer. The formation of this cationic initiator (D) is an extremely slow process and is the rate limiting step due to the fact that the N-phenylphenazine molecule (C) is fairly stable by itself. Once the cationic initiator is formed, every subsequent ANI monomer will undergo para coupling to maximize electron delocalization of the positive charge in the polymer chain structure. Therefore, after the cationic initiator is formed, the polymer chain starts to grow at a dramatic rate since the monomers will only add to the para position to form the most stable structure possible. As shown in the figure, highly conductive polyaniline (E) is produced once the N-phenylphenazine type cationic initiator is formed.

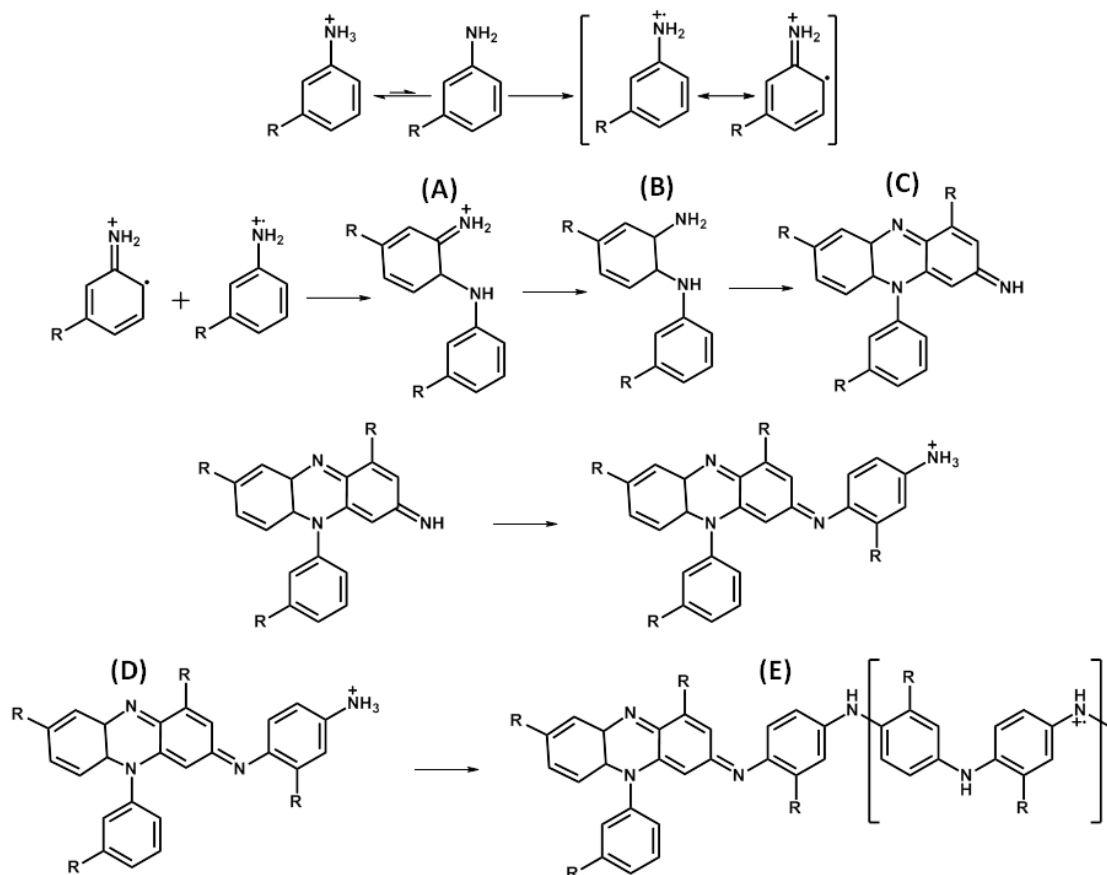


**Figure 1.9:** Aniline polymerization mechanism using an N-phenylphenazine type structural unit as cationic initiator. Ani in the figure represents an aniline monomer and R represents B(OH)<sub>2</sub> (a boronic acid group)

Although both mechanisms are used in literature, the second mechanism that uses the N-phenylphenazine type cationic initiator will be used as the general polymerization mechanism in this thesis. Based on various reports on ANI polymerization, the process normally begins slowly, followed by a dramatic rate increase [58, 64-67]. In the first mechanism, the monomers are added consecutively in a para linked fashion and kinetically it is difficult to explain why the rate of adding the first monomer to form the dimer is different from adding the

other monomers to form the polymer. In the second mechanism, however, a trimeric fragment is first formed followed by a long linear PANI chain. The formation of the N-phenylphenazine fragment can be associated with the slow process and the formation of the long linear PANI chain by cationic polymerization can be associated with the dramatic rate increase.

## 1.7 Self-Doped Polyaniline

Although polyaniline shows numerous advantages, its poor solubility in various solvents and its limited pH range (acidic media) prevents it from use in many biological applications. This problem was solved by the discovery of self-doped polyaniline in 1990 [68]. The self-doping nature is due to the negatively charged ionizable functional groups attached along the polyaniline backbone. The negatively charged functional groups (i.e. boronic acid, sulfonic acid) act as intramolecular dopant anions that help stabilize the positive charge induced by protonation of the imines. In the acid doped polyaniline case, anions in solution are usually used to help stabilize the positive charge from the protonation of imines. The self doping nature imparts additional interesting properties to the polyaniline. It has been shown that self-doped polyaniline is electrochemically active in a wide pH range up to very basic conditions (pH 12), whereas native polyaniline is active only at  $\text{pH} < 4$  [69]. In addition, the functional groups increase the solubility of polyaniline making them useable for different applications.

## 1.8 Carbon Nanotube Composites

### 1.8.1. Polymerization Kinetics

Tremendous efforts have been made to prepare conducting carbon nanotube polymer composites (CNT/polymer) with an aim to synergistically combine the merits of each individual component [5, 70-74]. The easiest and most straightforward approach to fabricate a carbon nanotube composite is to mix a preformed polymer with carbon nanotubes. However, our recent works demonstrated that this simple mixing approach might not fully and synergistically combine the merits of the carbon nanotubes and conducting polymers. By following the dispersion recipes developed by Zheng *et al* [42, 75] we dispersed SWNTs into water solutions. As a result, single stranded DNA (ss-DNA) functionalized single walled carbon nanotubes (ss-DNA/SWNTs) were obtained. By in-situ polymerization of 3-aminophenylboronic acid (ABA) monomers in the presence of the ss-DNA/SWNTs, we fabricated a water soluble and highly conductive self-doped polyaniline/SWNT composite [76]. We found that the ss-DNA/SWNTs acted as molecular templates, facilitating head-to-tail coupling during polymer growth [77], which results in PABA with long conjugated length and high conductivity. More interesting, we found the polymerization speed was dramatically increased (up to 4500 times faster) and the polymerization also required less oxidant, indicating that a much faster and “greener” polymerization approach can be developed for the production of conducting polymer

nanocomposites. In addition, we found that these advantages cannot be obtained using *in situ* polymerization with preoxidized ssDNA-SWNTs. These results indicated that *in situ* polymerization of the respective monomers in the presence of carbon nanotubes could form a genuine polymer/CNT composite with much more enhanced features compared to the “post mixing” approaches [71, 73, 78]. However, the enhancement would highly depend on the electronic structures of the carbon nanotubes and the monomer-nanotube interaction during polymerization, which greatly influence the kinetics of nanocomposite fabrication and the electronic performance of the resulting composites.

Furthermore, *in-situ* polymerization requires predispersing the carbon nanotubes into solution. Different dispersion approaches have been reported, such as polymer wrapping, just as single stranded DNA we used [42], or noncovalent adhesion of molecules [79], and acidic oxidation [80]. All these different approaches and even different molecules used in the same approach will impart different surface chemistries and electronic structures to the carbon nanotubes. The impact of different surface chemistry and electronic structure of the carbon nanotubes on the kinetics of the nanocomposite fabrication and the quality of the obtained composite has not been systematically studied. These studies are both fundamentally and practically important, which is one of the study objectives of this thesis. In this thesis, we will exploit the important chemical features of nucleic acid biopolymers to reach this aim. The advances in DNA technology allow the construction of various types of base sequences. Not only has DNA been used to efficiently disperse SWNTs into water solutions [42],

it has also been explored for separation of carbon nanotubes [42, 81]. Recently, Napier *et al.* [82] reported that DNA dispersed carbon nanotubes with different G nucleobase have different electrocatalytic ability in the electrochemistry of  $\text{Ru}(\text{bpy})_3^{2+}$  complex. The authors ascribed this difference to the reductive ability of the G sequence. In this thesis, we will use DNA with different sequences, especially DNA with G nucleobase, to disperse and functionalize SWNTs and MWNTs to systematically study how the electronic structures and surface chemistry of carbon nanotubes impact the in situ polymerization kinetics and the quality of the formed composites.

### **1.8.2. Stabilization of polymers from degradation**

Short lifetime has been a thorny problem for devices consisting of organic polymeric materials. One of the important reasons is the degradation of the polymers exposed to UV light from the sun. Recently, it was found the carbon nanotubes not only enhance the conductivity and mechanical performance of the composites, it also shows great oxygen radical scavenging capabilities [83], therefore they can be used as antioxidants to stabilize polymers [84]. The antioxidant effect was mainly attributed to the strong electron affinity of the carbon nanotubes. As we described earlier, different dispersing approaches results in carbon nanotubes with different electronic properties and surface chemistries. Therefore, their electron affinity would also be different. Because of this, it is of academic interest and practical importance to study how to optimize



the anti-degradation effects of carbon nanotubes. This study would lead to the formation of stable composite materials for developing devices with longer life spans and thus commercial value.

## **1.9 Enzymatic Biofuel Cells**

Biological fuel cells are energy conversion devices that convert chemical energy into electrical energy using biological processes [85]. In biofuel cells, the fuel and the catalyst used are all biological material. The fuel used is normally methanol, glucose, or organic acids, which are all renewable and can be produced by biological processes. Consequently, intense research has been focused on studying biofuel cells for their potential application in energy production.

### **1.9.1. Types of biofuel cells**

There are two different types of biofuel cells: microbial and enzymatic. The difference between microbial and enzymatic biofuel cells is that microbial biofuel cells use whole micro-organisms rather than enzymes as the catalyst [85-87]. Theoretically, microbial biofuel cells should have unlimited lifetime as long as a fuel is supplied since it is based on living micro-organisms. Enzymatic biofuel cells, however, have limited lifetimes due to their instability. In addition, extraction of enzymes is much more expensive than maintaining a culture of bacteria or other micro-organisms. The power density achieved from microbial biofuel cells,

however, is normally lower than that of enzymatic biofuel cells due to their resistance to mass transfer across the cell membranes [87]. Furthermore, microbial biofuel cells are not selective; therefore it can react with any fuel that is introduced. Even though enzymatic biofuel cells have lower stability and are more expensive than microbial biofuel cells, their high specificity and high power density (which can be achieved using electrical wiring and immobilization techniques) makes them highly attractive as biocatalysts in biofuel cells.

### **1.9.2. Types of enzymes used in enzymatic biofuel cells**

The biocatalytic reaction occurs at the active site which is located within the enzymes. Depending on where the active site is located, enzymes can be divided into three categories: 1) active sites with reversibly bound coenzymes, 2) active sites located near the surface of the enzymes, and 3) active sites buried deep within the enzymes. An example of a reversibly bound coenzyme is nicotinamide adenine dinucleotide (NADH/NAD<sup>+</sup>). It can diffuse out and facilitate electron transfer by acting as a mediator [86-87]. Enzymes that have their active site located near the surface include certain peroxidases [88]. Since the active site is located near the surface, orienting the enzyme for immobilization to the electrode is crucial. Enzymes with their active site buried inside the protein shell have very slow electron transfer rates. An example of this is flavin adenine dinucleotide (FAD), which normally would require redox mediators that can

diffuse into the enzyme to facilitate electron transfer. Figure 1.10 shows the different types of enzymes described.

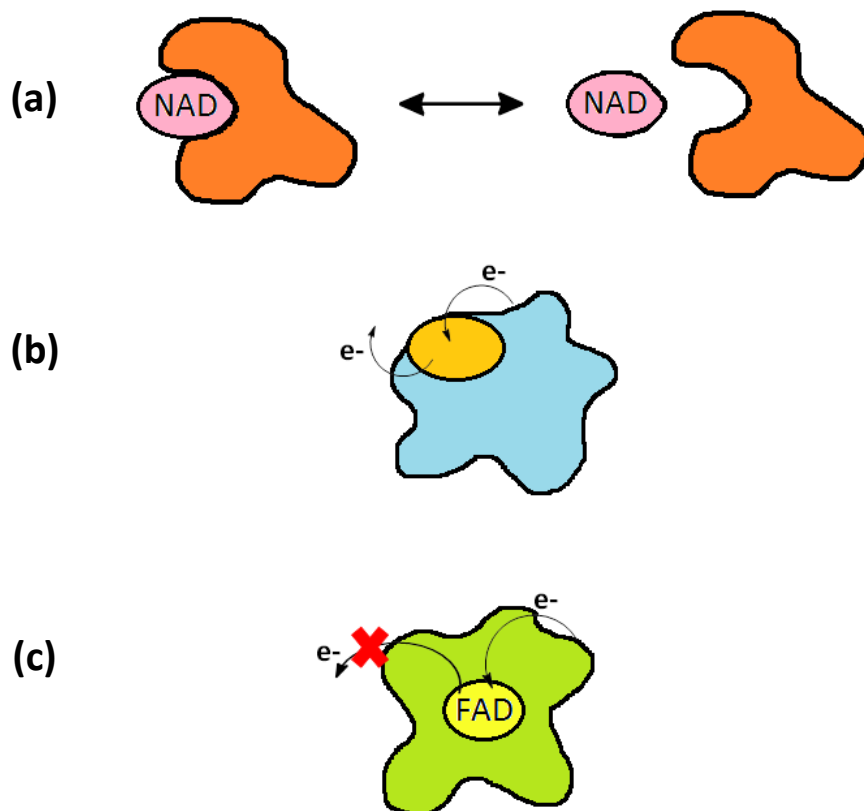


**Figure 1.10:** Different types of enzymes used as biofuel cell catalysts. (a) Weakly bound coenzymes, (b) active site located near surface, and (c) active site buried inside enzyme. Image reproduced from ref. [86]

### 1.9.3. Electron transfer pathways

Energy generation in biofuel cells usually involves electrons produced from biocatalysis between the active site and the substrate. In an enzymatic biofuel cell, a redox process occurs when a substrate binds with the active site of the

enzyme. The electron gained from the redox process is transferred from the active site to the electrode. These electrons are transferred to the electrode surface by two different mechanisms depending on the electrode setup (Figure 1.11). In mediated electron transfer (MET) process the enzyme is not directly attached to the surface of the electrode. Therefore redox mediators are necessary for electron transfer from the active site to the electrode. In the direct electron transfer process, the enzymes are attached to the electrode such that the active site is as close to the surface of the electrode as possible. The electrons formed during biocatalysis are then directly transferred to the electrode surface. Direct electron transfer (DET) only can occur for weakly bound active sites and active sites located at the surface. DET is normally not seen in enzymes with buried active sites; however, there are ways to systematically immobilize the enzyme to achieve DET. This will be explained in a later section.

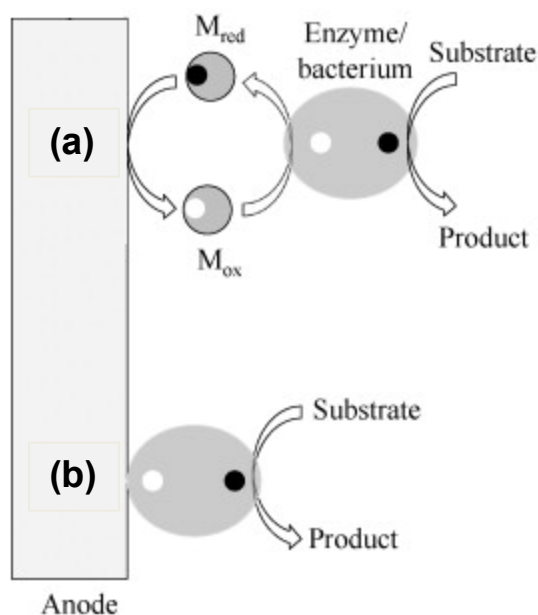


**Figure 1.11:** Electron transfer mechanism in biofuel cells. (a) Mediated electron transfer using redox mediators (b) Direct electron transfer from active site of enzyme to electrode surface. Image reproduced from ref. [89]

#### 1.9.4. Biofuel cell applications and problems

Currently, proton exchange membrane (PEM) fuel cells are commercially available and one of the most highly researched fields in fuel cell technology. Biofuel cells that use glucose as the fuel is highly attractive and promising for implantable devices or sensors since glucose is found in relatively high concentrations in the blood stream [85-86]. Biofuel cells are also highly attractive for wastewater treatment. It has been shown that microbial biofuel cells can help remove pollutants from wastewater by a bioremediation method [90].

Unlike certain PEM fuel cells that use hydrogen as a fuel, biofuel cells do not have any problems with fuel storage. Theoretically, concentrated glucose has a high energy density and up to 6 kWhr of electricity can be obtained upon complete oxidation [91]. However, the maximum power density achieved currently is 1 mW/cm<sup>2</sup> [92], which is three orders less than that of a typical PEM fuel cell [93]. The main problems associated with biofuel cells include immobilization of the biocatalysts, enzyme stability, mass transfer, and power density [94].

#### **1.9.4.1. Enzyme stability**

Most enzymatic biofuel cells are only stable for a few days. There are many factors that can limit the lifetime of enzymatic biofuel cells. In most cases, the stability of the biocatalysts determines the lifetime. In MET enzymatic biofuel cells the redox mediators can also limit the lifetime of the biofuel cell [95-96]. To avoid this problem, enzymes are normally immobilized on the electrodes surface. Immobilization of the enzyme can help extend its lifetime [97-99]. Biofuel cells with glucose oxidase and bilirubin oxidase immobilized with a redox polymer was shown to be stable for up to 20 days.

#### **1.9.4.2. Mass Transfer**

Similar to chemical fuel cells, biofuel efficiency is also limited by mass transfer. In biofuel cells there are three types of mass transfer that can reduce the efficiency [94]. The three mass transfer resistances are: 1) in MET, the

resistance from the diffusion of the redox mediators from the biocatalysts to the electrodes and in DET, the resistance from electron transfer from the active site to the electrode. 2) proton transfer from the anode to cathode through the membrane. 3) diffusion of the fuels or oxidant to the active site of the catalysts. Immobilization of enzymes is normally used to avoid the problem associated with mass transfer resistance from redox mediators.

#### **1.9.4.3. Enzyme immobilization and power density**

Enzyme immobilization is important for several reasons. First, it allows the repeated use of the catalysts. The electrode can be washed and then reused. Second, and arguably the most important, it facilitates DET between the active site and the electrode. The close contact of the active to the electrode surface is vital for DET. As the distance between the active site and the electrode increases, the resistance is increased, resulting in a lower electron transfer rate and a slower overall reaction. In this case, the rate determining step would be the electron conduction. If the active is very close to the electrode surface, then the enzymatic reaction kinetics becomes the rate determining step. However, in many cases the insulating protein shell of the enzyme causes slow DET. There have been a number of reports on increasing DET by immobilizing enzymes on CNTs or in polymer matrices [100-103]. To increase the DET rate of the biocatalytic oxidation of glucose, glucose oxidase has been directly immobilized onto the surface of CNTs [100]. It was found that the immobilization of glucose

oxidase directly on CNTs facilitated the DET. It was also found that the DET of glucose oxidase was a two electron transfer coupled with a two proton transfer process. The rate constant was found to be  $\sim 1.53\text{s}^{-1}$ , which is quite low. It was also shown that enzymes such as  $\text{NAD}^+$  dehydrogenases can be immobilized by trapping it in a nafion polymeric matrix [102]. Using this method, power densities as high as  $2.04\text{ mW/cm}^2$  were obtained. These electron transfer rates and power densities using polymers and carbon nanotubes are fairly low and it is possibly due to their low conductivity and large contact resistance, respectively. It has been reported that the formation of conducting carbon nanotube polymer composites can increase the conductivity dramatically [28-29, 104]. The immobilization of enzymes on conducting carbon nanotube polymer composites would theoretically reduce the resistance and possibly increase the electron transfer rate. The use of conducting carbon nanotubes composites for biofuel cells, however, has not been reported. Furthermore, enzymes can also be immobilized onto the surface using a reconstitution approach [105]. Reconstitution of the enzyme involves separating the embedded redox cofactor from the enzyme and immobilizing the cofactor onto the electrode first. After the immobilization of the cofactor, it is attached back to the apo-enzyme. This approach physically places the active site in close contact with the electrode surface, facilitating DET and increasing electron transfer rate.

Based on the all this, the main focus will be on improving the direct electron transfer rate from the active site to the electrode surface and the overall



reaction rate of the anode in a biofuel cell using conducting carbon nanotube polymer composites. In addition, the orientation of the enzyme immobilized on the electrode surface by a reconstitution approach will be studied.

## **1.10 Carbon nanotubes for Molecular Detection**

### **1.10.1. Electronic and optical detection**

Inspired by its remarkable electronic and optical properties SWNTs have been used to develop molecular sensing devices. One widely studied device is based on field effect transistors (FETs), in which individual SWNTs are used as the active channel. The device development has revolutionized our ability to detect single molecules [35]. The detection mechanism for the high sensitivity is the extremely sensitive modulation of the electrical conductance of a semiconducting SWNT by electrostatic gating or doping through charge transfer between SWNTs and adsorbed molecules. However, devices using single nanotubes have the major flaw of irreproducibility due to challenges in assembling individual tubes into the required positions with atomic level precision [106].

Another difficulty is the careful separation of semiconducting tubes from the metallic ones since most of the current SWNT fabrication techniques produces a mixture of metallic and semiconducting nanotubes [106-107], while only semiconducting nanotubes exhibit a large conductance change in response

to electrostatic and chemical gating effects desired for chemical sensors [35, 108-109]. SWNT networks have been explored as an alternative configuration to solve this problem [110-111]. SWNT networks can be mass produced, and done so at low cost and high efficiency, ideal for practical applications [112-115]. The devices based on SWNT networks exhibit reproducible characteristics because the electronic properties of the network are averaged over a large number of nanotubes [116-117]. However, the relative simplicity comes with a loss in detection sensitivity due to the co-existence of both semiconducting and metallic nanotubes in the network.

Carbon nanotubes have also been intensively explored to develop optical based sensing approaches for biological *in vitro* and *in vivo* molecular sensing and imaging applications in recent years due to their unique properties [118]. Specifically, SWNTs absorb and emit strongly in the near infrared (NIR), where human tissues and biological fluids are transparent. Furthermore, their NIR emission is highly sensitive to changes in the local dielectric environment but remains stable to permanent photo-bleaching for prolonged molecular detection with single molecular sensitivity. Once again, separation of semiconductor tubes and metallic tubes is required because the existence of metallic tubes would quench the NIR fluorescence of SWNTs, resulting in significant decrease in detection sensitivity.

On the other hand, all carbon nanomaterials including carbon nanotubes, graphite, graphene, even amorphous carbon exhibit extremely strong plasmon absorption in the ultraviolet region. This strong absorption has been studied as undesired optical background for the visible and NIR absorption based applications. In this thesis, we will report our exploration of this abnormally strong plasmon absorption to develop a new sensing platform for metallic ions. Compared to the previous reported FET and NIR fluorescence approaches, the new sensing platform can reach the same or better detection sensitivity and detection limits simply by using UV absorption spectroscopy. It does not require any device fabrication and/or NIR resource, which are not accessible in a lot of labs. Most importantly, separation of semiconducting and metallic tubes is not required, simplifying the sensing development and application. Finally, detection selectivity can be realized by modifying the surface of SWNTs with molecular ligands for specific metal ions. As a demonstration, the new detection method is applied to selectively detect iron ions ( $\text{Fe}^{3+}$ ) in an aqueous solution.  $\text{Fe}^{3+}$  was chosen because it is an essential element for the growth and metabolism of all marine organisms. Therefore the ability to selectively and sensitively detect  $\text{Fe}^{3+}$  is critical to the study of carbon sequestration in the ocean and consequently global climate changes.

### 1.10.2. Raman Scattering of Carbon nanotubes for molecular detection and imaging

Another unique optical property of carbon nanotubes which is highly attractive for molecular detection is their distinctive resonance-enhanced Raman signatures for Raman detection/imaging. Raman scattering spectra of SWNTs normally shows resonance enhanced Raman bands at 150-300  $\text{cm}^{-1}$ , 1590-1600  $\text{cm}^{-1}$ , and  $\sim 2600 \text{ cm}^{-1}$ . The bands at 150-300  $\text{cm}^{-1}$ , called the radial breathing mode (RBM) vibration, is an out-of-plane phonon mode where the carbon atoms move in the radial direction. The RBM is a unique phonon mode of SWNTs which is a direct indication of the existence of SWNTs in a CNT sample. The RBM frequency is inversely proportional to the CNT diameter [119]. This phonon mode is normally used to determine and characterize the chirality of SWNTs [13-18]. However, it is normally not used for molecular sensing applications due to their relatively low signal intensity.

The peak located at 1590-1600  $\text{cm}^{-1}$  is the G-band, which originates from the tangential stretching mode of the carbon atoms in the nanotubes [14]. Due to the high intensity of this band, it is widely used for detection of SWNTs within cells and living animals with high sensitivity. Furthermore, its full-width half-maximum (FWHM) is smaller than 2 nm, allowing for high degrees of multiplicity for simultaneous imaging with many colors [120-122]. In contrast to the NIR fluorescence, which is only emitted by semiconducting SWNTs, Raman scattering occurs for both metallic and semiconducting SWNTs. The scattering

exhibits resonance enhancement when incident light coincides with an optical transition of the nanotube, the Raman cross sections can reach  $5.7 \times 10^{-21} \text{ cm}^2 \text{ sr}^{-1} \text{ molecule}^{-1}$  for a 1  $\mu\text{m}$  nanotube excited at 785 nm, which is the highest known cross sections for single molecules. Due to the high Raman scattering cross-section of SWNTs and resonance enhancement at near IR absorption transitions, Raman scattering of nanotubes is easily detectable and unmistakable. Furthermore, it does not blink or quench and will not diminish under prolonged excitations. More importantly, the intensity of G band is relatively insensitive to the diameter and bundling of nanotubes. This is very different from it's the RBM, which behaves similarly to the NIR fluorescence of SWNTs and is sensitive to nanotube bundling and dielectric coating on the surface of nanotubes [123-124]. In contrast to NIR fluorescence, the G band is also relatively insensitive to the type of noncovalent coatings and the solution environment of SWNTs. Due to all these advantages, Raman spectroscopy of SWNTs provide tremendous benefits for robust *in vitro* and *in vivo* imaging and sensing.

Very recently, we constructed an anti-HER2 IgY – SWNT complex by chemically conjugating anti-HER2 IgY (chicken antibody with high specificity for HER2 expressing receptors) onto the surface of microwaved functionalized SWNTs [125]. The complex was shown to successfully detect and destroy HER2-expressing breast cancer cells *in vitro*. Raman spectroscopy was used to detect the specific binding of the IgY antibody moiety from the complex to the

HER2 receptor on the cancer cells. We demonstrated that single cancer cells can be detected and selectively eradicated while leaving the nearby normal cells unharmed. The major difference from previous reports is that internalization by cancer cells is not required in order to achieve the selective photothermal ablation, thus offering the advantage of being more easily extended to other cancer types. However, we found that Raman signal from the carbon nanotubes was very low compared with the cancer cell background. We attribute this weak signal to the microwave dispersed carbon nanotubes, which largely destroyed the conjugated structure of the CNTs. With this in mind, we have developed a new method for the construction of IgY HER2 antibody-functionalized SWNTs with the intrinsic properties of SWNTs largely preserved. The resultant IgY-SWNT complex display improved optoelectronic properties for its application in the detection and selective destruction of breast cancer cells.

## **1.11 Objective of Thesis**

The main aim of the thesis is to provide a fundamental understanding of how the electronic structures and surface chemistry of carbon nanotubes influence the kinetics during a conducting polymer composite fabrication and stability after its fabrication. The knowledge gained from these studies will be applied to develop an efficient biofuel cell anode. Along the same line, we also study how the electronic structures of carbon nanotubes influence the development of sensitive and selective molecular detection devices.

## 1.12 References

1. Gogotsi, Y., *Carbon Nanomaterials*. 2006: Taylor & Francis.
2. Kumar, C.S.S.R., *Carbon Nanomaterials*. 2011: John Wiley & Sons.
3. Spencer, J.N., G.M. Bodner, and L.H. Rickard, *Chemistry: Structure & Dynamics*. 2010: John Wiley & Sons.
4. Kroto, H.W., et al., *C60: Buckminsterfullerene*. *Nature*, 1985. **318**: p. 162-163.
5. Iijima, S., *Helical microtubules of graphitic carbon*. *Nature*, 1991. **354**: p. 56-58.
6. Novoselov, K.S., et al., *Electric Field Effect in Atomically Thin Carbon Films* *Science*, 2004. **306**: p. 666-669.
7. Rolison, D.R., *Properties of Nanostructured Materials: Chemical Properties*, in *Nanomaterials: Synthesis, Properties and Applications*, A.S. Edelstein and R.C. Cammarata, Editors. 1996, Taylor & Francis.
8. Varadan, W.K., et al., *Nanoscience and Nanotechnology in Engineering*. 2010: World Scientific Publishing Co.
9. Harris, P.J.F., *Carbon Nanotubes and Related Structures*. 1999: Cambridge University Press.
10. Reilly, R.M., *Carbon Nanotubes: Potential Benefits and Risks of Nanotechnology in Nuclear Medicine*. *J. Nuclear Med.*, 2007. **48**: p. 1039-1042.
11. Charlier, J.-C., X. Blase, and S. Roche, *Electronic and transport properties of nanotubes*. *Rev. Mod. Phys.*, 2007. **79**: p. 677-732.
12. Wilder, J.W.G., et al., *Electronic structure of atomically resolved carbon nanotubes*. *Nature*, 1997: p. 59-62.
13. Dresselhaus, M.S., et al., *Raman spectroscopy on isolated single wall carbon nanotubes*. *Carbon*, 2002. **40**: p. 2043-2061.
14. Dresselhaus, M.S., et al., *Raman Spectroscopy of Carbon Nanotubes*. *Physics Reports*, 2005. **409**: p. 47-99.
15. Dresselhaus, M.S., et al., *Raman Spectroscopy of Carbon Nanotubes*, in *Contemporary Concepts of Condensed Matter Science - Carbon Nanotubes: Quantum Cylinders of Graphene*, E. Burstein, et al., Editors. 2008, Elsevier B.V.
16. Dresselhaus, M.S. and P.C. Eklund, *Phonons in carbon nanotubes*, in *Advances in Physics*. 2000, Taylor & Francis Ltd. p. 705-814.
17. Saito, R., et al., *Raman intensity of single-wall carbon nanotubes*. *Phys. Rev. B*, 1997. **57**: p. 4145-4153.
18. Thomsen, C. and S. Reich, *Raman Scattering in Carbon Nanotubes*, in *Light Scattering in Solid*, M. Cardona and R. Merlin, Editors. 2007, Springer-Verlag Berlin Heidelberg.

19. Hatton, R.A., A.J. Miller, and S.R.P. Silva, *Carbon Nanotubes: A Multi-Functional Materials for Organic Optoelectronics*. J. Mater. Chem. , 2008. **18**: p. 1183-1192.
20. Ando, T., *The electronic properties of graphene and carbon nanotubes*. Asia Materials, 2009. **1**: p. 17-21.
21. Dai, H.J., et al., *Electrical Transport Properties and Field Effect Transistors of Carbon Nanotubes*. NANO: Brief Reports and Reviews, 2006. **1**: p. 1-4.
22. Zhou, X., et al., *Band Structure, Phonon Scattering, and the Performance Limit of Single-Walled Carbon Nanotube Transistors*. Phys. Rev. Lett., 2005. **95**.
23. Durkop, T., et al., *Extraordinary Mobility in Semiconducting Carbon Nanotubes*. Nano Lett., 2004. **4**: p. 35-39.
24. Li, S., et al., *Carbon Nanotube Transistor Operation at 2.6 GHz*. Nano Lett., 2004. **4**: p. 753-756.
25. Hong, S. and S. Myung, *Nanotube Electronics: A flexible approach to mobility*. Nat. Nanotech., 2007. **2**: p. 207-208.
26. Kang, S.J., et al., *High-Performance Electronics Using Dense, Perfectly Aligned Arrays of Single-Walled Carbon Nanotubes*. Nat. Nanotech., 2007. **2**: p. 230-236.
27. Kis, A. and A. Zettl, *Nanomechanics of carbon nanotubes*. Phil. Trans. R. Soc. A, 2008. **366**: p. 1591-1611.
28. Cheung, W., et al., *Fabrication of High Performance Conducting Polymer Nanocomposites for Biosensors and Flexible Electronics: Summary of the Multiple Roles of DNA Dispersed and Functionalized Single Walled Carbon Nanotubes*. J. Mater. Chem., 2009. **19**: p. 6465 - 6480.
29. Ma, Y., et al., *Improved Conductivity of Carbon Nanotube Networks by In Situ Polymerization of a Thin Skin of Conducting Polymer*. ACS Nano, 2008. **2**: p. 1197-1204.
30. Nijuguna, J., K. Pielichowski, and J.R. Alcock, *Epoxy-Based Fibre Reinforced Nanocomposites*. Adv. Eng. Mater., 2007. **9**: p. 835-847.
31. Prashantha, K., et al., *Present Status and Key Challenges of Carbon Nanotubes Reinforced Polyolefins: A Review on Nanocomposites Manufacturing and Performance Issues*. Polymer & Polymer Composites, 2009. **17**: p. 205-245.
32. Lassagne, B., et al., *Coupling Mechanics to Charge Transport in Carbon Nanotube Mechanical Resonators*. Science, 2009. **325**: p. 1107-1110.
33. Kim, P., et al., *Thermal Transport Measurements of Individual Multiwalled Nanotubes*. Phys. Rev. Lett., 2001. **87**.
34. Chen, J., et al., *Solution Properties of Single-Walled Carbon Nanotubes*. Science, 1998. **282**: p. 95-98.
35. Kong, J., et al., *Nanotube Molecular Wires as Chemical Sensors*. Science, 2000. **287**: p. 622-625.
36. Liu, J., et al., *Fullerene Pipes*. Science, 1998. **280**: p. 1253-1256.



37. Collins, P.G., et al., *Extreme Oxygen Sensitivity of Electronic Properties of Carbon Nanotubes* Science, 2000. **287**: p. 1801-1804.
38. Banerjee, S., T. Hemraj-Benny, and S.S. Wong, *Covalent surface chemistry of single-walled carbon nanotubes*. Adv. Mater., 2005. **17**: p. 17-29.
39. Hirsch, A., *Functionalization of single-walled carbon nanotubes*. Angew. Chem. Int. Ed., 2002. **41**: p. 1853-1859.
40. Ros, T.G., et al., *Surface Oxidation of Carbon Nanofibres*. Chem. Eur. J., 2002. **8**: p. 1151-1162.
41. Khabashesku, V.N., W.E. Billups, and J.L. Margrave, *Fluorination of Single-Wall Carbon Nanotubes and Subsequent Derivatization Reactions*. Acc. Chem. Res., 2002. **35**: p. 1087-1095.
42. Zheng, M., et al., *DNA-assisted dispersion and separation of carbon nanotubes*. Nat. Mater., 2003. **2**: p. 338-342.
43. Chiang, C.K., et al., *Electrical Conductivity in Doped Polyacetylene*. Phys. Rev. Lett., 1977. **39**: p. 1098-1101.
44. Scrosati, B., *Application of electroactive polymers*. 1993: Chapman & Hall.
45. Wan, M., *Conducting Polymers with Micro or Nanometer Structure*. 2008: Springer.
46. De Jesus, M.C., Y. Fu, and R.A. Weiss, *Conductive Polymer Blends Prepared by In Situ Polymerization of Pyrrole: A Review*. Polym. Eng. Sci., 1997. **37**: p. 1936-1943.
47. Macdiarmid, A.G., et al., *"Polyaniline": Interconversion of Metallic and Insulating Forms*. Mol. Cryst. Liq. Cryst., 1985. **121**: p. 173-180.
48. Petrova, J.N., et al., *Fully Doped Oligomers of Emeraldine Salt: Polaronic versus Bipolaronic Configuration*. Phys. Chem. B., 2011. **115**: p. 3765-3776.
49. Shoji, E. and M.S. Freund, *Potentiometric Saccharide Detection Based on the pKa Changes of Poly(aniline boronic acid)*. J. Am. Chem. Soc., 2002. **124**: p. 12486-12493.
50. Akhtar, M., et al., *Polyaniline thin film electrochromic devices*. Synth. Met., 1988. **26**: p. 203-208.
51. Hosseini, S.H. and A.A. Entezami, *Preparation and characterization of polyaniline blends with polyvinyl acetate, polystyrene and polyvinyl chloride for toxic gas sensors*. Polym. Advan. Technol., 2001. **12**: p. 482-493.
52. Ren, J., et al., *A new B-PAn-P system for the detection of bacteria population*. Sensor Actuator B, 2007. **125**: p. 510-516.
53. Macdiarmid, A.G., et al., *Polyaniline: Electrochemistry and application to rechargeable batteries*. Synth. Met., 1987. **18**: p. 393-398.
54. Jin, Z., Y. Su, and Y. Duan, *An improved optical pH sensor based on polyaniline*. Sens. Actuator B-Chem., 2000. **71**: p. 118-122.
55. Liu, H., et al., *Polymeric Nanowire Chemical Sensor*. Nano Lett., 2004. **4**: p. 671-675.

56. Sadek, A.Z., et al., *Doped and dedoped polyaniline nanofiber based conductometric hydrogen gas sensors*. Sens. Actuator A-Phys, 2007. **139**: p. 53-57.
57. Ćirić-Marjanovića, G., M. Trchová, and J. Stejskalb, *MNDO-PM3 Study of the Early Stages of the Chemical Oxidative Polymerization of Aniline*. Czech. Chem. Commun, 2006. **71**: p. 1407-1426.
58. Sapurina, I. and J. Stejskal, *The mechanism of the oxidative polymerization of aniline and the formation of supramolecular polyaniline structures*. Polym. Int., 2008. **57**: p. 1295-1325.
59. Stejskal, J., et al., *Oxidation of Aniline: Polyaniline Granules, Nanotubes, and Oligoaniline Microspheres*. Macromolecules, 2008. **41**: p. 3530–3536.
60. Geniès, E.M., M. Lapkowski, and J.F. Penneau, *Cyclic voltammetry of polyaniline: interpretation of the middle peak*. J. Electroanal. Chem. Inter. Electrochem., 1988. **249**: p. 97-107.
61. Ćirić-Marjanović, G., M. Trchová, and J. Stejskal, *The chemical oxidative polymerization of aniline in water: Raman spectroscopy*. J. Raman Spectrosc., 2008. **39**: p. 1375-1387.
62. Dmitrieva, E., Y. Harima, and L. Dunsch, *Influence of Phenazine Structure on Polaron Formation in Polyaniline: In Situ Electron Spin Resonance–Ultraviolet/Visible–Near-Infrared Spectroelectrochemical Study*. J. Phys. Chem. B, 2009. **113**: p. 16131–16141.
63. Kriz, J., et al., *NMR Investigation of Aniline Oligomers Produced in the Early Stages of Oxidative Polymerization of Aniline*. J. Phys. Chem. B, 2009. **113**: p. 6666-6673.
64. Ma, Y., et al., *The Electronic Role of DNA-Functionalized Carbon Nanotubes: Efficacy for in Situ Polymerization of Conducting Polymer Nanocomposites*. J. Am. Chem. Soc., 2008. **130**: p. 7921-7928.
65. Sivakumar, C., T. Vasudevan, and A. Gopalan, *Chemical Oxidative Polymerization and in situ Spectrochemical Studies of a Sulfonated Aniline Derivative by UV-Visible Spectroscopy*. Ind. Eng. Chem., 2001. **40**: p. 40-51.
66. Tzou, K. and R.V. Gregory, *Kinetic Study of the Chemical Polymerization of Aniline in Aqueous Solutions*. Synth. Met., 1992. **47**: p. 267-277.
67. Wei, Y., et al., *A study of the mechanism of aniline polymerization*. J. Polym. Sci. A, 2003. **27**: p. 2385-2396.
68. Yue, J. and A.J. Epstein, *Synthesis of self-doped conducting polyaniline*. J. Am. Chem. Soc., 1990. **112**: p. 2800-2801.
69. Karyakin, A., I.A. Maltsev, and L.V. Lukachova, *The influences of defects in polyaniline structure on its electroactivity: optimizatin of 'self-doped' polyaniline synthesis*. J. Electroanal. Chem., 1996. **402**: p. 217-219.
70. Ajayan, P.M., et al., *Aligned Carbon Nanotube Arrays Formed by Cutting a Polymer Eesin-Nanotube Composite*. Science, 1994. **265**: p. 1212-1214.
71. Cochet, M., et al., *Synthesis of a New Polyaniline/Nanotube Composite: "in-situ" Polymerisation and Charge Transfer through Site-Selective Interaction*. Chem. Comm., 2001: p. 1450-1451.

72. Dai, L. and A.W.H. Mau, *Controlled Synthesis and Modification of Carbon Nanotubes and C60: Carbon Nanostructures for Advanced Polymeric Composite Materials*. Adv. Mater., 2001. **13**: p. 899-913.
73. Sainz, R., et al., *Soluble Self-Aligned Carbon Nanotube/Polyaniline Composites*. Adv. Mat., 2005. **17**: p. 278-281.
74. Zengin, H., et al., *Carbon Nanotube Doped Polyaniline*. Adv. Mater., 2002. **14**: p. 1480-1483.
75. Zheng, M., et al., *Structure-Based Carbon Nanotube Sorting by Sequence-Dependent DNA Assembly*. Science, 2003. **302**: p. 1545-1548.
76. Ma, Y.F., et al., *In-situ Fabrication of A Water-Soluble, Self-Doped Polyaniline Nanocomposite: the Unique Role of DNA Functionalized Single-Walled Carbon Nanotubes*. J. Am. Chem. Soc., 2006. **128**: p. 12064-12065.
77. Liu, W., et al., *The Role of Template in Enzymatic Synthesis of Conducting Polyaniline*. J. Am. Chem. Soc., 1999. **121**: p. 11345-11355.
78. Li, X.H., et al., *Fabrication and Characterization of Well-Dispersed Single-Walled Carbon Nanotube/Polyaniline Composites*. Carbon, 2002. **41**: p. 1670-1673.
79. Chen, R.J., et al., *Noncovalent Sidewall Functionalization of Single-Walled Carbon Nanotubes for Protein Immobilization*. J. Am. Chem. Soc., 2001. **123**: p. 3838-3839.
80. Wang, Y., Z. Iqbal, and S. Mitra, *Rapidly Functionalized, Water-Dispersed Carbon Nanotubes at High Concentration*. J. Am. Chem. Soc., 2006. **128**: p. 95-99.
81. Tu, X.M., et al., *DNA sequence motifs for structure-specific recognition and separation of carbon nanotubes*. Nature, 2009. **460**: p. 250-253.
82. Napier, M.E., D.O. Hull, and H.H. Thorp, *Electrocatalytic oxidation of DNA-wrapped carbon nanotubes*. J. Am. Chem. Soc., 2005. **127**: p. 11952-11953.
83. Lucente-Schultz, R.M., et al., *Antioxidant Single-Walled Carbon Nanotubes*. J. Am. Chem. Soc., 2009. **131**: p. 3934-3941.
84. Watts, P.C.P., et al., *Carbon nanotubes as polymer antioxidants*. J. Mater. Chem., 2003. **13**: p. 491-495.
85. Shukla, A.K., et al., *Biological fuel cells and their applications*. Curr. Sci., 2004. **87**: p. 455-469.
86. Bullen, R.A., et al., *Biofuel cells and their development*. Biosens. Bioelec., 2006. **21**: p. 2015-2045.
87. Palmore, G.T.R. and G.M. Whitesides, *Microbial and Enzymatic Biofuel Cells*, in *Enzymatic Conversion of Biomass for Fuels Production*, M.E. Himmel, J.O. Baker, and R.P. Overend, Editors. 1994. p. 271-290.
88. Gomez, C., S. Shipovskov, and E.E. Ferapontova, *Peroxidase biocathodes for a biofuel cell development*. J. Renewable and Sustainable Energy, 2010. **2**.

89. Osman, M.H., A.A. Shah, and F.C. Walsh, *Recent progress and continuing challenges in bio-fuel cells. Part I: Enzymatic cells*. Biosens. Bioelec., 2011. **26**: p. 3087-3102.
90. Gil, G.-C., et al., *Operational parameters affecting the performannce of a mediator-less microbial fuel cell*. Biosens. Bioelectron., 2003. **18**: p. 327-334.
91. Sokic-Lazic, D., et al., *Oxidation of Biofuels: Fuel Diversity and Effectiveness of Fuel Oxidation through Multiple Enzyme Cascades*. Electroanal., 2010. **22**: p. 757-764.
92. Logan, B.E., et al., *Microbial Fuel Cells: Methodology and Technology*. Environ. Sci. Technol., 2006. **40**: p. 5181-5192.
93. Cheng, S., H. Liu, and B.E. Logan, *Increased performance of single-chamber microbial fuel cells using an improved cathode structure*. Electrochem. Commun., 2006. **8**: p. 489-494.
94. Kim, J., H. Jia, and P. Wang, *Challenges in biocatalysis for enzyme-based biofuel cells*. Biotech. Adv., 2006. **24**: p. 296-308.
95. Allen, R.M. and H.P. Bennetto, *Microbial fuel-cells: electricity production from carbohydrates*. Appl. Biochem. Biotechnol., 1993. **39**: p. 27-40.
96. Barton, S.C., J. Gallaway, and P. Atanassov, *Enzymatic biofuel cells for implantable and microscale devices*. Chem. Rev., 2004. **104**: p. 4867-4886.
97. Kang, C., et al., *Deactivation of bilirubin oxidase by a product of the reaction of urate and O<sub>2</sub>*. Bioelectrochem., 2004. **65**: p. 83-88.
98. Katz, E., B. Filanovsky, and I. Willner, *A biofuel cell based on two immiscible solvents and glucose oxidase and microperoxidase-11 monolayer-functionalized electrodes*. New J Chem, 1999. **23**: p. 481-487.
99. Willner, I., et al., *Biofuel cell based on glucose oxidase and microperoxidase-11 monolayer-functionalized electrodes*. J Chem Soc, Perkin Transact 2, 1998: p. 1817-1822.
100. Cai, C. and J. Chen, *Direct electron transfer of glucose oxidase promoted by carbon nanotubes*. Anal. Biochem., 2004. **332**: p. 75-83.
101. Giuseppi-Elie, A., C. Lei, and R.H. Baughman, *Direct electron transfer of glucose oxidase on carbon nanotubes*. Nanotechnology, 2002. **13**: p. 559-564.
102. Minteer, S.D., N.L. Akers, and C.M. Moore, *Enzyme immobilization for use in biofuel cells and sensors.*, U.S.P.A. Publication, Editor. 2004.
103. Zhao, Y.-D., et al., *Direct electron transfer of glucose oxidase molecules adsorbed onto carbon nanotube powder microelectrode*. Anal. Sci., 2002. **18**: p. 939-941.
104. Ma, Y., et al., *Enhanced Sensitivity for Biosensors: Multiple Functions of DNA-Wrapped Single-Walled Carbon Nanotubes in Self-Doped Polyaniline Nanocomposites*. J. Phys. Chem. B, 2006. **110**: p. 16359-16365.

105. Willner, I., et al., *Electrical Wiring of Glucose Oxidase by Reconstitution of FAD-Modified Monolayers Assembled onto Au-Electrodes*. J. Am. Chem. Soc., 1996. **118**: p. 10321-10322.
106. Hu, L., D.S. Hecht, and G. Grüner, *Percolation in Transparent and Conducting Carbon Nanotube Networks*. Nano Lett., 2004. **4**: p. 2513-2517.
107. Chen, R.J., et al., *Noncovalent Functionalization of Carbon Nanotubes for Highly Specific Electronic Biosensors*. Proc. Natl. Acad. Sci., 2003. **100**: p. 4984-4989.
108. Boussaad, S., et al., *In situ Detection of Cytochrome c Adsorption with Single Walled Carbon Nanotube Device*. Chem. Comm., 2003: p. 1502-1503.
109. Kong, J. and H. Dai, *Full and Modulated Chemical Gating of Individual Carbon Nanotubes by Organic Amine Compounds*. J. Phys. Chem. B, 2001. **105**: p. 2890-2893.
110. Qi, P.F., et al., *Toward Large Arrays of Multiplex Functionalized Carbon Nanotube Sensors for Highly Sensitive and Selective Molecular Detection*. Nano Lett., 2003. **3**: p. 347-351.
111. Star, A., et al., *Lable-Free Detection of DNA Hybridization Using Carbon Nanotube Network Field Effect Transistors*. Proc. Natl. Acad. Sci., 2006. **103**: p. 921-926.
112. Kaempgen, M., G.S. Duesberg, and S. Roth, *Transparent Carbon Nanotube Coatings*. Appl. Surf. Sci., 2005. **252**: p. 425-429.
113. Wu, Z., et al., *Transparent, Conductive Carbon Nanotube Films*. Science, 2004. **305**: p. 1273-1276.
114. Zhang, D., et al., *Transparent, Conductive, and Flexible Carbon Nanotube Films and Their Application in Organic Light-Emitting Diodes*. Nano Lett., 2006. **6**: p. 1880-1886.
115. Artukovic, E., et al., *Transparent and Flexible Carbon Nanotube Transistors*. Nano Lett., 2005. **5**: p. 757-760.
116. Grüner, G., *Carbon Nanotube Films for Transparent and Plastic Electronics*. J. Mater. Chem., 2006. **16**: p. 3533-3539.
117. Li, J., et al., *Carbon Nanotube Sensors for Gas and Organic Vapor Detection*. Nano Lett., 2003. **3**: p. 929-933.
118. Cheung, W. and H. He, *Carbon Nanotubes: In Vitro and In Vivo Sensing and Imaging*, in *Biosensor Nanomaterials*, S.J. Li, et al., Editors. 2011, WILEY-VCH Verlag GmbH & Co KGaA. p. 127-159.
119. Zhang, Y., et al., *Substrate-Induced Raman Frequency Variation for Single-Walled Carbon Nanotubes*. J. Am. Chem. Soc., 2005. **127**: p. 17156-17157.
120. Chen, Z., et al., *Protein microarrays with carbon nanotubes as multicolor Raman labels*. Nat. Biotech., 2008. **26**: p. 1285-1292.
121. Liu, Z., et al., *Multiplexed Multicolor Raman Imaging of Live Cells with Isotopically Modified Single Walled Carbon Nanotubes*. J. Am. Chem. Soc., 2008. **130**: p. 13540-13541.

122. Liu, Z., et al., *Multiplexed Five-Color Molecular Imaging of Cancer Cells and Tumor Tissues with Carbon Nanotube Raman Tags in the Near-Infrared*. Nano Res., 2010. **3**: p. 222-233.
123. Peters, M.J., et al., *Structural Phase Transition in Carbon Nanotube Bundles under Pressure*. Phys. Rev. B, 2000. **61**: p. 5939-5944.
124. Rao, A.M., et al., *Diameter-Selective Raman Scattering from Vibrational Modes in Carbon Nanotubes* Science, 1997. **275**: p. 187-191.
125. Xiao, Y., et al., *Anti-HER2 IgY Antibody-Functionalized Single Walled Carbon Nanotubes for Detection and Selective Destruction of Breast Cancer Cells*. BMC Cancer, 2009. **9**.

## **Chapter 2**

# **DNA Functionalized SWNTs as Molecular Catalytic Templates: DNA Sequence Dependent Catalytic Efficacy**

## **2.1 Introduction**

Since their discovery, carbon nanotubes have been explored for their potential applications in various fields due to their highly remarkable electronic, mechanical, and optical properties. These properties arise from their unique electronic and atomic structures. Furthermore, they have been exploited for potential applications in nanoelectronics, energy storage, molecular sensing, and for reinforcing composite materials [1]. One of the unique features of carbon nanotubes is that every atom is located on its surface; hence it is not surprising that in recent years there has been much attention focused on molecular engineering of carbon nanotube surfaces (surface functionalization, solubilization) for the exploration and development of their properties and applications.

The ability to manipulate the surface properties of carbon nanotubes is of crucial importance for their utilization in different applications. Surface modification can cause its electronic structure to change; therefore studying its surface properties can theoretically allow the control of its properties for various

purposes. For example, it has been shown that covalent side-wall modification of carbon nanotube surfaces can impact its electrical and mechanical properties [2]. This is especially important for the application of carbon nanotubes in reinforcing composite materials and for building electronic devices.

Within the last decade, conducting polymers have also attracted considerable attention due to their unique combination of properties not displayed by any other known materials. Conducting polymers are used in a variety of applications including batteries, electrochromic displays, light-emitting diodes, printed circuit boards, sensors, and flexible electronics [3]. Although they offer various interesting properties such as high mechanical flexibility and tunable electronic properties [4], their conductivities are much lower compared with inorganic semiconductors such as silicon. It is well known that the  $\pi$ -conjugated system of a conducting polymer has a great impact on its electronic properties, and thus is responsible for its conductivity [5]. Consequently, abundant research has been conducted over the past decade focused on enhancing the conductivities of conducting polymers by improving their conjugation [6-7].

Moreover, one of the most studied conducting polymers is polyaniline (PANI) due to its ease of synthesis, its electrochromic behavior, good stability, and high conductivity. In an effort to increase their electrical properties, researchers have focused on producing high molecular weight PANI and its derivatives by studying the aniline (ANI) polymerization reaction. Polymerization parameters such as the initial aniline monomer concentration [8-9], initial oxidant



concentration [8-9], solution pH [8, 10], reaction temperature [8-9, 11], and ANI monomer to oxidant ratio [9] have been studied along with their affect on the resulting polymer's molecular weight, electronic structures, and molecular structures, all three of which contributes to the conductivity of PANI. For example, it was found that ANI polymerization at reduced temperatures (0°C or lower) yields PANI with higher conductivities, molecular weights (5-10 times higher), and viscosities [9, 11-13]. Conversely, ANI polymerization at room temperature produces PANI with low molecular weights and high defect sites [14]. Defect sites on the PANI backbone are defined as any structural deformation of the polyaniline linear chain that disrupts its conjugated structure such as chain branching, cross-linking, and oligomer formation.

In an effort to further improve the conductivity as well as other properties, carbon nanotubes have been synergistically combined with various polymers to form polymer carbon nanotube composites [15-17]. In a recent study, we have discovered that poly(aniline boronic acid) (PABA), a derivative of PANI, polymerized in situ with ssDNA wrapped SWNT (ssDNA-SWNT) not only can increase the composite's conductivity but also increases the polymerization rate by approximately 4500 times compared to that of pure PABA during the first 10 minutes of polymerization [18]. This is highly attractive because it allows the production of highly conductive polymer/CNT composite materials in an efficient manner. Tzou *et al.* [19] have shown that adding different substrates into the reaction mixture can increase the polymerization rate and it is primarily due to an

increase in surface area where the polymer can be deposited. Although the surface area plays an important role in increasing the polymerization rate, other studies were carried out to determine factors that may also contribute to the rate of polymerization. Ma *et al.* [18] studied the interaction between the ssDNA–SWNT and 3-aminophenylboronic acid (ABA) monomers, a derivative of ANI. It was concluded that a charge transfer complex is formed when electron deficient ABA monomers form  $\pi$ -stacking interactions with the electron rich carbon nanotube surface. This causes the ABA monomers to become electron rich, making it easier for it to be oxidized during the polymerization process, thus increasing its polymerization rate. In addition, carbon nanotube poly(aniline boronic acid) composite (CNT/PABA) have been shown to have conductivities of up to two orders of magnitude higher than that of pure PABA [20-22]. It is noteworthy to mention that in order to achieve these interesting properties, the ssDNA–SWNT must be polymerized in situ with the ABA monomers and not mixed separately after the PABA is formed [23].

Inspired by the dramatic increase in polymerization rate and conductivity by simply introducing ssDNA–SWNT into the reaction mixture, and with the goal of efficiently producing highly conductive PABA composites, we further investigated how ssDNA–SWNT contributes to this “catalytic behavior”. **Specifically, in this chapter, we will study how different sequences of DNA (30T, 15GT) used to disperse the CNTs affect PABA formation. Essentially we hypothesize that the surface properties and the electronic structures of**

**the CNTs will be altered upon dispersion with the different DNA strands and therefore can influence how the PABA is formed.** Catalytic effect of different types of DNA (ssDNA, dsDNA) and different types of CNTs (SWNT, MWNT) will also be mentioned. To the best of our knowledge, this is the first case where a detailed study of the manipulation of carbon nanotube surface properties has on the rate of ABA polymerization.

## 2.2 Results and Discussion

### 2.2.1. Dispersion of carbon nanotubes

The dispersion of CNTs has been intensely studied since they were discovered and efficient dispersion is vital for preserving the CNT's superior properties. To study the effect that carbon nanotubes have on PABA formation, we first dispersed the carbon nanotubes into aqueous solution using a method proposed by Zheng *et al.* [24], which is described in the experimental section in detail. The SWNTs were dispersed with different types of DNA, namely, double stranded DNA (dsDNA), single stranded DNA with a 30T sequence (ssDNA(30T)), and single stranded DNA with a 15GT sequence (ssDNA(15GT)). The MWNT was dispersed with only ssDNA(30T). The aim of using these four differently dispersed CNTs (dsDNA–SWNT, ssDNA(30T)–SWNT, ssDNA(15GT)–SWNT, and ssDNA(30T)–MWNT) is to study various different combinations that can be formed which may impact the formation of PABA during the polymerization process. More specifically, we want to look at the four combinations to study the surface properties of the following three cases on ABA polymerization: MWNT compared with SWNT, ssDNA–SWNT compared with dsDNA–SWNT, and the affect of using different sequences of DNA dispersed CNTs.

After the dispersion process, the samples were purified and characterized using UV-Vis spectroscopy to ensure that individually dispersed SWNTs were present in solution. Characteristic absorption peaks are usually observed for individual SWNTs in the visible to near IR region due to van Hove singularities [25-26] and is normally considered a good qualitative indicator of individually dispersed SWNTs in solution. Furthermore, the presence of prominent peaks at the visible and near-IR region known as the van Hove singularities indicate that the aromatic surface of the SWNTs is not altered and its unique electronic properties are preserved. The van Hove singularities originate from optical transitions in the valence band of SWNTs. In contrast, bundled SWNTs cause significant broadening of the peaks and this is primarily due to the interactions between these bundled tubes, causing the van Hove singularities to be absent from the spectrum [27]. A representative UV-Vis spectrum of the DNA dispersed SWNT is shown in figure 2.1a. As illustrated in the figure, there is a large absorption band at ~260nm and a collection of absorption peaks from 400-1300nm. The absorption band at 260nm is attributed to the  $\pi$ -plasmon band of SWNT and absorption of DNA on the SWNTs. The collection of absorption peaks from 400-1300nm is due to van Hove singularities of SWNTs with different chiralities and diameters [28-29].

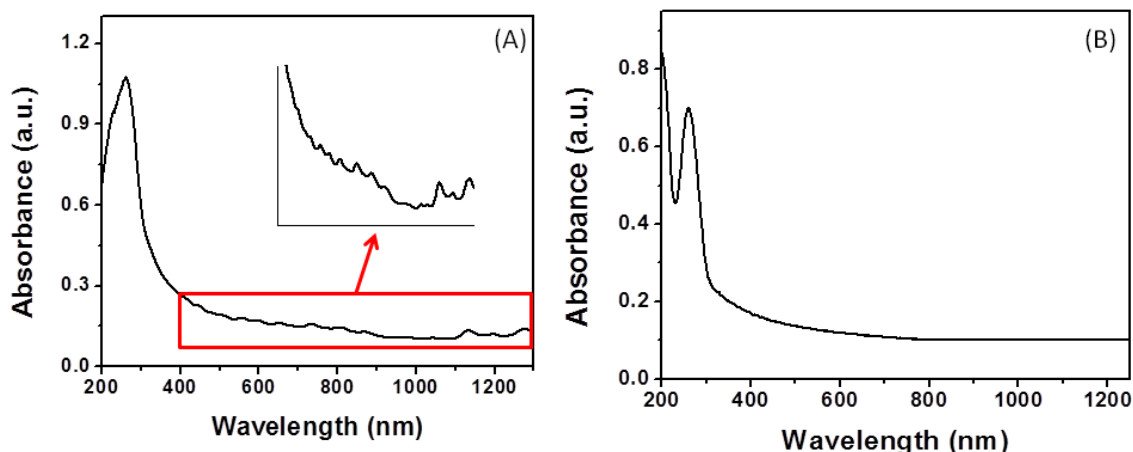


**Figure 2.1:** Typical UV-Visible spectrum of (a) DNA dispersed single-walled carbon nanotube (b) DNA dispersed multi-walled carbon nanotube.

Unlike the case of DNA dispersed SWNTs, the absorption spectrum of individually dispersed MWNTs do not show the typical van Hove singularities (Figure 2.1b). This may be due to the coupling interactions between each adjacent concentric shell in the MWNTs [30-32]. Although there have been a number of studies on the optical transitions for isolated SWNTs, the effect of shell coupling on the optical transitions in MWNTs are quite complex and not fully understood [30-32].

### 2.2.2. Monolayer formation of ABA on CNT surface

One important consideration is to ensure that the polymerization process studied is only from the polymer formed on the carbon nanotube surface and not

from free polymer formed in solution. Thus, it is essential to determine the concentration of ABA monomers (3-aminophenylboronic acid) required to fully cover the surface of the CNTs prior to polymerization. Based on previous studies, ABA monomers are expected to form charge transfer complexes with the CNT surface [18]. Upon forming the complex, the electron deficient ABA monomers are expected to withdraw electrons from the electron rich CNTs. Since the electronic structure of carbon nanotubes has been shown to be highly sensitive to charge transfer reactions [27, 33], UV-Vis-NIR spectroscopy can be utilized to determine the amount of ABA required to fully cover the CNT surface.

Figure 2.2 shows the interaction of different concentrations of ABA monomers with a 70mg/L solution of ssDNA–SWNT. It is shown that as electrons are withdrawn from CNTs, absorption bleaching is observed at the near-IR range until 5mM of ABA is added to the CNT solution. This is consistent with previous reports where CNTs were shown to experience absorption bleaching at the near-IR region after partial oxidation from dissolved oxygen [34-35]. At this point, the CNT surface is assumed to be fully covered with ABA monomers through  $\pi$  – stacking interactions.

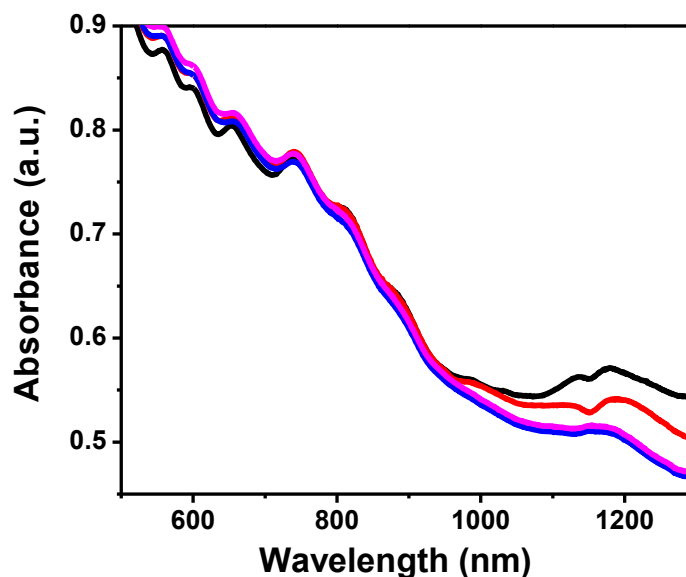


**Figure 2.2:** UV-Vis-NIR spectrum showing interaction between 70mg/L ssDNA(30T)-SWNT solution with different concentrations of ABA monomers: 0mM (black), 2mM (red), 4mM (magenta), 5mM (blue).

### 2.2.3. Polymerization Kinetics of DNA–CNT/ABA

One approach that can be used to study the polymerization process is by monitoring the reaction and determining its kinetics. Understanding the kinetics of polymerization processes is of fundamental importance for efficiently producing polymeric materials for a wide variety of applications. A thorough comprehension of the kinetics can help explain the polymer formation mechanism that leads to the production of highly conductive polymer composite materials.

Several groups have studied the kinetics of ANI polymerization using a wide range of techniques. Wei et al. [36] studied the rate of PANI formation



electrochemically by utilizing cyclic potential sweep techniques and determined that the rate of PANI formation at the electrode is correlated with the anodic peak current. This suggests that the rate can be monitored by increases in the anodic peak current. Using a different approach, Tzou and Gregory [19] studied the kinetics of chemical polymerization of ANI by monitoring the rate of ANI monomer depletion using gas chromatography. Recently, the kinetics of polymerization of an aniline derivative was also explored using UV-Visible spectroscopy by Sivakumar *et al.* [37]. Sivakumar studied polymer formation by monitoring its absorption increase, which is directly proportional to the concentration of polymer formed, according to the Beer's Law.

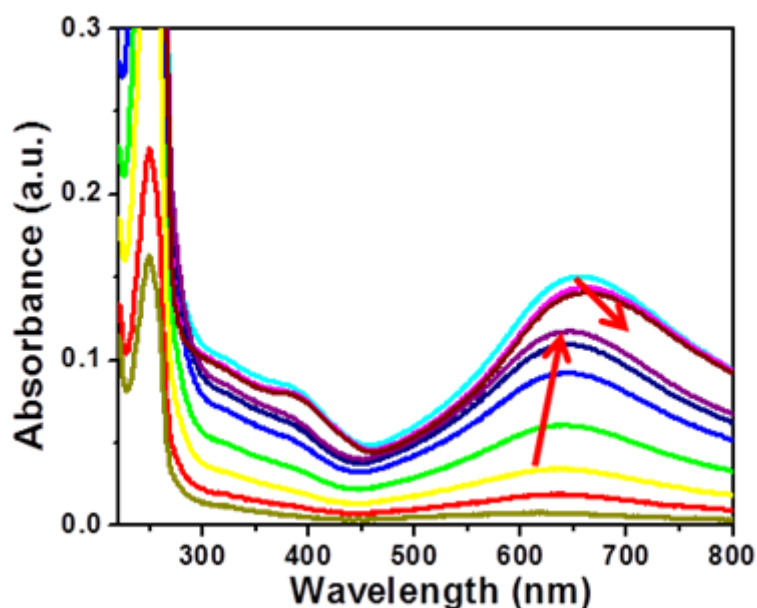


**Figure 2.3:** Typical UV-Visible spectra of ABA polymerization in the presence of DNA– CNT. The arrows indicate the increase and red shift of the emeraldine absorption peak

Using a similar process to Sivakumar *et al.* [37], we studied the effect of different DNA dispersed CNTs on the kinetics of ABA polymerization using UV-Visible spectroscopy. After forming the ABA–SWNT charge transfer complex, ammonium persulfate (APS), a strong oxidizing agent, was added to the solution to initiate the polymerization reaction and the absorption spectra was taken at various time intervals (Figure 2.3). There are three absorption bands that are normally shown; the absorption at ~260nm due to the  $\pi - \pi^*$  transition of aniline, DNA on the SWNTs, and possibly the  $\pi$  plasmon band of SWNTs [38-39], the absorption at ~390nm due to the polaron transition [38, 40-41] of polyaniline or to the quinone diimine structure of low molecular weight oligomers [42], and the absorption band at ~650nm which ultimately red-shifts to ~800nm (not shown in Figure 2.3) due to the bipolaron transition which can be associated with charge carriers in the polymer chain [38]. Thus, the increase of the absorption band at ~650nm during polymerization can be used to monitor PABA formation and to study the kinetics of polymerization. The extinction coefficient of PABA at ~650nm and ~800nm is approximately the same and the average is used for kinetic calculations.

Moreover, there are several trends that are apparent from the polymerization of ABA in the presence of different DNA-CNTs shown in figure 2.3. At the early stages of the polymerization reaction, the absorption band at ~650nm is essentially absent; indicating that little or no polymer is formed. As the polymerization progresses, the polymer peak increases in intensity and shifts to

higher wavelength, suggesting an increase in the amount of polymer formed and an increase in polymer conjugation length. Eventually the absorption intensity will reach a maximum and begin to decrease, while continuing to shift to higher wavelengths. As we will see later, the red shift and decrease in intensity seen is most likely due to the reduction of the pernigraniline state of PABA to the emeraldine state.

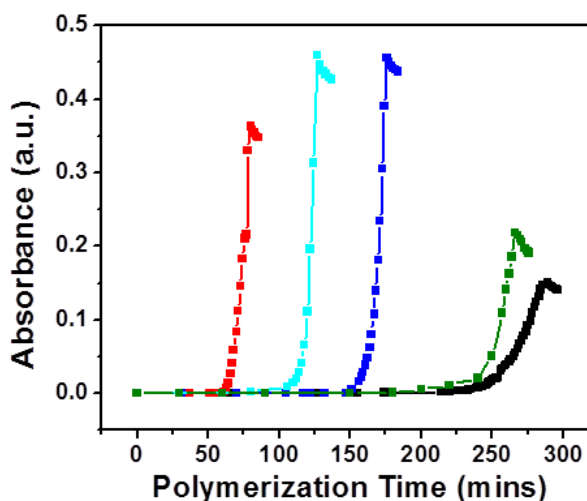


**Figure 2.4:** Kinetic profile of ABA polymerization in the presence of ssDNA–MWNT (red), ssDNA(30T) –SWNT (cyan), ssDNA(15GT) –SWNT (blue), ssDNA(30T) (green), and no CNTs (pristine PABA, black) in acidic medium. In situ polymerization reaction was performed at 4°C

To investigate the polymerization process of ABA with different DNA–CNTs, the polymer absorption intensity was plotted as a function of polymerization time to obtain their kinetic profiles. The representative kinetic profiles for each of the polymerization process are shown in Figure 2.4. Experiments were performed at least 3 times for each curve shown and the

maximum difference in polymerization time for all curves was 7 mins, therefore this process is fairly reproducible. The polymerization of “pure” ABA (no DNA–CNTs were added) and ssDNA(30T) (only the DNA strand is added and no CNTs) are also included as controls. As shown in the figure, ABA polymerized in the presence of any DNA–CNT results in a dramatic rate enhancement compared with pure ABA polymerization, which is consistent with previous reports [18, 20]. Furthermore, it is apparent that DNA by itself (green curve) can increase the polymerization rate, however unlike in the case of CNT dispersed with DNA; the rate enhancement is quite small. More surprisingly, however, is the fact that different sequence of DNA used to disperse the CNTs seems to affect the polymerization rate.

In addition, it can be seen that the kinetic profiles for all polymerization studies are similar. Normally the kinetic profile for ABA polymerization can be divided into three separate regions or phases; the initiation, the autocatalytic (propagation), and termination stages. During the beginning and throughout most of the polymerization process, the absorption intensity is extremely low indicating that polymer formation during this initiation phase is slow. It is generally thought that the nucleation process occurs during this stage (formation of the N-phenylphenazine type cationic initiator as shown in the polymerization mechanism in the introduction) and is the preparatory phase before the dramatic increase in polymerization rate during the autocatalytic stage. The rate constant for the initiation stage is represented as  $k_1$ . As shown in Table 1,  $k_1$  is normally

very small. In Figure 2.4, the autocatalytic stage is represented by the remarkable increase in the polymerization rate and PABA formation. According to literature [18, 20, 36-37], the large increase in polymerization rate (shown in mechanism in the introduction as the stage where cationic polymerization occurs) is most likely due the catalytic effect from formed polyaniline. The formed polyaniline has a low oxidation potential compared with aniline oligomers and monomers in solution [43]. This specific characteristic of the formed polymer is important because the oxidant in solution will preferentially oxidize it compared with the oligomers and monomers. Furthermore, the oxidized polymer can be reduced by the oligomers and monomers resulting in an increase in oxidized monomers which can participate in the polymerization process. This characteristic is more prominent in the presence of CNTs since ABA can be stacked on the surface of CNTs creating a preconcentration effect [18]. The rate constant for the autocatalytic stage is represented as  $k_2$  and is normally very large compared with  $k_1$  due to the dramatic increase in polymerization speed compared to the initiation stage. The last stage of ABA polymerization is the termination stage. As the name suggests, this indicates the end of the polymerization process. This occurs if all the monomer or the oxidant is used up. As mentioned earlier, the formed polymer is preferentially oxidized compared with the oligomers and monomers due to its lower oxidation potential. This suggests that the PABA formed is normally in its fully oxidized pernigraniline state and this is evident from the appearance of the peak at ~600-700nm in the UV-Vis spectrum. As the polymerization process enters the termination stage,

either the ABA monomers or the APS oxidant is depleted. If the oxidant is depleted then the oxidized PABA will be reduced by the ABA monomers converting the PABA from the fully oxidized non-conductive pernigraniline state to the half oxidized conductive emeraldine state [43]. This is represented in the UV spectrum by the decrease in intensity at the 600-700nm region and the increase in intensity at the 700-800nm region. In addition, since the emeraldine state is energetically more stable and favored compared with the pernigraniline state in solution; a shift to longer wavelengths is expected. It is noteworthy to mention that in order to form the emeraldine state, the concentration of the monomer is in excess at the end of polymerization. If however, the oxidant concentration is in excess at the end of polymerization the polymer formed will remain in the fully oxidized pernigraniline state (Figure 2.5). Note that the use of very high concentrations of APS will cause the formation of oligomers rather than polymer (Figure 2.5).

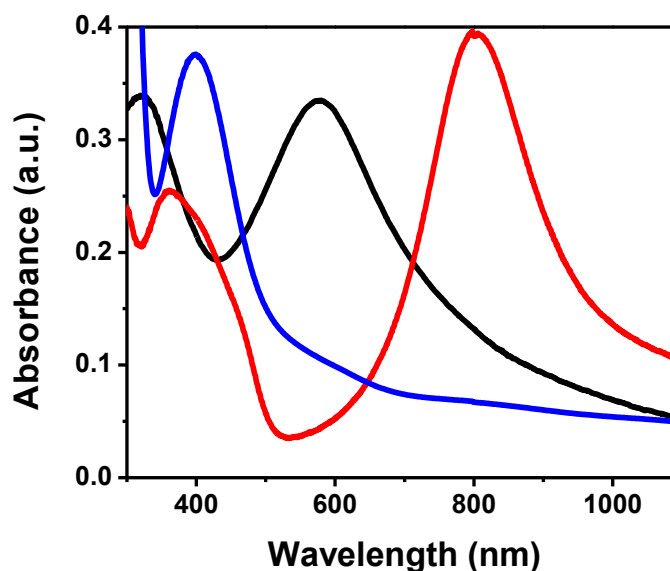


**Figure 2.5:** UV-Visible spectrum showing pure PABA polymerized with an APS to ABA molar ratio of 0.25 (blue), 0.16 (black), and 0.11 (red)

To explore the different polymerization rates more in detail, the kinetic equation and the rate constants were determined. There have been various kinetic models that are described in literature for the polymerization of aniline and its derivatives [18-19, 36-37, 42]. The earliest studies on the kinetics of electrochemical polymerization of ANI showed that the rate of PANI formation is highly dependent on the initial monomer concentration, the oxidant concentration, and the concentration of polymer formed [19, 36-37]. In addition, Sivakumar *et al.* [37] demonstrated that the kinetic equation proposed by other researchers can be simplified if the produced polymer is soluble in solution and therefore the autocatalytic effect from the formed polymer is negligible. The simplified kinetic equation was used in our previous work when only the first 10

minutes of polymerization was studied [18], where the system remained in the homogeneous state. In our present case, however, we studied the entire polymerization process and therefore surface effects from the formed polymer are highly important. Based on all the considerations above, the kinetic equation used for this study is:

$$\frac{d[\text{PABA}]}{dt} = k_1[\text{ABA}][\text{APS}] + k_2[\text{ABA}][\text{PABA}] \quad (1)$$

where [ABA] represents the concentration of ABA monomers, [APS] represents the concentration of APS (the oxidizer), [PABA] represents the concentration of PABA formed, and  $k_1, k_2$  represents the observed rate constants. The rate constant  $k_2$  includes the surface factor contribution from PABA. Using equation (1) for all the polymerizations shown in Figure 2.6, a table of rate constants can be obtained (Table 2.1). All rate constants were determined using the kinetics simulation software Kintecus.

	$k_1$ (L mg <sup>-1</sup> min <sup>-1</sup> )	$k_2$ (L mg <sup>-1</sup> min <sup>-1</sup> )
Pure PABA	0.004726 ± 3.1%	0.8223 ± 0.6%
ssDNA (30T)/PABA	0.01199 ± 2.4%	1.436 ± 0.2%
ssDNA-SWNT (15GT)/PABA	0.03294 ± 3.7%	4.420 ± 0.4%
ssDNA-SWNT (30T)/PABA	0.03994 ± 1.1%	4.969 ± 0.2%
ssDNA-MWNT/PABA	0.04841 ± 0.9%	5.104 ± 0.1%

**Table 2.1:** Comparison of polymerization rate constants for the acidic polymerization of ABA in the presence of different CNTs and different sequences of DNA



## **2.2.4. Origin of catalytic effect**

Based on the last section, there are several questions that remain unanswered. Firstly, why does the presence of dsDNA dispersed SWNT give a higher polymerization rate than ssDNA dispersed SWNT? Secondly and arguably the most interesting is why does changing the sequence of the DNA on SWNT yield different polymerization rates? Finally, why does the presence of DNA dispersed with MWNT give a higher polymerization rate than DNA dispersed with SWNT? Section 2.2.4.1 will explore the catalytic role of DNA and SWNT in the polymerization process in hopes of answering the first two questions. The difference in polymerization rates between DNA dispersed with MWNT and SWNT will be briefly mentioned in section 2.2.4.2.

### **2.2.4.1. Catalytic role of SWNT and DNA**

The different polymerization rates shown by ssDNA(15GT)-SWNT and ssDNA(30T)-SWNT may be due to several possibilities. First, it could be a result of the different sequence of DNA used to disperse the SWNTs. The electronic and chemical properties may change depending upon the sequence of DNA used and therefore affect the rate of polymerization. Second, since the SWNTs used were not purified by chirality, their metallic to semiconducting ratios might be different [24, 44-45]. Semiconducting SWNTs normally have a small band gap and there is no band gap for metallic SWNTs [46]; hence their electronic

properties are different. These different properties can influence the rate of ABA polymerization.

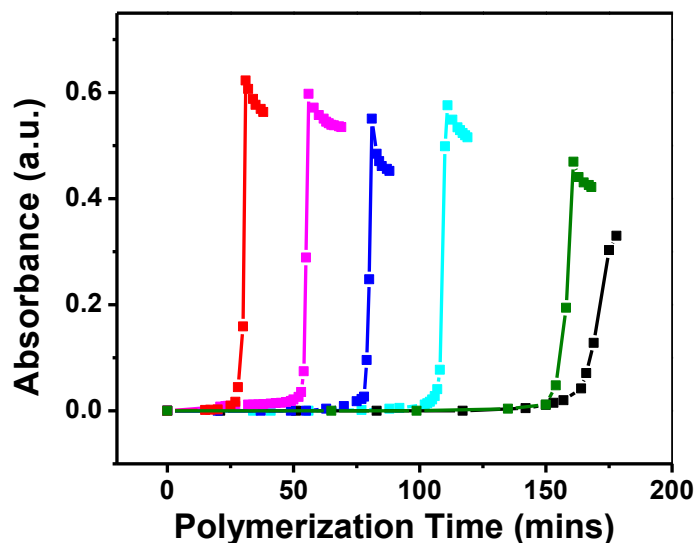


**Figure 2.6:** Kinetic profile of ABA polymerization in the presence of ssDNA–MWNT (red), dsDNA–SWNT (magenta), ssDNA(15GT)–SWNT (blue), ssDNA(30T)–SWNT (cyan), ssDNA(30T) (green), and no CNTs (pristine PABA, black) in neutral medium. In situ polymerization reaction was performed at 4°C

To further analyze the role of the carbon nanotubes in speeding up the polymerization processes, the polymerization was also studied in neutral conditions. Figure 2.6 shows the kinetic profile of ABA polymerization in the presence of different CNTs, different DNA strands and sequences in neutral medium. The polymerization kinetics trend for the neutral approach is similar to that of the acidic approach, except for a few differences. One difference is that the polymerization rate for the neutral approach is much faster than its acidic counterpart. One possibility is that in the neutral polymerization approach,

fructose is normally added into the polymerization mixture so it binds with the boronic acid moiety on the ABA monomer. This forms an anionic boronic ester complex which may increase the polymerization rate. Also, due to the steric effect from the bulky ester complex, it is possible that the addition of monomers favors the para position during the polymerization process. There may be other explanations and further research must be done in order to truly explain the phenomenon seen. Note also that dsDNA-SWNT is included in the neutral polymerization approach.

	$k_1$ (L mg <sup>-1</sup> min <sup>-1</sup> )	$k_2$ (L mg <sup>-1</sup> min <sup>-1</sup> )
Pure PABA	0.02902 ± 2.1%	4.686 ± 0.3%
ssDNA (15GT)/PABA	0.03853 ± 1.3%	9.486 ± 0.1%
ssDNA-SWNT (30T)/PABA	0.05974 ± 1.2%	24.98 ± 0.1%
ssDNA-SWNT (15GT)/PABA	0.06615 ± 1.2%	30.10 ± 0.2%
dsDNA-MWNT/PABA	0.09722 ± 1.5%	32.53 ± 0.2%
ssDNA-MWNT/PABA	0.1449 ± 0.5%	34.51 ± 0.1%

**Table 2.2:** Comparison of polymerization rate constants for the neutral polymerization of ABA in the presence of different CNTs and different sequences of DNA

#### **2.2.4.1.1. Catalytic role of dsDNA and ssDNA**

The dsDNA-SWNT was not included in the acidic polymerization study solely because it was found that dsDNA-SWNT is unstable at low pH conditions and forms aggregates. From the neutral approach, it was found that the rate of polymerization is much faster for dsDNA-SWNT than ssDNA-SWNT. The difference in rate may be due to the extra stability provided by the duplex structure of dsDNA. Pang *et al.* [47] have studied the electrochemical oxidation of dsDNA and ssDNA adsorbed on gold electrode and found that oxidation occurs much easier for ssDNA due to its exposed nucleobases. This suggests that ssDNA can donate its electrons more efficiently than dsDNA. During the polymerization reaction there are two competing events that can occur; DNA may transfer its electrons to either the APS or to the CNTs. On one hand, if the electrons are transferred to the CNTs, this would increase the electron density of the ABA monomers adsorbed onto the DNA-CNT, facilitating the rate of polymerization. On the other hand, if DNA is oxidized by the APS then the polymerization rate would not increase since there is no increase in electron density on the ABA monomers. Based on these considerations and the data shown in figure 2.8, ssDNA-SWNT may be oxidized more readily than dsDNA-SWNT, resulting in a lower polymerization rate for ssDNA-SWNT than dsDNA-SWNT.

#### **2.2.4.1.2. Catalytic role of metallic and semiconducting SWNT**

One important and interesting data obtained from Figure 2.6 and table 2.2 is that the trend for the polymerization rate of ABA in the presence of ssDNA(30T)-SWNT and ssDNA(15GT)-SWNT in the neutral approach are reversed compared with the acidic approach. In the acidic approach, ssDNA(30T)-SWNT had a faster polymerization rate than ssDNA(15GT)-SWNT, whereas in the neutral approach the roles are inverted. One possible explanation for this is that metallic SWNTs do not have a band gap compared to semiconducting SWNTs and are more prone to be oxidized in acid conditions possibly by dissolved oxygen in the solution [48]. This is especially true in acidic medium where concentrated acid is known to cause covalent functionalization of CNTs [2]. Covalent functionalization of CNT surfaces can disrupt its band structure, therefore affect its electronic properties [2].

As mentioned before, ssDNA/SWNT may have different metallic to semiconducting tube ratios prior to purification and one reason for this is due to the surfactant used to disperse them (ex: different types of DNA) [24, 44-45]. To eliminate this effect and further understand what type of CNTs play the “catalytic role” in the observed different polymerization profiles, we selectively eliminated the metallic CNTs from the dispersed solution. Removal of metallic CNTs has been accomplished by various methods including anion exchange chromatography [45] and density gradient centrifugation [44]. More recently, elimination of metallic CNT have been achieved by using microwave irradiation

[49]. The absorption of microwave energy is governed by the material's dielectric constant. Materials with different dielectric constants absorb microwave energy and heat up selectively [49-50]. Metallic CNTs have been shown to have a higher dielectric constant than water which has a higher dielectric constant than semiconducting CNTs [51]. Consequently, when irradiated with microwave energy, the metallic CNTs preferentially heats up to a high local temperature much faster than semiconducting CNTs and are selectively destroyed. This process can be monitored in two ways: by UV-Vis spectroscopy and Raman spectroscopy.

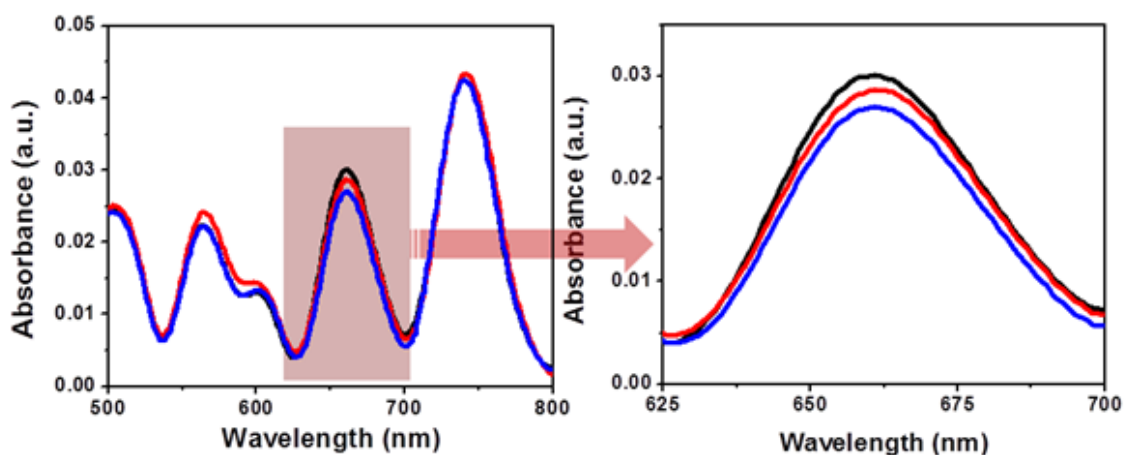


**Figure 2.7:** (left) UV-Visible spectrum of ssDNA(15GT)-SWNT at different microwave irradiation times: 0 min (black), 1 min (red), 3 min (blue). The UV spectrum shown is after background correction using method proposed by [52]. (right) Zoomed in image of shaded area.

As mentioned in the previous chapter, the UV-Vis spectrum of CNTs show van Hove singularities from 400nm-1300nm. The van Hove singularities from

400nm to ~650nm are due to optical transitions from metallic CNT and the peaks seen from 650nm to 1300nm are due to optical transitions from semiconducting CNT. Thus, according to Priya *et al.* [53] it is possible to monitor the degradation of metallic CNT using UV-Vis by the decrease in the van Hove peak at ~600-700nm as a function of microwave irradiation time after background correction using a method proposed by Nair *et al.* [52]. Figure 2.7 shows the UV-Vis spectrum of the degradation of metallic CNTs at different microwave irradiation times for ssDNA(15GT)-SWNT. As shown, as microwave irradiation time increases, the absorption intensity at ~625-700nm decreases. This indicates that microwave irradiation selectively destroys and removes metallic CNTs from the solution.

To verify that metallic SWNTs are preferentially destroyed, Raman spectroscopy was also used to monitor this process. Raman is a very powerful tool and is used widely in literature to characterize SWNTs. A typical Raman spectrum of ssDNA(15GT)-SWNT is shown by the black curve (0 min) in Figure 2.8a. When analyzing the Raman spectrum of SWNTs, there are normally three important regions of interest, namely the G band, the D band, and the bands from the radial breathing mode (RBM). The G band ranges from  $\sim 1550\text{-}1600\text{cm}^{-1}$  and is a result of tangential vibrations of the carbon atoms on the SWNT [46, 51]. In addition, it is usually composed of two peaks: the one at  $\sim 1570\text{cm}^{-1}$  due to vibrations along the circumference of the nanotube and the one at  $\sim 1590\text{cm}^{-1}$  due to vibrations along the nanotube axis [46, 51, 54]. The peak at  $1590\text{cm}^{-1}$

known as the  $G^+$  peak is important for describing the electrical properties and bonding structure of SWNTs. The  $G^-$  peak at  $1570\text{cm}^{-1}$  is known to be sensitive to the type of SWNT present and can be used to determine whether the nanotube is metallic or semiconducting [46]. It has been demonstrated in literature that the  $G^+$  peak is normally higher in intensity than the  $G^-$  peak in both semiconducting and metallic SWNTs, however the  $G^-$  peak for metallic SWNTs is usually much broader than semiconducting SWNTs [54]. The disorder-induced D-band occurs at  $\sim 1300\text{cm}^{-1}$  and originates from amorphous impurities and structural defects on the SWNTs and is usually used to qualitatively determine the quality of SWNTs in the sample. The RBM occurs at  $\sim 120\text{-}350\text{cm}^{-1}$  and is due to the radial vibrations of the carbon atoms on the SWNT. The RBM is one of the most useful features and can be used to determine if SWNT is present in the sample, the diameter of the SWNT, and if the sample contains metallic or semiconducting SWNTs [46].



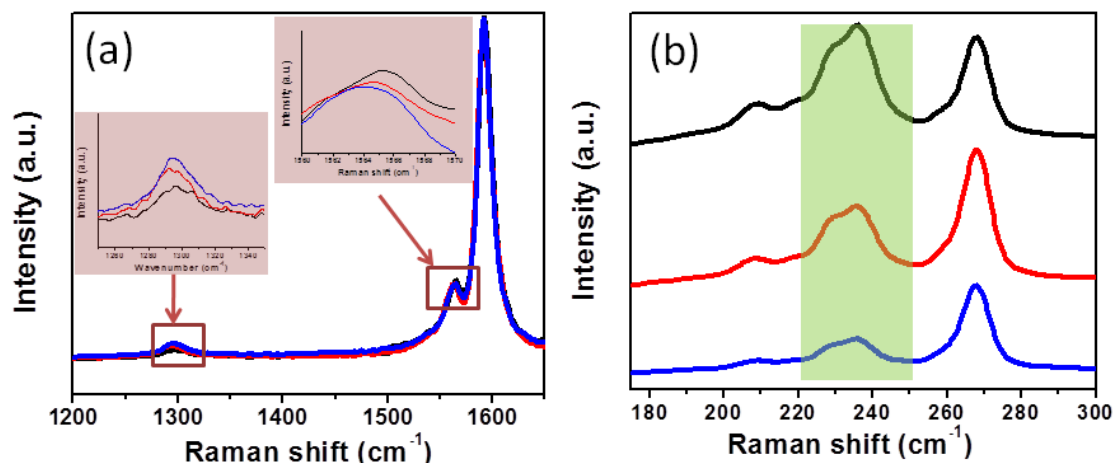


**Figure 2.8:** Raman spectrum showing (a) the D-band and G band of ssDNA(15GT)-SWNT (b) the radial breathing mode for ssDNA(15GT)-SWNT at different microwave irradiation times: 0 min (black), 1 min (red), 3 min (blue).

The Raman spectrum of ssDNA(15GT)-SWNT at different microwave irradiation times is shown in Figure 2.8. In Figure 2.8a, the G<sup>+</sup> band shows a decrease in intensity and the D band shows an increase in intensity as the sample is subjected to longer irradiation time. This suggests that the SWNTs that are eliminated are most likely metallic. However, the increase in D band intensity indicates that there are defects formed. The defects might be due to partially destroyed metallic SWNTs that have precipitated out of solution which can be seen by eye after microwave irradiation (Centrifugation was used to remove the insoluble material after microwave irradiation). Furthermore, the RBM in Figure 2.8b shows that the region from  $\sim 220\text{-}250\text{cm}^{-1}$ , which originates from metallic SWNT decreases as a function of microwave irradiation time and the region from  $260\text{-}280\text{cm}^{-1}$ , originating from semiconducting SWNT remains essentially the

same. To see this more clearly, the ratio of  $I_{236}/I_{268}$  was calculated and compared. The intensity ratios for 0, 1, and 3 mins microwave times were 1.04, 0.75, and 0.41, respectively. Combining the UV-Vis and Raman results, we have concluded that microwave irradiation have preferentially eliminated the metallic SWNT from our samples. After microwave irradiation, the concentrations of both samples were re-determined using UV-Vis spectroscopy. Assuming that all the metallic SWNTs were removed, the concentration determined using UV-Vis is only from semiconducting SWNTs.

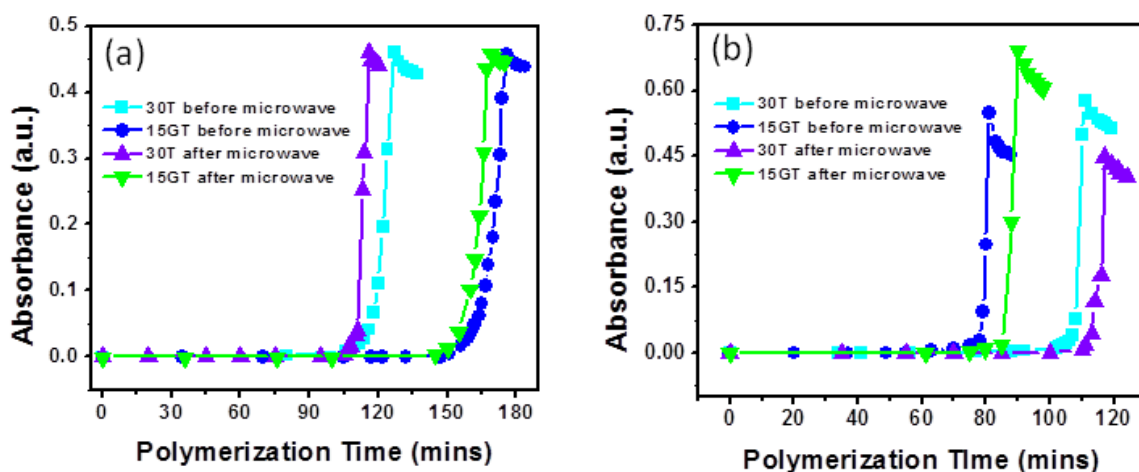


**Figure 2.9:** Kinetic profile of ABA polymerization in the presence of ssDNA(30T)-SWNT (cyan), ssDNA(15GT)-SWNT (blue), ssDNA(30T)-SWNT after microwave treatment (violet), and ssDNA(15GT)-SWNT after microwave treatment (green) in (a) acidic medium and (b) neutral medium.

The kinetic profile for ABA polymerization (acidic approach) in the presence of pre-microwaved and post-microwaved DNA-SWNT is shown in Figure 2.9a. Since the metallic SWNTs were all removed from the solution, the

ssDNA(15GT)-SWNT and ssDNA(30T)-SWNT should show the same kinetic profiles if the DNA sequence does not influence the polymerization rate. However in Figure 2.9a we see that after the removal of metallic SWNT by microwave irradiation the kinetic profiles for the two samples are not the same. Therefore, the DNA sequence plays a catalytic role.

Furthermore, if the metallic SWNTs do not influence the polymerization rate, then its kinetic profile should look exactly the same as before microwave treatment. However, it was found that the polymerization rate increases after metallic CNTs were removed from both ssDNA(15GT)-SWNT and ssDNA(30T)-SWNT. Although microwave treatment preferentially eliminates metallic CNTs, it is highly possible that very small concentrations exist in the sample and one may argue that the rate difference shown could be a result of its lower stability in acidic pH. However, the removal of metallic CNTs also shows a change in polymerization rate in the neutral approach (Figure 2.9b). If it is assumed that metallic CNTs display no catalytic effect, then its removal should not change the rate of polymerization. Based on this, it can be concluded that the metallic to semiconducting CNT ratio contributes to the catalytic effect observed.

The catalytic effect is possibly due to the different properties exhibited by metallic and semiconducting CNTs. Using UV-Vis-NIR spectroscopy, Zheng *et al.* [55] studied the electron transfer of small-molecule inorganic redox reagents with CNTs of different chiralities. It was found that the reduction potential of the CNTs increases with increasing band gap energies. Due to its larger band gap,

semiconducting CNTs is expected to have a higher reduction potential than metallic CNTs. This implies that during the polymerization process the metallic CNTs can donate its electrons more easily to the ABA monomers than semiconducting CNTs, increasing the electron density on the monomers and ultimately increasing the rate of polymer formation. Therefore samples with different metallic to semiconducting CNT ratios can yield different polymerization rates.

#### **2.2.4.1.3. Catalytic role of different sequence of DNA**

In Figure 2.9, the kinetic profiles show only a small change in the initiation time between the pre and post microwaved samples. This suggests that in addition to the catalytic effect shown by metallic CNTs, there may be other factors that contribute to the increase in polymerization rate. As mentioned earlier, one possible factor is the catalytic effect due to the different sequence of DNA used to disperse the CNTs.

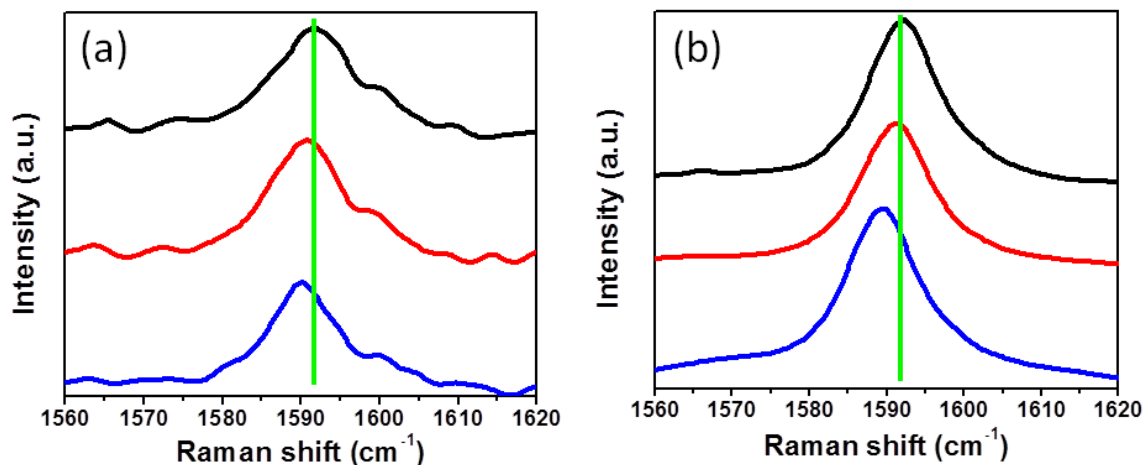


**Figure 2.10:** Raman spectrum of (a) ssDNA(30T)-SWNT and (b) ssDNA(15GT)-SWNT with different concentrations of ABA monomers: 0mM ABA (black), 3mM ABA (red), 5mM ABA (blue).

To determine if there is an electronic factor from the different sequences influencing the polymerization rate, Raman spectroscopy was used to study its electronic interaction with ABA monomers. It has been shown in literature that electron donating and electron withdrawing groups can be used to tailor the electronic structures of SWNTs [56]. Electron withdrawing groups are known to cause a downshift of the  $G^+$  band and electron donating groups causes an upshift. The Raman spectrum of ssDNA(30T)-SWNT (Figure 2.10a) and ssDNA(15GT)-SWNT (Figure 2.10b) at different concentrations of ABA monomers is shown. From both spectra a downshift of the  $G^+$  band is seen, indicating that ABA withdraws electrons from the CNTs, which is consistent with the data presented previously in Figure 2.2. As the concentration of ABA is increased, the downshift of the  $G^+$  band also increases. This suggest that the

larger the downshift, the larger the electron transfer ability. Based on the figures, it was determined that 5mM of ABA caused ssDNA(30T)-SWNT and ssDNA(15GT)-SWNT to downshift  $1.5\text{cm}^{-1}$  and  $2.7\text{cm}^{-1}$ , respectively. Therefore, ssDNA(15GT) tends to transfer electrons more efficiently than ssDNA(30T) and may be the reason for the difference in the polymerization rates for differently dispersed SWNTs.

#### **2.2.4.2. Catalytic role of SWNT and MWNT**

As mentioned before, MWNTs are made of concentric layers of SWNTs. Their shell coupling interactions are complex and not fully understood [30-32]. One possible reason for the faster polymerization rate obtained using MWNT is that MWNT may have a higher electron density due to its multiple SWNT layers. This enables MWNTs to donate electrons to the ABA monomers, making it easier to polymerize compared with SWNT.

#### **2.2.5. Quality of produced CNT-PABA composite**

In the previous section, it was found that the type of CNT used (MWNT or SWNT), the metallic to semiconducting SWNT ratio present, and the sequence of DNA used to disperse the CNT all contributed to the rate of ABA polymerization. Although this is important, it is equally vital to study the CNT-polymer composite formed. CNT-PABA composites are used in various applications and generally

properties such as high conductivity with long conjugated structures are desired. To characterize the different polymer composites formed in the previous section, UV-Vis and FTIR spectroscopy was used.

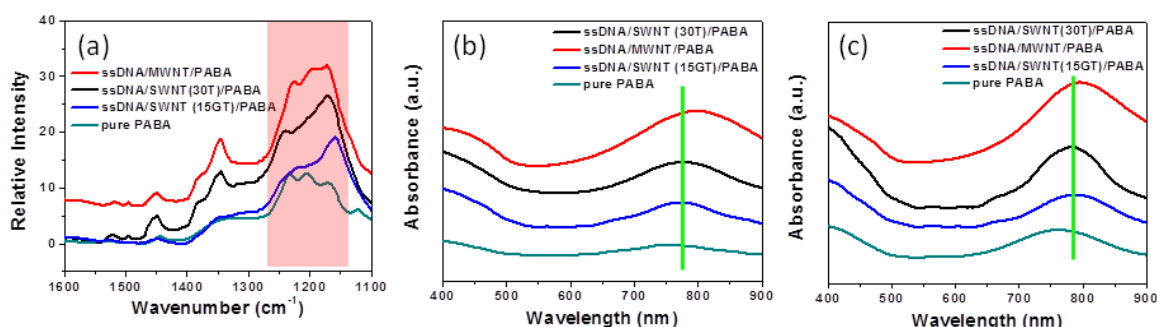


**Figure 2.11:** (a) FTIR spectrum showing the “electronic-like” band (shaded area) of various DNA-CNT/PABA in acidic medium. UV-Visible-NIR spectra of various in-situ polymerized DNA-CNT/PABA in (b) acidic medium and (c) neutral medium. The curves corresponds to: ssDNA-MWNT/PABA (red), ssDNA(30T)-SWNT/PABA (black), ssDNA-SWNT(15GT)/PABA (blue), and pure PABA (cyan).

The FTIR spectrum of ssDNA(30T)-SWNT/PABA, ssDNA(15GT)-SWNT/PABA, ssDNA-MWNT/PABA, and pure PABA are shown in Figure 2.11a. The most prominent band at  $\sim 1180\text{cm}^{-1}$  is known as the electronic-like band, which is a measure of the degree of delocalization of electrons along the polyaniline backbone and is correlated to the electrical conductivity of polyaniline [57]. The FTIR shows an increasing intensity as follows: pure PABA < ssDNA(15GT)-SWNT/PABA < ssDNA(30T)-SWNT/PABA < ssDNA-MWNT/PABA. This suggests that ABA polymerization in the presence of ssDNA/MWNT yields CNT-polymer composites with the longest conjugated

polymer lengths, and therefore the highest conductivities. This trend is similar to that in the UV-Vis spectrum (Figure 2.11b). After polymerization, pure PABA shows the shortest wavelength at 753nm and 763nm for both acidic and neutral polymerization approaches, respectively. ssDNA(15GT)/SWNT/PABA and ssDNA(30T)/SWNT/PABA showed approximately the same wavelengths for both acidic (~774nm) and neutral cases (~788nm). ssDNA/MWNT/PABA showed the highest wavelength at 790nm and 798nm for acidic and neutral approaches, respectively. The UV-Vis and FTIR data suggest that ABA polymerization in the presence of MWNT produces composites with the longest conjugation length and thus highest conductivity.

## 2.3 Conclusion

In summary, we carefully and systematically studied the “catalytic roles” of DNA dispersed carbon nanotubes for the polymerization of ABA. All DNA dispersed CNTs (MWNTs and SWNTs) dramatically increased the polymerization rate. Most importantly, the quality of the polymer produced in terms of conjugation length and therefore their conductivity was also largely improved. The MWNTs showed much higher catalytic effect compared to the SWNTs. The efficiency of SWNTs in speeding up the polymerization rate highly depends on two factors: 1) the metallic/semiconducting CNT ratio present in the SWNTs. 2) the sequence of DNA used to disperse the SWNTs. This work provides a deep fundamental understanding of the role of electronic structure



and surface chemistry of carbon nanotubes in polymerization reactions, providing guidance to more efficient fabrication of high quality conducting polymer composites for various practical applications.

## 2.4 Experimental

### 2.4.1. Reagents

3-Aminophenylboronic acid hemisulfate salt (ABA), potassium fluoride (KF), ammonium persulfate (APS), potassium phosphate monobasic, potassium phosphate dibasic trihydrate, sodium chloride, DNA (dsDNA) from salmon testes, and fructose were purchased from Aldrich and used as received without further purification. Sulfuric acid was purchased from Pharmco-Aaper. Single stranded DNA with sequence d(T)<sub>30</sub> (ssDNA(30T)) and sequence d(GT)<sub>15</sub> (ssDNA(15GT)) were purchased from Integrated DNA Technologies. Single walled carbon nanotubes (SWNT) were purchased from Carbon Nanotechnologies, Inc. Multi walled carbon nanotubes (MWNT) were purchased from Nanolab, Inc. All solutions were prepared using deionized water (18.2M $\Omega$ ) (Nanopore water, Barnstead).

### 2.4.2. Dispersion of CNTs into aqueous solution

CNTs were dispersed into deionized water using a method previously described by Zheng *et al* [24]. Briefly, a suspension of CNTs and DNA underwent high powered sonication using a Sonics Vibra-Cell VCX 130 in deionized water. The sonication process was performed in an ice-water bath to prevent local heating of the CNT which may cause unnecessary scission of CNT. After sonication, the

sample was centrifuged with a Beckman J2-21 centrifuge at 6000g to remove undispersed CNT. To remove free DNA, the solution was dialyzed with a Microcon YM-50 centrifugal filter unit (Millipore) for 2 hours. The resulting solution consists of highly dispersed and functionalized DNA-CNTs with a mass concentration of 200-500mg/L. The electronic structure of the dispersed DNA-CNTs was characterized by UV-Visible spectroscopy.

### 2.4.3. In-situ monitoring of ABA polymerization

For acidic polymerization, 5mM ABA monomers were mixed with 40mM KF and dissolved in 0.05M  $\text{H}_2\text{SO}_4$ . DNA dispersed CNT was then added to the mixture so that the concentration added was 70mg/L. The mixture was bubbled in nitrogen gas for 30 minutes prior to the start of the polymerization to remove dissolved oxygen. Afterwards, the polymerization was initiated by the addition of 0.2mM APS. The experiments were performed at 4°C and nitrogen gas was continuously bubbled during the polymerization process. The procedure for neutral polymerization is similar to that of acidic polymerization except for the following: it was performed at neutral pH (7.4) by using phosphate buffer saline (PBS) solution in the presence of fructose.

## 2.4.4. Characterization

### 2.4.4.1 Ultraviolet-Visible-Near Infrared Spectroscopy

Spectra were acquired with a Cary 500 UV-Vis-NIR spectrophotometer. The spectra were collected over the range of 200-1300 nm for the characterization of DNA dispersed CNTs and 200-1100 nm for the in-situ polymerization monitoring process. In preparing the samples for UV-Vis spectral analysis, 50  $\mu$ l of the solution were taken and dissolved in 3 mL of de-ionized water. Nitrogen purging was stopped between each measurement.

### 2.4.4.2 Raman Spectroscopy

Raman spectra were acquired using a Kaiser Optical Systems Raman Microprobe. The spectra were collected using a 785nm diode laser over the range of 700-4000 $\text{cm}^{-1}$ . For Raman spectra measurements, the DNA-CNT solution was diluted and drop-cast onto a slide.

### 2.4.4.3 Fourier Transform Infrared Spectroscopy

All FTIR spectra were obtained using a Spectrum Spotlight FTIR Imaging System with a spectral resolution of 4  $\text{cm}^{-1}$ . The spectra were collected over the range of 700-4000 $\text{cm}^{-1}$ . In preparing the sample for FTIR analysis, diluted samples of the polymer solutions were dried in vacuum on  $\text{CaF}_2$  windows.

## 2.5 References

1. Barrera, E.V., M.L. Shofner, and E.L. Corral, *Applications: Composites*, in *Carbon Nanotubes: Science and Applications*, M. Meyyappan, Editor. 2005, CRC Press.
2. Banerjee, S., T. Hemraj-Benny, and S.S. Wong, *Covalent Surface Chemistry of Single-Walled Carbon Nanotubes*. *Adv. Mater.*, 2005. **17**: p. 17-29.
3. Bhadra, S., et al., *Progress in preparation, processing and applications of polyaniline*. *Prog. Polym. Sci.*, 2009. **34**: p. 783-810.
4. Roncali, J., P. Leriche, and A. Cravino, *From One- to Three-Dimensional Organic Semiconductors: In Search of the Organic Silicon?* *Adv. Mater.*, 2007. **19**: p. 2045-2060.
5. Baughman, R.H. and L.W. Shacklette, *Conductivity as a function of conjugation length: Theory and experiment for conducting polymer complexes*. *Phys. Rev. B*, 1989. **39**: p. 5872-5886.
6. Martin, C.R., R. Parthasarathy, and V. Menon, *Template synthesis of electronically conductive polymers - A new route for achieving higher electronic conductivities*. *Synth. Met.*, 1993. **55**: p. 1165-1170.
7. Meng, H., D.F. Perepichka, and F. Wudl, *Facile Solid-State Synthesis of Highly Conducting Poly(ethylenedioxythiophene)*. *Angew. Chem. Int. Ed.*, 2003. **42**: p. 658-661.
8. Cao, Y., et al., *Influence of chemical polymerization conditions on the properties of polyaniline*. *Polymer*, 1988. **30**: p. 2305-2311.
9. Kuramoto, N. and A. Tomita, *Aqueous polyaniline suspensions: chemical oxidative polymerization of dodecylbenzene-sulfonic acid aniline salt*. *Polymer*, 1997. **38**: p. 3055-3058.
10. Huang, W.-S., B.D. Humphrey, and A.G. Macdiarmid, *Polyaniline, a Novel Conducting Polymer*. *J. Chem. Soc., Faraday Trans.*, 1986. **82**: p. 2385-2400.
11. Cao, Y. and P. Smith, *Liquid-crystalline solutions of electrically conducting polyaniline*. *Polymer*, 1993. **34**: p. 3139-3143.
12. Adams, P.N., P.J. Laughlin, and A.P. Monkman, *Low temperature synthesis of high molecular weight polyaniline*. *Polymer*, 1996. **37**: p. 3411-3417.
13. Cao, Y., P. Smith, and A.J. Heeger, *Counter-ion induced processibility of conducting polyaniline and of conducting polyblends of polyaniline in bulk polymers*. *Synth. Met.*, 1992. **48**: p. 91-97.
14. Adams, P.N., D.C. Apperley, and A.P. Monkman, *A comparison of the molecular weights of polyaniline samples obtained from gel permeation chromatography and solid state  $^{15}\text{N}$  NMR spectroscopy*. *Polymer*, 1993. **34**: p. 328-332.

15. Ajayan, P.M. and O.Z. Zhou, *Carbon Nanotubes: Synthesis, Structure, Properties and Applications*, ed. M.S. Dresselhaus, G. Dresselhaus, and P. Avouris. 2001: Springer.
16. Dalton, A.B., et al., *Super-tough carbon-nanotube fibres*. *Nature*, 2003. **423**: p. 703.
17. Sainz, R., et al., *A soluble and highly functional polyaniline–carbon nanotube composite*. *Nanotechnol.*, 2005. **16**: p. S150-S154.
18. Ma, Y., et al., *The Electronic Role of DNA-Functionalized Carbon Nanotubes: Efficacy for in Situ Polymerization of Conducting Polymer Nanocomposites*. *J. Am. Chem. Soc.*, 2008. **130**: p. 7921-7928.
19. Tzou, K. and R.V. Gregory, *Kinetic Study of the Chemical Polymerization of Aniline in Aqueous Solutions*. *Synth. Met.*, 1992. **47**: p. 267-277.
20. Cheung, W., et al., *Fabrication of high performance conducting polymer nanocomposites for biosensors and flexible electronics: summary of the multiple roles of DNA dispersed and functionalized single walled carbon nanotubes*. *J. Mater. Chem.*, 2009. **19**: p. 6465-6480.
21. Long, Y., et al., *Synthesis and electrical properties of carbon nanotube polyaniline composites*. *Appl. Phys. Lett.*, 2004. **85**: p. 1796-1798.
22. Ma, Y., et al., *In Situ Fabrication of A Water-Soluble, Self-Doped Polyaniline Nanocomposite: The Unique Role of DNA Functionalized Single-Walled Carbon Nanotubes*. *J. Am. Chem. Soc.*, 2006. **128**: p. 12064-12065.
23. Ma, Y., et al., *Improved Conductivity of Carbon Nanotube Networks by In Situ Polymerization of a Thin Skin of Conducting Polymer*. *ACS Nano*, 2008. **2**: p. 1197-1204.
24. Zheng, M., et al., *DNA-assisted dispersion and separation of carbon nanotubes*. *Nat. Mater.*, 2003. **2**: p. 338-342.
25. Hamada, N., S. Sawada, and A. Oshiyama, *New one-dimensional conductors: graphitic microtubules*. *Phys. Rev. Lett.*, 1992. **68**: p. 1579-1581.
26. Saito, R., et al., *Electronic structure of chiral graphene tubules*. *Appl. Phys. Lett.*, 1992. **60**: p. 2204-2206.
27. O' Connell, M.J., et al., *Band Gap Fluorescence from Individual Single-Walled Carbon Nanotubes*. *Science*, 2002. **297**: p. 593-596.
28. Nakashima, N., et al., *DNA dissolves Single-walled Carbon Nanotubes in water*. *Chem. Lett.*, 2003. **32**: p. 456-457.
29. Yang, Z., et al., *Noncovalent Wrapped Sidewall Functionalization of Multiwall Carbon Nanotubes with Polyimide*. *Polymer Composites*, 2007. **38**: p. 36-41.
30. Baughman, R.H., et al., *Carbon Nanotube Actuators*. *Science*, 1999. **284**: p. 1340-1347.
31. Hafner, J.H., C.L. Cheung, and C.M. Lieber, *Growth of nanotubes for probe microscopy tips*. *Nature*, 1999. **398**: p. 761-762.
32. Ye, Y., et al., *Hydrogen adsorption and cohesive energy of single-walled carbon nanotubes* *Appl. Phys. Lett.*, 1999. **74**: p. 2307-2309.

33. O' Connell, M.J., E.E. Eibergen, and S.K. Doorn, *Chiral selectivity in the charge-transfer bleaching of single-walled carbon-nanotube spectra*. Nat. Mater., 2005. **4**: p. 412 - 418.
34. Dukovix, G., et al., *Reversible Surface Oxidation and Efficient Luminescence Quenching in Semiconductor Single-Wall Carbon Nanotubes*. J. Am. Chem. Soc., 2004. **126**: p. 15269-15276.
35. Strano, M.S., et al., *Reversible, Band-Gap-Selective Protonation of Single-Walled Carbon Nanotubes in Solution*. J. Phys. Chem. B, 2003. **107**: p. 6979-6985.
36. Wei, Y., et al., *A study of the mechanism of aniline polymerization*. J. Polym. Sci. A, 2003. **27**: p. 2385-2396.
37. Sivakumar, C., T. Vasudevan, and A. Gopalan, *Chemical Oxidative Polymerization and in situ Spectrochemical Studies of a Sulfonated Aniline Derivative by UV-Visible Spectroscopy*. Ind. Eng. Chem., 2001. **40**: p. 40-51.
38. Freund, M.S. and B.A. Deore, *Self-Doped Conducting Polymers*. 2007: John Wiley & Sons, Ltd.
39. Gajendran, P. and R. Saraswathi, *Polyaniline-carbon nanotube composites*. Pure Appl. Chem., 2008. **80**: p. 2377-2395.
40. Deore, B.A., S. Hachey, and M.S. Freund, *Electroactivity of Electrochemically Synthesized Poly(Aniline Boronic Acid) as a Function of pH: Role of Self-Doping*. Chem. Mater., 2004. **16**: p. 1427-1432.
41. Stilwell, D.E. and S.-M. Park, *Electrochemistry of Conductive Polymers*. J. Electrochem. Soc., 1989. **136**: p. 427-433.
42. Fu, Y. and R.L. Elsenbaumer, *Thermochemistry and Kinetics of Chemical Polymerization of Aniline Determined by Solution Calorimetry*. Chem. Mater., 1994. **6**: p. 671-677.
43. Sapurina, I. and J. Stejskal, *The mechanism of the oxidative polymerization of aniline and the formation of supramolecular polyaniline structures*. Polym. Int., 2008. **57**: p. 1295-1325.
44. Arnold, M.S., et al., *Sorting carbon nanotubes by electronic structure using density differentiation*. Nat. Nanotechnol., 2006. **1**: p. 17-18.
45. Zheng, M., et al., *Structure-Based Carbon Nanotube Sorting by Sequence-Dependent DNA Assembly*. Science, 2003. **302**: p. 1545-1548.
46. Dresselhaus, M.S., et al., *Raman spectroscopy of carbon nanotubes*. Physics Reports, 2005. **409**: p. 47-99.
47. Pang, D.W., et al., *Electrochemical oxidation of DNA at a gold microelectrode*. Electroanalysis, 1995. **7**: p. 774-777.
48. Strano, M.S., et al., *Electronic Structure Control of Single-Walled Carbon Nanotube Functionalization*. Science, 2003. **301**: p. 1519-1522.
49. Shim, H.C., et al., *Preferential elimination of metallic single-walled carbon nanotubes using microwave irradiation*. Nanotechnol., 2009. **20**.
50. Thostenson, E.T. and T.-W. Chou, *Microwave processing: fundamentals and applications*. Composites: Part A, 1999. **30**: p. 1055-1071.

51. Jorio, A., G. Dresselhaus, and M.S. Dresselhaus, *Carbon Nanotubes: Advanced Topics in the Synthesis, Structure, Properties and Applications*. 2008: Springer.
52. Nair, N., et al., *Estimation of the (n,m) Concentration Distribution of Single-Walled Carbon Nanotubes from Photoabsorption Spectra*. *Anal. Chem.*, 2006. **78**: p. 7689-7696.
53. Priya, B.R. and H.J. Bryne, *Quantitative Analyses of Microwave-Treated HiPco Carbon Nanotubes Using Absorption and Raman Spectroscopy*. *J. Phys. Chem. C*, 2009. **113**: p. 7134-7138.
54. Jorio, A., et al., *G-band resonant Raman study of 62 isolated single-wall carbon nanotubes*. *Phys. Rev. B*, 2002. **65**.
55. Zheng, M. and B.A. Diner, *Solution Redox Chemistry of Carbon Nanotubes*. *J. Am. Chem. Soc.*, 2004. **126**: p. 15490-15494.
56. Shin, H.-J., et al., *Tailoring Electronic Structures of Carbon Nanotubes by Solvent with Electron-Donating and -Withdrawing Groups*. *J. Am. Chem. Soc.*, 2008. **130**: p. 2062-2066.
57. Salaneck, W.R., et al., *Physical Characterization of Some Polyaniline, (øN)x*. *Mol. Liq. Cryst.*, 1985. **121**: p. 191-194.



## **Chapter 3**

# **DNA Functionalized Carbon Nanotubes as Active Stabilizers: Enhanced Stability of Conducting Polymer Composites**

### **3.1 Introduction**

Conducting polymers have been studied for decades and their degradation and stability is of primary interest due to their potential applications in organic solar cells, biosensors, chemical sensors, and light emitting diodes [1]. Polymer degradation is believed to occur as soon as the polymer is synthesized and continues to degrade during its storage and use. The degradation processes are normally accompanied by changes in their chemical and physical properties which eventually results in complete deterioration of the polymer [2-3]. These property changes can be induced by heat, oxygen, radiation, mechanical stress, water, and many other influences [2-5].

As conducting polymer properties are being exploited for various applications, considerable attention has been focused on understanding the degradation mechanism and discovering methods to inhibit or mitigate its effects. The main degradation processes that occur during outdoor exposure is photodegradation (photolysis, photo-oxidation) and hydrolysis, resulting in chain scission, crosslinking, and oxidation of the polymer chain [2-4]. This is especially

true for organic materials such as conducting polymers because ultraviolet (UV) radiation has enough energy to directly break certain bonds and initiate further degradation through hydrolytic and oxidative processes [3].

Various methods have been proposed to inhibit or retard the degradation process. Four “polymer stabilizers” that are used to accomplish this are UV absorbers, UV quenchers, hydrogen donating antioxidants, and hindered amine light stabilizers (HALS). The role of UV absorbers is essentially absorbing the UV light radiation and dissipating it as heat, thereby reducing degradation of the polymer chain. UV absorbers normally have high absorption coefficients and are highly stable, which can prevent secondary reactions from occurring [6]. Two of the most used UV absorbers are hydroxybenzophenones and hydroxyphenylbenzotriazoles [7]. One of the biggest disadvantage of using UV absorbers is that a thick layer is needed to efficiently stabilize the polymer from degradation [6], which is unattractive in certain applications.

UV quenchers work in a similar manner to UV absorbers but instead of absorbing the UV light, they absorb energy. Energy that is gained by the polymer from UV light absorption is transferred to the UV quencher to prevent the polymer from degrading. This energy is dissipated as heat or photoluminescence [6]. UV quenchers are normally not used because they contain heavy metals such as Nickel and are not as efficient as other methods [6-7].

The third polymer stabilizer is the hydrogen donating antioxidants such as hindered phenols and secondary aromatic amines which mitigates the effects of degradation by transferring a proton to free radical species, preventing it from

reacting with the polymer backbone [5]. During the proton transfer, a new radical is formed. The new radical generated is always less reactive and does not react with the polymer chain.

HALS is another class of polymer stabilizer that is commonly used today and inhibits the degradation process through the formation of nitroxyl radicals [8]. The nitroxyl radical acts as a “radical trap (scavenger)”, where it binds with a free radical temporarily to prevent it from reacting with the polymer chain. When the complex encounters another free radical, the nitroxyl radical is regenerated and a non-radical product is formed (both radicals combine to form non-radical product). Most of these stabilizers are used simultaneously to achieve maximum stabilizing effect.

Although there are currently numerous polymer stabilizers available, there is still much attention focused on discovering new stabilizers and understanding their stabilizing mechanism. Due to its similarity to carbon black and fullerenes, which have both been shown to possess UV absorbing and radical scavenging behavior [9-10], carbon nanotubes have also been studied for these stabilizing effects.

The stabilization properties of carbon nanotubes have been well studied in literature. Using electron spin resonance spectroscopy (ESR), Fenoglio *et al.* [11] have recently shown that hydroxyl radicals formed by the Fenton reaction and also by UV radiation can be largely reduced in the presence of MWNTs. The radical scavenging ability of SWNTs was also studied by density functional theory calculations. Using different types of radicals, Galano [12] showed that the

reaction of SWNTs with the radicals studied were exothermic and exergonic. Furthermore, reaction with further radicals was energetically favored, suggesting the scavenging capability of SWNTs. Although the mechanism is not fully understood, it is believed that the radical scavenging ability of carbon nanotubes may be due to their high electron affinity.

Although there are many literature about using CNTs as stabilizers [10-12], their stabilizing effect on conducting polymers are not well documented. **In this chapter of the thesis, we will attempt to explore the effects of CNTs on stabilizing conducting polymers under UV light environment.** The conducting polymer used is poly(aniline boronic acid) (PABA) due to their interesting properties and potential uses in various applications. The use of CNTs as the active stabilizer for conducting polymers is extremely attractive because it provides several benefits. Not only does it help stabilize the polymer but it also improves its properties through synergistic effects.

## 3.2 Results and Discussion

### 3.2.1. Stabilization of PABA monitored using Spectroscopic Methods

CNT/PABA solutions were prepared and irradiated with UV light to increase the rate of degradation [13]. The samples were irradiated with three different wavelengths and the absorption spectra were monitored (Figure 3.1). As mentioned in the previous chapter, PABA have three distinct absorption bands at ~260nm due to the  $\pi - \pi^*$  transition of aniline, ~390nm due to the polaron transition or to quinone diimine structure of low molecular weight oligomers, and ~700-800nm due to the bipolaron transition. Therefore the UV radiation wavelengths were chosen accordingly. As shown in Figure 3.1, the polymer absorption peak at ~800nm does not show significant change after 5hr UV radiation for samples irradiated with 254nm light (1a) and 800nm light (1c). In contrast, there is a noticeable change in the absorption peak for the sample irradiated with 365nm light (1b). The blue shift and decrease in intensity of the absorption peak seen can be explained by a decrease in both the polymer conjugation length and polymer concentration. The conjugation length of a conducting polymer is normally associated with the conductivity of the polymer. It is known that as polyaniline degrades, its conductivity also decreases [14-15]. Therefore, the decrease in conjugation length and concentration shown suggests a decrease in conductivity and can be used to monitor the degradation of PABA.

Due to the noticeable change seen using 365nm light, all samples from here on were irradiated with this wavelength.

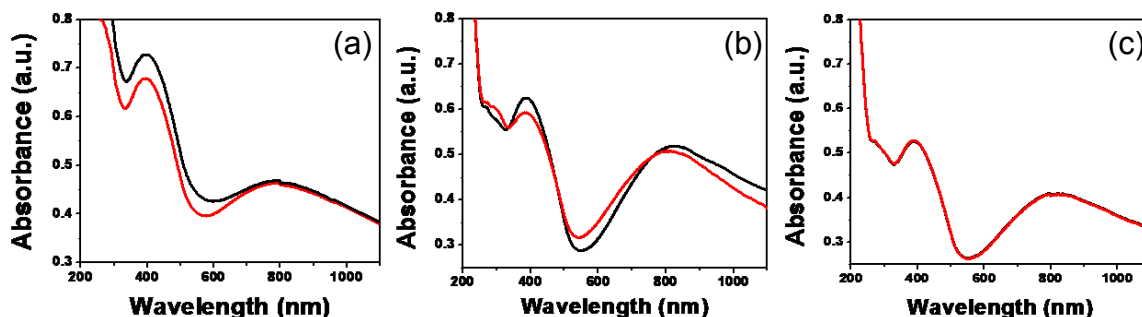


**Figure 3.1:** UV-Vis spectra of ssDNA/SWNT/PABA irradiated using (a) 254nm light, (b) 365nm light, and (c) 800nm light at different irradiation times: (black curve) 0hr and (red) 5hrs.

To determine if CNTs can help stabilize PABA, three PABA solutions were prepared. The three solutions are as follows: pure PABA (no CNTs are present), 0.2% ssDNA/SWNT/PABA (CNT used is 0.2% weight of ABA) and 1% ssDNA/SWNT/PABA (CNT used is 1% weight of ABA). The three polymer solutions were subjected to UV irradiation and the UV-Visible spectra were obtained at different time intervals (Figure 3.2). From the figure, it can be seen that UV irradiation induces significant changes in the UV-Vis spectra and there are three distinct features of interest. First, there is an increase in absorption at ~266nm. This may be due to oxidation of the PABA backbone, resulting in an increase in concentration of ABA monomers and PABA degraded products. Studies have shown that degradation of PABA can yield degraded products such as hydroquinone, p-benzoquinone, and p-aminophenol [16-17]. The second feature of interest is the increase of absorption at ~550nm. The absorption band

at ~550nm is attributed to the non-conductive pernigraniline oxidation state of PABA and to degraded products such as quinoneimines [18-20]. Furthermore, as we have seen before, the absorption band at ~800nm experiences a decrease in intensity and blue shift of the wavelength. This band is due to bipolaron transitions and is normally attributed to the emeraldine oxidation state of PABA [18-19].

Based on the UV Visible data it appears that UV irradiation of PABA samples causes two main degradation pathways: chain scission and oxidation of PABA. Chain scission results in the formation of degraded products and therefore can lower the absorption intensity of the emeraldine peak and increase the absorption intensity at ~260nm and ~550nm. Oxidation of PABA causes the polymer to convert from the emeraldine oxidation state to the pernigraniline oxidation state. This can explain the decrease in absorption of the emeraldine peak and the increase of absorption of the pernigraniline peak at ~550nm. It is believed that the combination of both degradation processes may have caused the changes seen in the UV spectra upon irradiation.

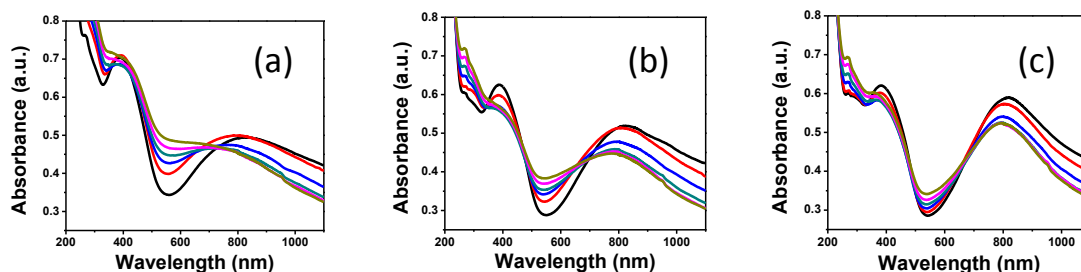


**Figure 3.2:** UV spectra of (a) pure PABA, (b) 0.2% ssDNA/SWNT/PABA, (c) 1% ssDNA/SWNT/PABA after irradiation for (black) 0hrs, (red) 5hrs, (blue) 20hrs, (green) 35hrs, (magenta) 50hrs, (olive) 65hrs. For all three spectra, UV irradiation causes the intensity of the emeraldine peak at  $\sim 800\text{nm}$  to decrease and to blue shift.

To get a clear understanding of the degradation and stabilization mechanisms, the wavelength shift and intensity decrease of the emeraldine absorption band was studied more in detail. The normalized changes in wavelengths and in intensities were plotted as a function of irradiation time (Figure 3.3). From Figure 3.3a, it can clearly be seen that different concentrations of SWNTs have a large impact on the wavelength shifts of PABA. Pure PABA shows the largest wavelength decrease ( $\sim 20\%$ ) after 65hrs of UV irradiation. It is significantly larger than 0.2% ssDNA/SWNT/PABA ( $\sim 5.5\%$ ) and 1% ssDNA/SWNT/PABA ( $\sim 2.9\%$ ). Furthermore, as higher concentrations of SWNT are used to form the SWNT/PABA, the less the wavelength shifts. Since the wavelength decreases more in PABA in the absence of SWNTs, this suggests that SWNTs participates in the stabilization of PABA. Furthermore, this stabilizing effect can also be seen by analyzing the intensity decrease (Figure 3.3b). Similar to the wavelength shift analysis seen in Figure 3.3a, pure PABA shows the



largest peak intensity decrease after 65hrs irradiation (18.4%), followed by 0.2% ssDNA/SWNT/PABA (13.3%), and 1% ssDNA/SWNT/PABA (10.4%).

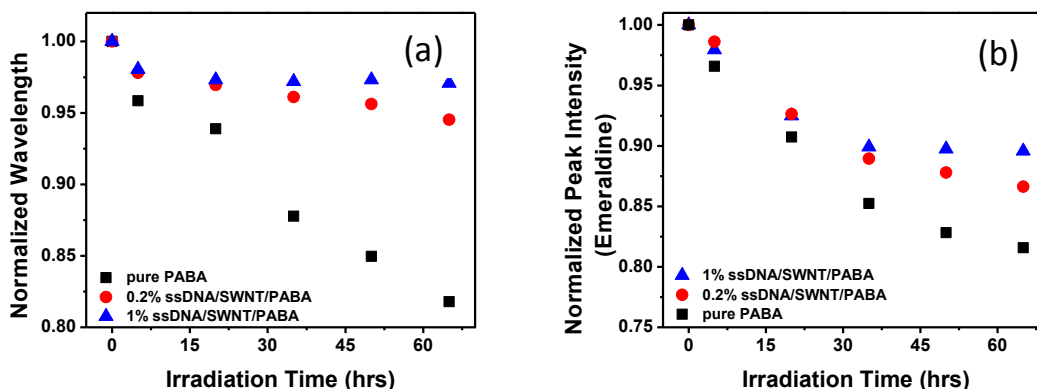


**Figure 3.3:** (a) Normalized wavelength changes and (b) normalized intensity changes for (black) pure PABA, (red) 0.2% ssDNA/SWNT/PABA, and (blue) 1% ssDNA/SWNT/PABA.

To further validate this phenomenon seen, the emission peak at 450nm was monitored using fluorescence spectroscopy (excited at 390nm). As mentioned previously, absorption peak seen at 390nm is due to polaron transition of the polymer or to low molecular weight oligomers. The polymer itself, however, does not show strong fluorescence due to quenching of the polymer signal due to oxidation of its chain and polaron formation [21]. Therefore the fluorescence signal is contributed from oligomers and can be used to monitor the degradation process. As shown in Figure 3.4, the fluorescence decreases as irradiation time increases. The trend shown here is similar to that seen using UV-Vis

spectroscopy. One possible explanation for the decrease in fluorescence may be the degradation of the oligomers to monomers.

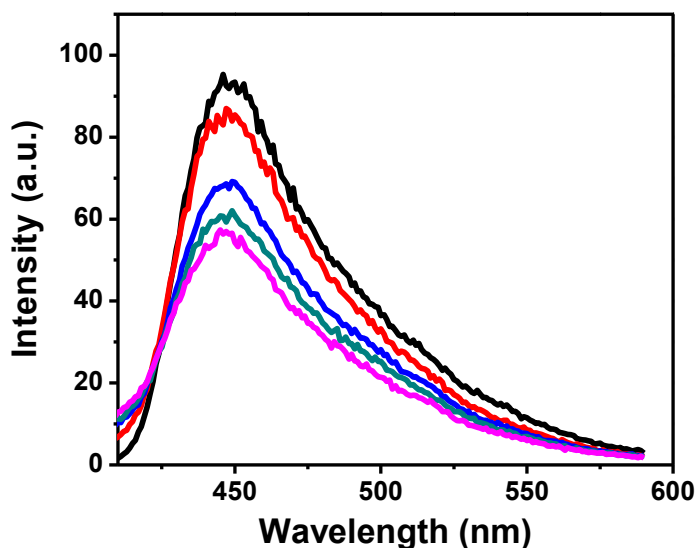


**Figure 3.4:** Fluorescence spectrum of pure PABA at different irradiation times (black) 0hrs, (red) 5hrs, (blue) 35hrs, (olive) 50hrs, and (magenta) 65hrs.

### 3.2.2. Stabilization of PABA monitored using Conductance Measurements

Since degradation causes the conjugation length of PABA to decrease, this would lead to the decrease in conductance as well. Therefore the degradation of PABA and its stabilization by SWNTs can also be monitored by changes in its conductance. The conductance of both the PABA polymer alone and the PABA/SWNT composites exhibit percolation behavior [22], showing sharp increases by several orders of magnitude when the concentration of the

conductive species in the formed films reaches its respected percolation threshold. We first found their respective percolation thresholds by adding PABA polymer or the PABA/SWNT composites onto Si chips with pre-patterned gold electrode pairs (1.5  $\mu\text{m}$  apart) using a layer by layer approach. The conductance was monitored by two probe conductance measurement. After all samples reached percolation, they were irradiated with UV light in the same manner as before and the conductance was measured at different irradiation times. The purpose of allowing the samples to percolate prior to irradiation is to compare the percentage decrease in conductance once the maximum number of conducting networks has been formed for each of the samples.

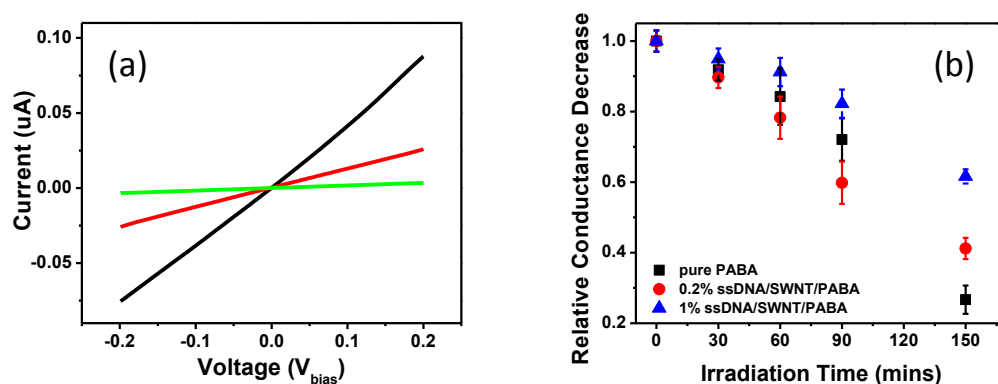


**Figure 3.5:** (a) I-V curve of pure PABA irradiated for 0 (black), 60 (red), and 150 mins (green). (b) Normalized relative conductance decrease for pure PABA (black), 0.2% ssDNA/SWNT/PABA (red), 1% ssDNA/SWNT/PABA (blue).

Figure 3.5a shows a typical I-V curve obtained for pure PABA after different irradiation times. As expected, the degradation of PABA causes a

decrease in conductance. It is known that SWNT/PABA composites show a much higher conductance than pristine PABA [23-24]. To compare the effect of degradation of the PABA samples, the conductance were normalized and shown in Figure 3.5b. Pure PABA showed the largest relative decrease in conductance (73.31%) compared to 0.2% ssDNA/SWNT/PABA (58.79%) and 1% ssDNA/SWNT/PABA (38.40%) after UV light irradiation. These results are consistent with the UV-Vis measurements and reveal that the amount of ssDNA/SWNT added to the polymerization process affects the stability of the formed polymer nanocomposite.

### **3.2.3. Stabilization of PABA monitored using FTIR spectroscopy**

In order to understand this stabilizing phenomenon further, we used FTIR spectroscopy to study the changes in molecular structure of the formed polymers before and after UV irradiation. Figure 3.6a shows the FTIR spectra of pure PABA at different UV irradiation times. From the figure, there are three absorption bands of interest. The strong absorption band at  $1100\text{ cm}^{-1}$  can be attributed to the “electronic-like band” and is a measure of the degree of delocalization of electrons, and thus its conductivity [25-26]. The absorption band at  $1596\text{ cm}^{-1}$  can be attributed to the C=N stretching in the quinoid type ring [27-

28] and the absorption band at  $1440\text{ cm}^{-1}$  is from mixed C-N, C-C stretching, C-H, and N-H bending vibrations of the benzenoid ring [28].

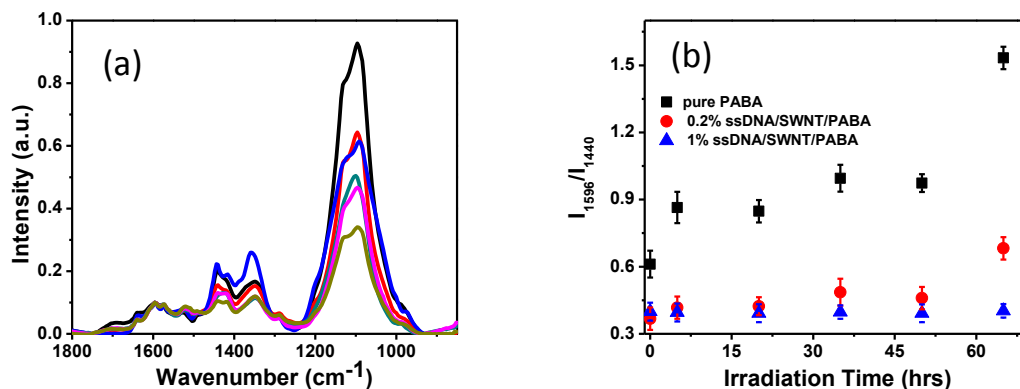


**Figure 3.6:** (a) FTIR spectra of pure PABA after exposure to UV light irradiation for 0 (black), 5 (red), 20 (blue), 35 (green), 50 (magenta), and 65 hours (olive). (b) Quinoid to benzenoid ratio ( $I_{1596}/I_{1440}$ ) at different irradiation times for pure PABA (black), 0.2% ssDNA/SWNT/PABA (red), 1% ssDNA/SWNT/PABA (blue).

A general relative decrease in the “electronic-like” peak is seen, indicating that the conductivity of the polymers decreases with increasing UV irradiation time. The relative intensity decrease of the “electronic-like band” for the three polymers was calculated. After 65 hours of UV light irradiation, pure PABA showed the greatest relative decrease in intensity (63.2%) compared to 0.2% ssDNA/SWNT/PABA (33.6%) and 1% ssDNA/SWNT/PABA (17.0%). This reveals that pure PABA experiences the greatest conductivity loss compared to the composites containing SWNT. Furthermore, as the concentration of SWNT increases, the polymer produced has greater stability.

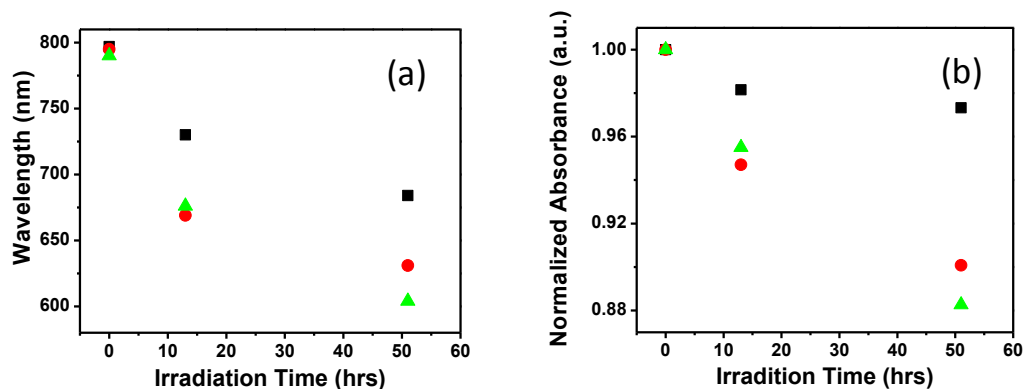
Furthermore, the absorption bands corresponding to the quinoid ring located at  $1596\text{ cm}^{-1}$  and the benzenoid ring at  $1440\text{ cm}^{-1}$  can be expressed as an intensity ratio ( $I_{1596}/I_{1440}$ ) and used to study the degradation process. This quinoid to benzenoid ratio can provide information on the degree of oxidation of the polymer. As shown in the previous chapters, PABA has many different oxidation states and only the emeraldine state is conductive. From the UV-Vis data shown in Figure 3.2, UV irradiation can cause the oxidation of PABA. Therefore it is possible that the conductive half-oxidized emeraldine state is converted to the non-conductive fully oxidized pernigraniline state. During this process, the benzenoid units of emeraldine are oxidized to quinoid units. By monitoring the change in  $I_{1596}/I_{1440}$  ratio, the rate of emeraldine conversion to pernigraniline can be studied.

Figure 3.6b shows the quinoid to benzenoid intensity ratio of pure PABA, 0.2% ssDNA/SWNT/PABA, and 1% ssDNA/SWNT/PABA at different irradiation times. 1% ssDNA/SWNT/PABA showed almost no change ( $\sim 0.9\%$  increase) in the quinoid to benzenoid ratio, indicating that its molecular structure is relatively unaffected by UV irradiation even after 65 hours of exposure. The quinoid to benzenoid ratio, however, increased 1.9 times for 0.2% ssDNA/SWNT/PABA and over 2.5 times for pure PABA. This shows that as higher concentrations of ssDNA/SWNT are used to form the polymer composite, the amount of quinoid units present in the polymer chain is lower under UV irradiation and thus retarding the degradation process.

### **3.2.4. Role of ssDNA/SWNT in stabilization of PABA**

#### **3.2.4.1. UV absorber**

CNTs are known to absorb light across a wide spectral range [29], making them extremely attractive as UV absorbers. To determine the UV absorbing effect of CNTs on PABA, a postmixture approach in preparing the composites were used. In the postmixture approach, pure PABA was first prepared and then mixed with 1% ssDNA/SWNT. The three samples, pure PABA, postmixture, and 1% ssDNA/SWNT/PABA were irradiated and compared (Figure 3.7). As expected, 1% ssDNA/SWNT/PABA shows a much lower blue shift in wavelength and lower absorption decrease than pure PABA. The composite prepared by postmixture shows less blue shift (14.2%) than the pure PABA (23.5%), but more blue shift (20.6%) than the in-situ prepared composite with the same amount of ssDNA/SWNTs. The absorption intensity for the postmixture also decreases more than that of in situ prepared composite. This result shows that the UV absorbing ability of SWNTs plays a very important role in the stabilization of PABA. From Figure 3.7, we can conclude that PABA prepared by the in-situ approach degrades slower than PABA prepared by the postmixture approach. This suggests that SWNTs may be able to stabilize PABA by a different mechanism.



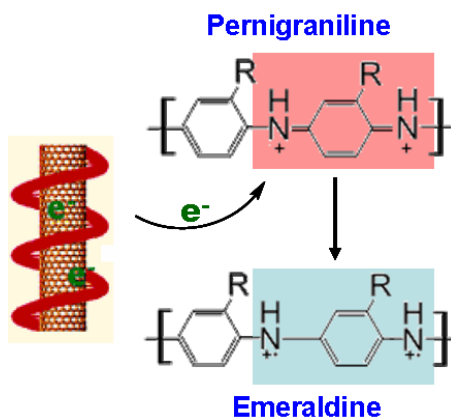
**Figure 3.7:** (a) Wavelength decrease and (b) absorption decrease of 1% ssDNA-SWNT/PABA (black), postmixture composite (red), and pure PABA (green) after different irradiation times

### 3.2.4.2. Proposed stabilization mechanism

The degradation of polyaniline has been well studied in literature and mechanisms involving photolysis, hydrolysis, oxidation, and crosslinking have all been proposed [13, 20, 30-31]. Polymer degradation is a complex process and it may involve several or all of the mechanisms listed above. Based on the data presented, degradation of PABA by oxidation will be considered to explain the stabilizing effects of SWNTs on in-situ prepared PABA composites. We hypothesize that this stabilizing effect is due to the reductive ability of ssDNA/SWNTs, which can reduce the nonconductive pernigraniline state to the stable and highly conductive emeraldine state (Scheme 3.1) and making the polymer more stable and less susceptible to further degradation such as hydrolysis which will lead to chain scission. It is shown in literature that the



pernigraniline state is unstable and degrades faster than the emeraldine state[13]. When PABA interacts with UV light, it loses electrons and is oxidized from the emeraldine state to the pernigraniline state. During the process, the electrons are possibly gained by the superoxides formed from oxygen in the environment [32]. The oxidized PABA is then reduced by the ssDNA/SWNTs back to the emeraldine state. Therefore, the molecular structure and thus the conductivity of the polymer are largely preserved. As the concentration of SWNT is increased, this stabilizing effect is more prominent, as supported by the conductance, UV-Vis, and FTIR data. In this process, the SWNTs itself are oxidized. Reduction of the oxidized SWNTs by water may occur and would complete the cycle [33-34].



**Scheme 3.1:** Proposed stabilization mechanism of ssDNA/SWNT during the in-situ polymerization process.

The stabilization mechanism proposed here would require electron transfer between the carbon nanotubes and the conducting polymer. Electron rich carbon nanotubes would facilitate this stabilization effect, while electron deficient carbon nanotubes would speed up the degradation process. However, reports have shown that electron deficient carbon nanotubes are good electron acceptors, showing strong radical scavenging ability, similar to fullerenes [10]. Therefore it is expected to show strong stabilization effect toward PABA degradation. To further test these hypotheses, we dispersed SWNTs by microwave irradiation. This process partially oxidizes the surface of the SWNT and simultaneously functionalizes the carbon nanotubes with some oxygen containing groups. Due to the partially oxidized surface, the microwave dispersed SWNTs (MD-SWNT) are poor electron donors compared to ssDNA/SWNTs. MD-SWNT/PABA composite were irradiated and the results are shown in Figure 3.8. In Figure 3.8a, it can clearly be seen that MD-SWNT/PABA experiences the largest intensity decrease compared with all the other PABA composites. This suggests that it degrades the fastest and provides no stabilization effect. In addition, it appears that MD-SWNT/PABA degrades faster than the pure PABA. More interestingly, we found that MD-SWNT does not cause significant blue shift of the emeraldine absorption band (Figure 3.7b), which is very different from what was seen during the degradation of pure PABA. Although at this point further studies are necessary for a complete understanding why the MD-SWNTs did not provide stabilization effects, it is evident that electronic structures of the MD-SWNT and the surface

functional groups on the MD-SWNT play a role in the observed increasing degradation rate.

Taking a step further, we prepared ssDNA/SWNT/PABA by polymerizing a monolayer of PABA on the ssDNA/SWNT surface. It has been shown that the “thin skin” approach can improve conductivity dramatically compared with ssDNA/SWNT itself [35]. The purpose of this is to study the stability of the “thin skin” ssDNA/SWNT/PABA which can be used as thin films for various electronic applications. The results are shown in Figure 3.8. Both figures clearly show that ssDNA/SWNT effectively stabilizes the thin layer of PABA making it highly attractive for electronic applications.

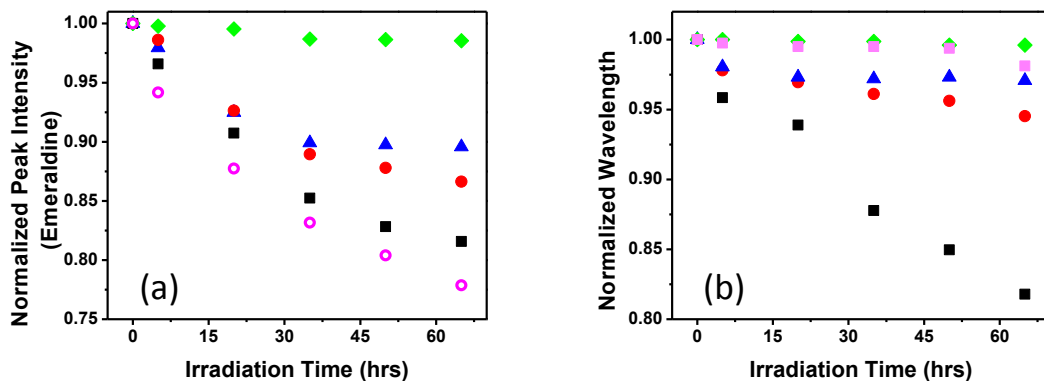


**Figure 3.8:** (a) Normalized intensity changes and (b) normalized wavelength changes for (magenta) MD-SWNT/PABA, (black) pure PABA, (red) 0.2% ssDNA/SWNT/PABA, (blue) 1% ssDNA/SWNT/PABA, and (green) “thin skin” ssDNA/SWNT/PABA.

### 3.3 Conclusion

In summary, not only was the electrical performance of the conducting polymer improved by *in-situ* polymerization of 3-aminophenylboronic acid (ABA) monomers in the presence of single-stranded DNA dispersed- and functionalized- single-walled carbon nanotubes (SWNTs), the composite also showed enhanced stabilization under UV irradiation. A new stabilization mechanism against UV irradiation was proposed based on the reductive capability of the carbon nanotubes functionalized with DNA. The enhanced stability would greatly help develop organic photonic systems as well as other electronic devices with longer life spans and thus commercial value.

## 3.4 Experimental

### 3.4.1. Reagents

3-Aminophenylboronic acid hemisulfate salt (ABA), potassium fluoride (KF), and ammonium persulfate (APS) were purchased from Aldrich. Sulfuric acid was purchased from Pharmco-Aaper. Single stranded DNA with sequence d(T)<sub>30</sub> (ssDNA(30T)) were purchased from Integrated DNA Technologies. Single walled carbon nanotubes (SWNT) were purchased from Carbon Nanotechnologies, Inc. All chemicals were used as received without further purification. All solutions were prepared using deionized water (18.2MΩ) (Nanopore water, Barnstead).

### 3.4.2. Dispersion of CNTs into aqueous solution

CNTs were dispersed into deionized water using a method previously described by Zheng *et al* [36]. Briefly, a suspension of CNTs and DNA underwent high powered sonication using a Sonics Vibra-Cell VCX 130 in deionized water. The sonication process was performed in an ice-water bath to prevent local heating of the CNT which may cause unnecessary scission of CNT. After sonication, the sample was centrifuged with a Beckman J2-21 centrifuge at 6000g to remove undispersed CNT. To remove free DNA, the solution was dialyzed with a Microcon YM-50 centrifugal filter unit (Millipore) for 2 hours. The resulting

solution consists of highly dispersed and functionalized DNA-CNTs with a mass concentration of 200-500mg/L. The electronic structure of the dispersed DNA-CNTs was characterized by UV-Visible spectroscopy.

### 3.4.3. In-situ fabrication of self-doped ssDNA/SWNT/PABA nanocomposite

A typical synthetic procedure for the preparation of a water soluble poly (anilineboronic acid)/ssDNA/SWNT nanocomposite (ssDNA/SWNT/PABA) in the presence of fluoride is as follows: An aqueous solution of 40mM ABA and 40mM potassium fluoride was prepared with 0.05M sulfuric acid. Different concentration of ssDNA/SWNT (0%, 0.2%, 1%, etc...) was added to the ABA solution bringing the total volume to 3mL. The quantity of ssDNA/SWNT added is the weight percent based on the amount of ABA monomers in the mixture. The mixture was then purged with nitrogen for 30 minutes to remove dissolved oxygen. APS, the oxidizing agent, was slowly added to this mixed solution over a period of 70 minutes to initiate the polymerization process. This reaction was carried out at 0°C under nitrogen bubbling for an additional 5 hrs. The mixture was left to react overnight in the refrigerator at 4°C. The formed polymer was centrifuged at 4000g for 30 minutes to remove the water soluble oligomers and monomers from the mixture. Dialysis was then performed to remove free DNA and other salts

from the solution. The polymer composite was characterized by UV-Visible spectroscopy after purification.

#### 3.4.4. UV radiation of ssDNA/SWNT/PABA

The following steps were taken to expose the polymer nanocomposites with ultraviolet (UV) light: A known quantity of the polymer solutions were dissolved in de-ionized water. Using UV-Visible spectroscopy, the absorbance intensity of the polymer peak for the polymer samples was adjusted to approximately the same intensity to keep the polymer concentration the same. The polymer solutions, in quartz cuvettes, were then placed 4cm from each other and 7cm from a 3UV multi-wavelength lamp light source (Ultraviolet Products). The samples were then irradiated for different lengths of time and characterized using UV-Visible spectroscopy (UV-Vis), Fourier Transform Infrared spectroscopy (FTIR), and conductance measurements.

#### 3.4.5. Characterization

##### 3.4.5.1 Ultraviolet-Visible-Near Infrared Spectroscopy

All UV spectra were acquired with a Cary 500 UV-Vis-NIR spectrophotometer. The spectra were collected over the range of 200-1100 nm. In preparing the

samples for UV-Vis spectral analysis, an aliquot of the solution was taken and diluted in 3 mL of de-ionized water.

### 3.4.5.2 Fourier Transform Infrared Spectroscopy

All FTIR spectra were obtained using a Spectrum Spotlight FTIR Imaging System with a spectral resolution of  $4\text{ cm}^{-1}$ . The spectra were collected over the range of  $700\text{--}4000\text{ cm}^{-1}$ . In preparing the sample for FTIR analysis, diluted samples of the polymer solutions were dried in vacuum on  $\text{CaF}_2$  windows.

### 3.4.5.3 Two probe conductance measurements

All conductance measurements were obtained using an Electrochemical Workstation CHI 760C coupled to a Micromanipulator 6000 with a Microzoom microscope. In preparing the sample for conductance measurements, diluted samples of the polymer solutions were dried in vacuum on micro interdigitated silicon electrodes (Air Force Research Labs).



### 3.5 References

1. Chandrasekhar, P., *Conducting polymers, fundamentals and applications: a practical approach*. 1999: Kluwer Academic Publishers.
2. Allen, N.S. and M. Edge, *Fundamentals of Polymer Degradation and Stabilisation*. 1992: Elsevier.
3. Klemchuk, P.P., *Environmental Degradation of Polymers*, in *Handbook of Polymer Degradation*, S.H. Hamid, Editor. 2000, Marcel Dekker Inc.
4. Guillet, J.E., *Fundamental processes in the UV degradation and stabilization of polymers*. Pure Appl. Chem, 1972. **30**: p. 135-144.
5. Shlyapnikov, Y.A., S.G. Kiryushkin, and A.P. Marin, *Antioxidative Stabilization of Polymers*. 1996: Taylor & Francis.
6. Zweifel, H., R.D. Maier, and M. Schiller, *Plastics Additive Handbook*. 2009: Hanser.
7. Massey, L.K., *The effects of UV light and weather on plastics and elastomers*. 2007: William Andrew, Inc.
8. Gijssman, P., J. Hennekens, and D. Tummer, *The mechanism of action of hindered amine light stabilizers*. Polym. Deg. Stab., 1993. **39**: p. 225-233.
9. Wallder, V.T., et al., *Weathering studies on polyethylene*. Ind. Eng. Chem., 1950. **42**: p. 2320-2325.
10. Yin, J.J., et al., *The scavenging of reactive oxygen species and the potential for cell protection by functionalized fullerene materials*. Biomaterials, 2009. **30**: p. 611-621.
11. Fenoglio, I., et al., *Reactivity of carbon nanotubes: Free radical generation or scavenging activity?* Free Radical Biol. Med., 2006. **40**: p. 1227-1233.
12. Galano, A., *Carbon Nanotubes as Free-Radical Scavengers*. J. Phys. Chem. C, 2008. **112**: p. 8922-8927.
13. Neoh, K.G. and E.T. Kang, *Spectroscopic studies of protonation, oxidation and light irradiation of polyaniline solutions*. Polymer, 1991. **33**: p. 2292-2297.
14. Sakkopoulos, S., E. Vitoratos, and E. Dalas, *Conductivity degradation due to thermal aging in conducting polyaniline and polypyrrole*. Synth. Met., 1998. **92**: p. 63-67.
15. Rannou, P. and M. Nechtschein, *Aging studies on polyaniline: conductivity and thermal stability*. Synth. Met., 1997. **84**: p. 755-756.
16. Stilwell, D.E. and S.-M. Park, *Electrochemistry of Conductive Polymers*. J. Electrochem. Soc., 1988. **135**: p. 2497-2502.
17. Mazeikiene, R. and A. Malinauskas, *Kinetic study of the electrochemical degradation of polyaniline*. Synth. Met., 2001. **123**: p. 349-354.
18. Malinauskas, A. and R. Holze, *In situ UV-VIS spectroelectrochemical study of polyaniline degradation*. Appl. Polym. Sci., 1999. **73**: p. 287-294.
19. Blinova, N.V., et al., *The chemical and colloidal stability of polyaniline dispersions*. Polym. Deg. Stab., 2005. **88**: p. 428-434.

20. Arsov, L.D., W. Plieth, and G. Kobmehl, *Electrochemical and Raman spectroscopic study of polyaniline; influence of the potential on the degradation of polyaniline*. J. Solid State Electrochem., 1998. **2**: p. 355-361.
21. Son, Y., H.H. Patterson, and C.M. Carlin, *Potential-dependent photoluminescence of conductive polymers: Simple quenching model and experimental results for poly(aniline)*. Chem. Phys. Lett., 1989. **162**: p. 461-466.
22. Pike, G.E. and C.H. Seager, *Percolation and Conductivity: A Computer Study. I*. Phys. Rev. B, 1974. **10**: p. 1421-1434.
23. Ma, Y., et al., *In Situ Fabrication of A Water-Soluble, Self-Doped Polyaniline Nanocomposite: The Unique Role of DNA Functionalized Single-Walled Carbon Nanotubes*. J. Am. Chem. Soc., 2006. **128**: p. 12064-12065.
24. Cheung, W., et al., *Fabrication of high performance conducting polymer nanocomposites for biosensors and flexible electronics: summary of the multiple roles of DNA dispersed and functionalized single walled carbon nanotubes*. J. Mater. Chem., 2009. **19**: p. 6465-6480.
25. Quillard, S., et al., *Vibrational analysis of polyaniline: A comparative study of leucoemeraldine, emeraldine, and pernigraniline bases*. Phys. Rev. B, 1994. **50**: p. 12496-12508.
26. Yan, X.-B., Z.-J. Han, and B.-K. Tay, *Fabrication of Carbon Nanotube-Polyaniline Composites via Electrostatic Adsorption in Aqueous Colloids*. J. Phys. Chem. C, 2007. **111**: p. 4125-4131.
27. Trchova, M., et al., *Evolution of Polyaniline Nanotubes: The Oxidation of Aniline in Water*. J. Phys. Chem. B, 2006. **110**: p. 9461-9468.
28. Zengin, H., et al., *Carbon Nanotube Doped Polyaniline*. Adv. Mater., 2002. **14**: p. 1480-1483.
29. Mizuno, K., et al., *A black body absorber from vertically aligned single-walled carbon nanotubes*. Proc. Natl. Acad. Sci., 2009. **106**: p. 6044-6047.
30. Yang, X., Q. Xie, and S. Yao, *A comparative study on polyaniline degradation by an electrochemical quartz crystal impedance system: electrode and solution effects*. Synth. Met., 2004. **143**: p. 119-128.
31. Rannou, P., et al., *Ageing of PANI: chemical, structural, and transport consequences*. Synth. Met., 1999. **101**: p. 734-737.
32. Otsuka, S., K. Saito, and K. Morita, *Generation of superoxide by adding polyaniline to water*. Chem. Lett., 1996. **8**: p. 615-616.
33. Zheng, M. and V.V. Rostovtsev, *Photoinduced Charge Transfer Mediated by DNA-Wrapped Carbon Nanotubes*. J. Am. Chem. Soc., 2006. **128**: p. 7702-7703.
34. Zheng, M. and B.A. Diner, *Solution Redox Chemistry of Carbon Nanotubes*. J. Am. Chem. Soc., 2004. **126**: p. 15490-15494.
35. Ma, Y., et al., *Improved Conductivity of Carbon Nanotube Networks by In Situ Polymerization of a Thin Skin of Conducting Polymer*. ACS Nano, 2008. **2**: p. 1197-1204.

36. Zheng, M., et al., *DNA-assisted dispersion and separation of carbon nanotubes*. Nat. Mater., 2003. **2**: p. 338-342.

## **Chapter 4**

# **Self-Doped Polyaniline/Carbon nanotube composites for Construction of Efficient Enzyme Based Biofuel Cells**

## **4.1 Introduction**

Slow electron transfer rate is a fundamental problem that limits the use of redox enzymes, such as glucose oxidase, in biological fuel cells because of the lack of direct electron transfer between redox enzymes and electrode supports. This is mainly because the redox center of the enzyme is embedded in a thick and nonconductive protein shell, which results in spatial separation from the electrode surface. Therefore tremendous efforts have been devoted to constructing enzymatic electrodes which have direct electron transfer between the redox center and electrode support to increase the electron transfer rate and therefore the efficiency of biofuel cells [1-9].

Conducting polymer and CNT composites have been used as electrode materials to develop enzymatic based sensors and biofuel cells [3, 10-13]. SWNTs have been used as long range nanoconnectors to electrically contact the active site to the electrode surface [3]. The SWNTs were vertically aligned on the electrode surface and the enzymes (glucose oxidase (GOx)) were reconstituted on the top of the tubes. It was shown that electron transfer from the active site to

the electrode from a distance as far as 150nm was possible and the rate of electron transfer was dependent on the length of the SWNT. Using a layer by layer electrostatic assembly approach, the glucose oxidase modified SWNTs with cationic redox polymers on the electrode surface showed current densities of  $440\mu\text{A}/\text{cm}^2$ , which is 2-fold higher than that with SWNTs alone [12]. Layers of repeating glucose oxidase modified SWNT (GOx/SWNT) and a cationic redox polymer was formed on the electrode surface and it was shown that 75% catalytic activity was retained even after 30 days. Direct electron transfer of glucose oxidase was also shown for CNT/chitsan matrices [11]. The electrode was modified with a GOx trapped CNT/chitosan matrix with an electron transfer rate of  $3.1\text{s}^{-1}$ .

Besides CNTs, conducting polymers and their composites have also been used to facilitate electron transfer to the electrode [14-16]. Electrodes modified with nanorods of polyaniline/gold nanoparticles (PANI/Au) composite was shown to have a 25-fold increase in electron transfer rate compared to a polyaniline/poly(4-styrene-sulfonate) nanorod system. The increase in electron transfer rate was attributed to the higher surface area and conductivity of the PANI/Au nanorod composite. An amperometric glucose biosensor based on trapping GOx in the inner walls of aligned polyaniline nanotubes was also demonstrated and showed an electron transfer rate of  $5.8\text{s}^{-1}$  [16].

Although there are many methods for assembling the electrodes for bioelectrocatalysis of glucose oxidase, systematic studies on assembling the

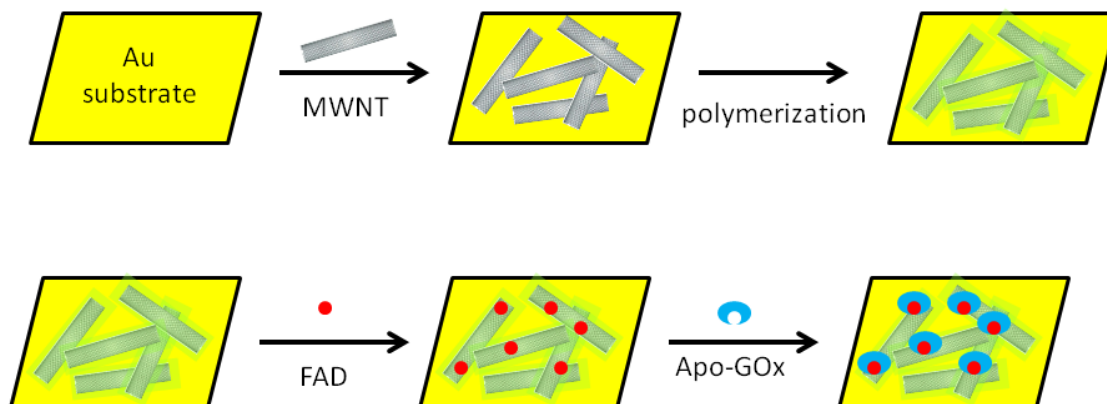
electrode to achieve optimum direct electron transfer between the redox enzymes and electrode supports as well as how each parameter affects the electron transfer rate has not been studied.

In this chapter, we will systematically study how the conducting polymer thickness and the carbon nanotube arrangement influence electron transfer between redox enzymes and electrodes, and therefore influence the enzymatic catalytic behavior. Another important aspect of this work is to control the orientation of the redox center relative to the electrode surface. We modified the electrode surface by in-situ fabrication of polyaniline/ss-DNA-SWNT composites with different functional groups. In one case, the composite formed has boronic acid functional groups along the polyaniline backbone for binding to native flavin adenine dinucleotide (FAD) via its diol moiety. Glucose oxidase was reconstituted on the FAD conjugated composite surface to yield an electrically contacted enzyme-electrode. In the other case, the composite formed had carboxyl functional groups on the polyaniline backbone. This allows FAD that was chemically modified with an amine group to bind to the composite. Glucose oxidase was then reconstituted following the same protocol. We found that this subtle orientation change of the redox center dramatically influences glucose binding to the reconstructed enzymes and also their electrocatalytic capability to oxidize glucose. The results provide an important fundamental understanding on constructing efficient electrode materials for glucose sensors and practical enzyme-based biological fuel cell in the future.

## 4.2 Results and Discussion

### 4.2.1. Fabrication, optimization, and characterization of composite modified electrodes for glucose oxidation

The construction of the anode or cathode of an enzymatic biofuel cell normally entails the assembly of different molecules and enzymes on the electrode surface. This introduces various resistances to the system and consequently lowers the power output of the biofuel cell. Leger *et al.* [17] have described redox enzyme modified electrodes as a series of resistors. The catalytic efficiency of the enzyme and the electron transfer rate from the active site of the enzyme to the electrode are crucial and plays important roles in the power output of the system. Scheme 4.1 shows an illustration of how the anode will be assembled in this work. As shown, the assembly of the anode consists of multiple steps which can contribute to the overall resistance. To minimize resistance and obtain the maximum performance, each immobilization step shown in Scheme 4.1 was studied and optimized.



**Scheme 4.1:** Illustration showing the assembly of the anode. The gold substrate was first modified with a ligand which allows electrostatic binding to negatively charged ssDNA/MWNT. After immobilization of ssDNA/MWNT, a thin layer of PABA was formed on its surface. A reconstitution approach was used to immobilize glucose oxidase to the gold surface. The FAD cofactor was immobilized via the boronic acid moiety of PABA. Apo-glucose oxidase was finally used to reactivate the enzyme for bioelectrocatalysis

Based on the results from previous chapters, ssDNA/MWNTs were the most efficient type of CNTs in terms of forming polymer composites with high conjugation length and conductivity. In addition, the MWNTs can help stabilize the polymer from degradation and therefore maintain its high performance in a biofuel cell. More importantly, MWNTs have high surface area and through surface functionalization enzymes can be loaded onto its surface (direct electron transfer) to increase glucose oxidation sensitivity and current density [5]. Direct electron transfer between glucose oxidase and CNTs have been shown, however in these cases the high overpotential limits its use in practical applications [3, 10]. In an attempt to improve the overpotential and current density, we have proposed the use of ssDNA/MWNT/PABA composite. From one of our recent works, we



found that the electrical performance of SWNT networks can be significantly improved by in situ polymerization of a thin layer of PABA on ssDNA/SWNTs [18]. The conductance of the formed polymer composite was found to be ~80 times higher than that of ssDNA/SWNT alone. The higher conductance compared to ssDNA/SWNT networks is attributed to the decrease in contact resistance between SWNTs by forming a highly conductive polymer layer (PABA) along the SWNT surface. Therefore, the use of CNT/polymer composite in assembling the anode is expected to have a lower resistance than CNT itself and should facilitate electron transfer. Furthermore, the boronic acid groups along the PABA backbone can be used to directly and chemically anchor the redox center (FAD) to further facilitate direct electron transfer with the electrode surface. This reconstitution method is used because it brings the active site in close contact with the surface of the electrode. This shortens the distance between them and electrons produce during glucose oxidation can travel to the electrode with minimal resistance.

To optimize the thickness of the PABA layer on the carbon naotubes, we determine the amount of monomer necessary to form a highly conductive PABA/CNT composite. Both AFM and 4-probe conductance measurements were used. Percolation curves of ssDNA/MWNT/PABA for three different ABA concentrations are shown in Figure 4.1 As the ABA concentration is increased, more polymers are formed on the carbon nanotubes and the conductance of the composite decreased, which is very different from those observed in SWNTs [18-

19]. The reason for this different behavior is not known yet and further studies are required. On the other hand, the conductivity of CNTs is much higher than that of PABA, therefore forming a thick layer of PABA would act as a semi-insulating layer.

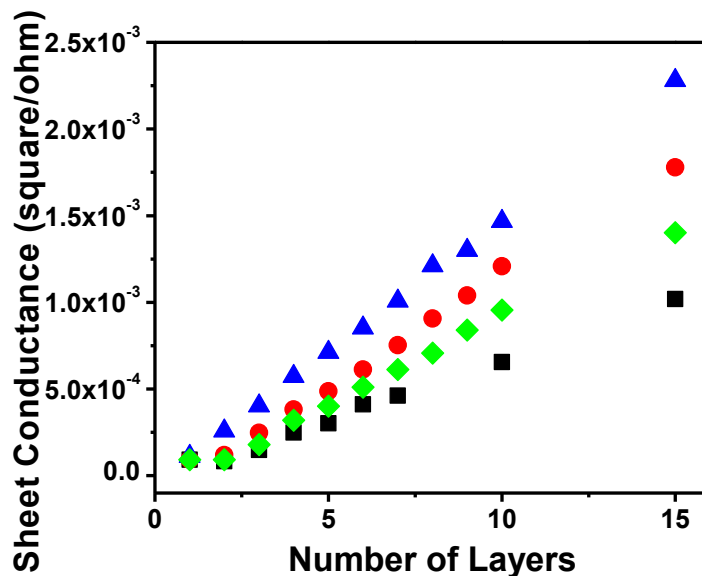


**Figure 4.1:** Conductance profile for in-situ polymerized ssDNA/MWNT/PABA composite with ABA concentrations of (blue) 0.75mM, (red) 1.5mM, (green) 2.25mM, and (black) 4.5mM

Since the conductance increases consistently with a decrease in polymer coating, AFM studies were carried out to determine which concentration of ABA is optimal for forming a uniformly thin layer of PABA on the MWNT surface. The AFM of the composites formed is shown in Figure 4.2. The composite formed using 1.5mM ABA (Figure 4.2a) shows some MWNTs that are only partially covered with PABA (white arrows). 2.25mM ABA (Figure 4.2b) shows uniform

polymer coating on the ssDNA/MWNTs. 4.5mM ABA (Figure 4.2c) shows thick layers of polymer (white arrows) and non-uniform coating. Based on the percolation data, the lower concentrations of ABA used for in situ polymerization has a higher conductance. However, from the AFM data 2.25mM ABA shows the most uniform polymer coating on the ssDNA/MWNT surface. The boronic acid moiety on the PABA backbone is used to immobilize glucose oxidase and since glucose oxidation efficiency is of interest, 2.25mM ABA was chosen as the optimal monomer concentration. Although this is not optimal in terms of its conductivity, theoretically it gives the highest boronic acid functional groups on the surface. This allows for optimal FAD and enzyme loading and therefore should give higher glucose oxidation efficiency.

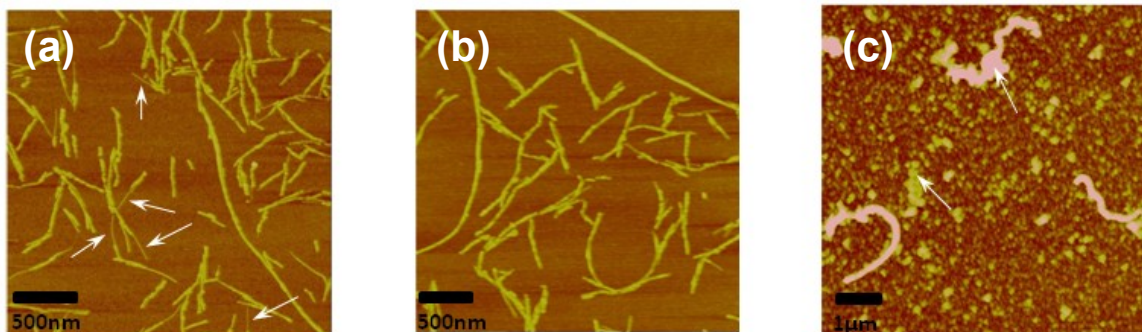


**Figure 4.2:** AFM images of ssDNA/MWNT/PABA with ABA concentrations of (a) 1.5mM, (b) 2.25mM, and (c) 4.5mM

After forming the polymer, the diol group of FAD cofactor was immobilized onto the PABA backbone through the boronic acid moiety. Boronic acids are known to react with diol groups to form boronate esters [20]. Since FAD is a

redox cofactor, electrochemical techniques can be used to study the electrochemical property of the immobilized FAD and also monitor their loading. Figure 4.3a shows a typical CV graph of the FAD modified gold electrode at different scan speeds. A characteristic peak at -0.4V is seen and is attributed to the oxidation peak for FAD. The CV shows a very small FAD oxidation peak and a very large charging current. The small peak may be due to low concentrations of FAD immobilized on the surface and the large charging current may be from the exposed gold surface. To view the peak more clearly, differential pulse voltammetry (DPV) was used (Figure 4.3b). As shown, the peak potential is at  $\sim$ -0.45V and is characteristic of the FAD oxidation peak.

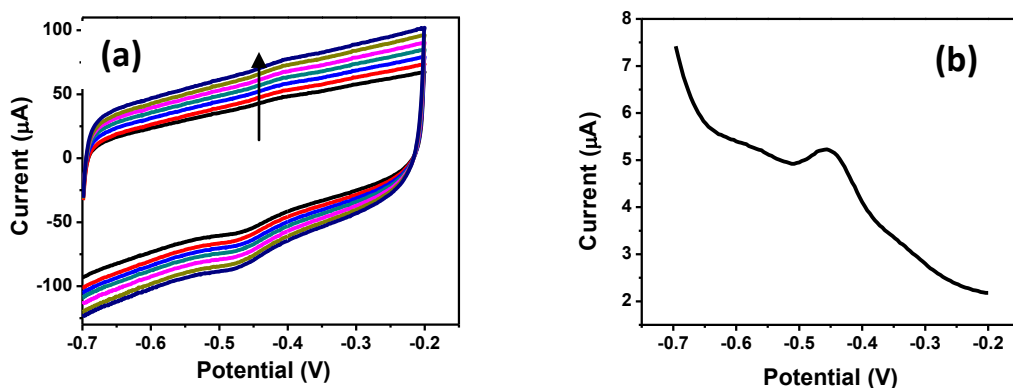


**Figure 4.3:** (a) Cyclic voltammogram of FAD modified electrode at different scan rates. Scan rates range from 9-20V/s. The direction of the arrow in the figure indicates increasing scan rate. (b) Differential pulse voltammogram of the FAD modified electrode

Another important piece of information that can be obtained from the CV curves is if the FAD is actually attached to the modified gold electrode. A linear relationship is shown between the peak current and the scan rate (Figure 4.4b), which is representative of a surface confined redox species [21]. Therefore, the FAD is attached to the polymer composite modified gold electrode.

### Electron transfer rate determination using Laviron Analysis

Using cyclic voltammetry, the electron transfer rate of redox active molecules like FAD can be determined using Laviron's theory [22]. At low scan rates (<1V/s) the peak-to-peak potential separation ( $E_p = E_{pa} - E_{pc}$ ) of the FAD modified electrodes is ~60mV (not shown in Figure), indicating a reversible electrochemical reaction with a fast electron transfer rate. At higher scan rates, the  $E_{pa}$  shifts to more positive potentials and the  $E_{pc}$  shifts to more negative potentials. This is because at higher scan rates the system becomes more irreversible. The change in peak separation,  $\Delta E_p$ , can be plotted with the logarithm of scan rate to obtain a Laviron plot (Figure 4.3b). By obtaining the slope of the linearly fitted curve (red line in the figure), the electron transfer coefficient,  $\alpha$ , can be determined. Using  $\alpha$ , the electron transfer rate constant can be determined using the laviron equation:

$$\log k_{ET} = \alpha \log(1 - \alpha) + (1 - \alpha) \log \alpha - \log \frac{nFE_p}{2.3RT} - \alpha(1 - \alpha) \frac{RT}{nFv}$$

where  $k_{ET}$  is the electron transfer rate constant,  $\alpha$  is the electron transfer coefficient,  $F$  is Faraday's constant,  $R$  is the gas constant,  $T$  is the temperature,  $n$  is the number of electrons involved in the redox process,  $E_p$  is the peak potential, and  $v$  is the scan rate.

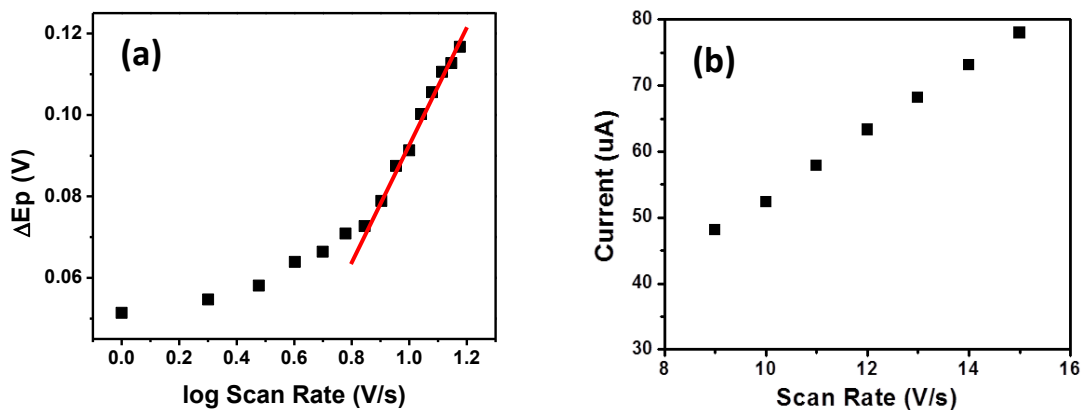


**Figure 4.4:** (a) Typical Laviron analysis plot of FAD oxidation peak (b) peak current as a function of scan rate.

The electron transfer rate constant obtained using the Laviron analysis was used as a way to determine the efficiency of the assembled electrode and to further optimize other parameters that may affect its performance. As mentioned previously, electron transfer rate from the active site to the electrode is important for the overall efficiency of the biofuel cell. All molecules used to anchor FAD to the electrode surface (between the active site and the electrode) introduce resistance which can affect electron transfer rate. Therefore, the optimization of all layers of molecules used between the active site and the electrode is

necessary to improve the efficiency of biofuel cells. From scheme 4.1 and the experimental section, we see that the molecules used to immobilize FAD are 1) the linkers used to immobilize MWNT to the gold electrode surface, 2) the MWNT itself, 3) the polymer coating on the MWNT. Since we have already optimized the polymer coating above, optimization of parameters such as the thickness of the ssDNA/MWNT used and the different linkers used to attach ssDNA/MWNT to the gold surface is necessary. It was found that thick layers of ssDNA/MWNT have low FAD electron transfer rates. This is attributed to the large resistance formed in the MWNT network. In addition, different linkers used to modify the gold surface prior to ssDNA/MWNT immobilization also affect the overall FAD electron transfer rate. The use of conjugated linkers showed a slightly higher electron transfer rate than hydrocarbon linkers. The conjugated linkers provided less resistance than the hydrocarbon linkers. The summary of different optimization parameters are summarized in Table 4.1.

	<b>FAD electron transfer rate</b>
<b>Thick Layer of MWNT with 4-aminothiophenol linker</b>	<b>75s<sup>-1</sup></b>
<b>Thin Layer of MWNT with 4-aminothiophenol linker</b>	<b>288s<sup>-1</sup></b>
<b>Thin Layer of MWNT with Cysteamine linker</b>	<b>270s<sup>-1</sup></b>

**Table 4.1:** Table of different parameters and their calculated FAD electron transfer rate constant.

A reconstitution approach was used to attach the glucose oxidase enzyme to the surface of the electrode [23]. Reconstitution involves first separating the embedded redox cofactor from the enzyme, which deactivates the enzyme. The cofactor is then immobilized onto the electrode surface through different surface modification techniques. After immobilization of the cofactor, the apo-enzyme is reattached to the cofactor that is immobilized on the surface, reactivating the enzyme in the process. This process has the advantage of bringing the active site as close to the electrode surface as possible, facilitating direct electron transfer.

The immobilization of FAD, the redox cofactor, can be monitored using electrical impedance spectroscopy. Impedance spectroscopy is an electrochemical technique which can be used to study transport properties of materials as well as electrochemical reactions occurring at interfaces. Impedance measures the resistance of a current passing through as a small periodic voltage is applied. The potential applied is normally expressed as:

$$E = E_0 \sin(\omega t)$$

where  $E$  is the potential at time  $t$ ,  $E_0$  is the amplitude of the signal and  $\omega$  is the radial frequency ( $\omega = 2\pi f$ , where  $f$  is the frequency). The current response that is phase shifted is expressed as:

$$I = I_0 \sin(\omega t + \phi)$$



where  $I$  is the current response,  $I_0$  is the amplitude of the current, and  $\phi$  is the phase shift. Using both Ohm's Law and Euler's relationship, the impedance,  $Z$ , can be expressed as a combination of real and imaginary components:

$$Z(\omega) = \frac{E}{I} = Z_0 e^{j\phi} = Z_0 (\cos\phi + j\sin\phi)$$

The real component of the impedance represents the total opposition to the passage of current by pure resistance in the system. The complex component of the impedance represents the opposition to the passage of current due to capacitance and inductance. The impedance of a system can be represented graphically as a Nyquist plot ( $Z_{\text{img}}$  plotted with  $Z_{\text{real}}$ ) or a Bode plot ( $Z$  plotted with  $\phi$  or  $f$ ). A typical Nyquist plot normally shows a semicircle at high frequencies that represents a diffusion controlled process and a linear component at low frequencies due to mass transport. From the Nyquist plot, various information about the electrochemical reaction at the interface can be obtained such as the charge transfer resistance (determined from the diameter of the semicircle), the time constant and double layer capacitance (determined from the maximum of the semicircle). Electrochemical impedance spectroscopy have been used extensively for determining polymer coating efficiencies and fuel cell efficiencies [24-25].

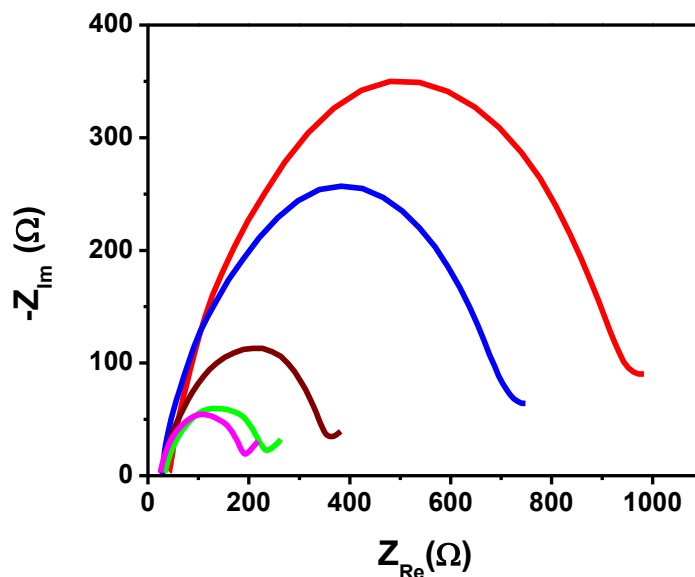


**Figure 4.5:** Nyquist plot of FAD immobilization on polymer composite modified gold electrode at different time intervals: (red) 0 mins, (blue) 30 mins, (brown) 60 mins, (green) 120 mins, and (magenta) 300 mins. The impedance was scanned at -0.45V.

In our current case, the voltage applied was -0.45V, which is the same potential where the FAD redox reaction occurs. The results are shown in Figure 4.5. As shown, the impedance decreases as more FAD is loaded onto the gold surface.

After FAD loading, the immobilization of apo-glucose oxidase to complete the reconstitution approach can also be monitored using impedance spectroscopy (Figure 4.6). As more apo-glucose is loaded onto the surface, the impedance increases. The results shown are comparable to literature [26]. The dramatic increase in impedance is due to the insulating shell of apo-glucose

oxidase. The insulating shell have been shown to limit the diffusion of redox probes to the electrode surface and interfacial electron transfer resistance largely controls the impedance [27].

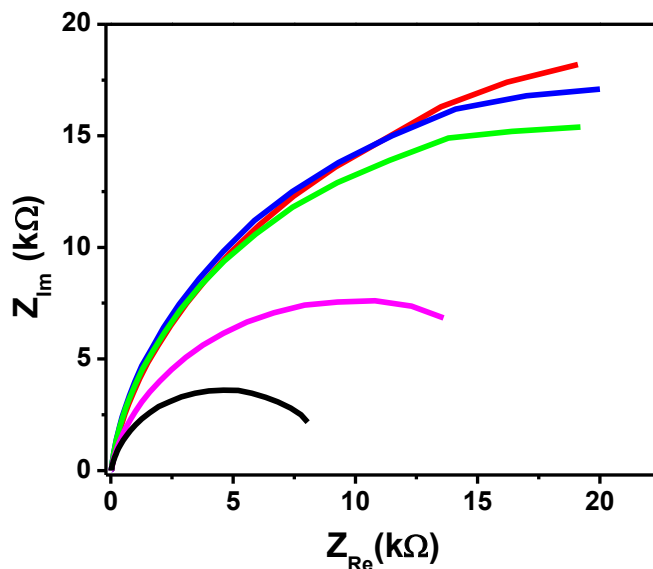
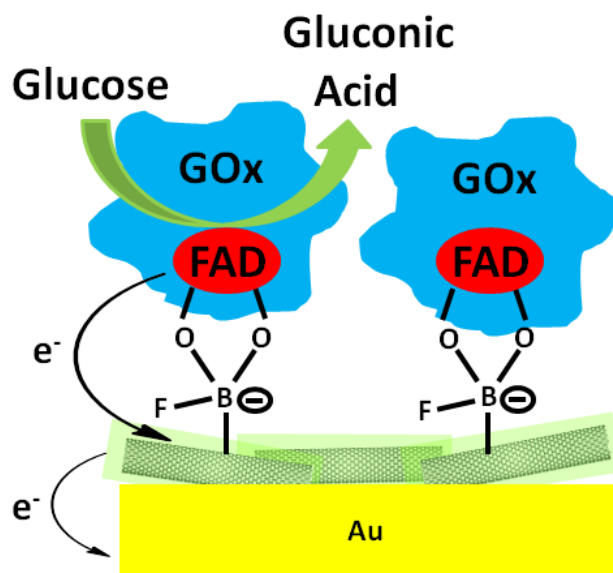


**Figure 4.6:** Nyquist plot of apo-glucose reconstitution on FAD modified gold electrode at different time intervals: (black) 1hr, (magenta) 2 hrs, (green) 4 hrs, (blue) 5hrs, and (red) 17hrs.

#### 4.2.2. Glucose oxidation of reconstituted enzyme modified electrode

The optimized GOx modified electrode was then tested for its glucose oxidation efficiency. An illustration of the glucose oxidation is shown in scheme 4.2. As glucose is added to the system, it gets oxidized by the glucose oxidase enzyme at the active site. The electron gained from the oxidation process is

transferred from the FAD (which is reduced to FADH<sub>2</sub> in the process;  $\text{FAD} + 2\text{H}^+ + 2\text{e}^- \leftrightarrow \text{FADH}_2$ ) to the polymer composite and then to the electrode. Since the apo-glucose was reconstituted onto the gold electrode, the FAD unit is oriented so that it is close to the electrode surface, facilitating electron transfer. In addition, due to the high conductivity displayed by the conducting polymer composite and its high surface area which allows higher loading of the enzyme, an enhanced glucose oxidation rate is expected.



**Scheme 4.2:** Scheme showing the glucose oxidation of the assembled anode

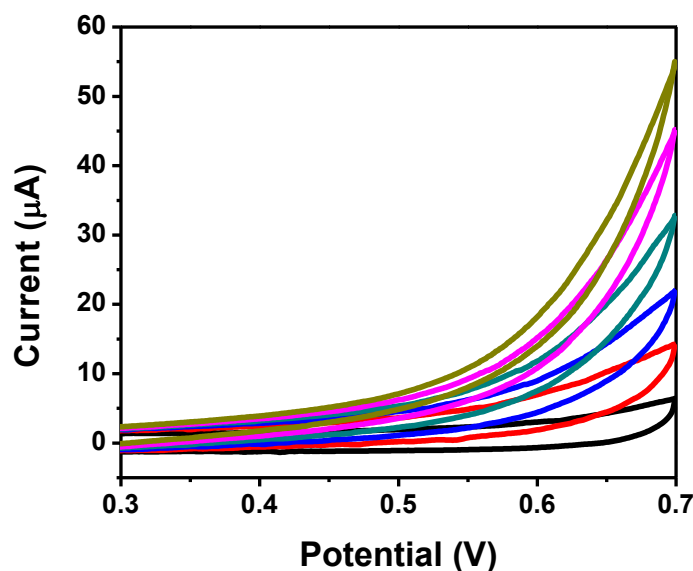


**Figure 4.7:** CV showing glucose oxidation of the assembled anode at different glucose concentrations: (black) 0mM, (red) 1mM, (blue) 5mM, (green) 10mM, (pink) 20mM, (brown) 50mM

Glucose oxidation of the assembled anode was monitored using CV (Figure 4.7). As shown, higher glucose concentrations causes the current to increase at  $\sim 0.5V$ . The increase in current indicates the bioelectrocatalytic oxidation of glucose [6]. The unimolecular electron transfer was calculated to be  $\sim 3500s^{-1}$ , which is  $\sim 2.5$  times higher than that reported in some literatures [28]. The overpotential, which is the difference between the experimental applied potential and the standard potential of FAD, of this assembled system is fairly high. Currently we do not understand what caused this large overpotential. One of the possible reasons is the steric effects imposed by closely immobilized apo-Gox on the gold electrode surface. Apo-Gox must be bound to FAD in order for it

to be active for glucose oxidation. It is possible that apo-GOx does not bind to FAD in a vertical fashion as depicted in scheme 4.2; it may bind at an angle. If two apo-GOx binds very close to each other, sterics can cause inefficient binding between the apo-Gox and the FAD therefore reducing its efficiency.

To study the steric effect that can be caused by adjacent enzymes attached to the electrode surface, the polymerization method was modified. Instead of using just ABA monomer to form the polymer on the MWNT surface, ABA monomers were copolymerized with ANI monomers (which have no functional groups). The purpose of this is to decrease the amount of boronic acid groups on the surface of the formed polymer. If the concentration of boronic acid groups decreases then the amount of FAD attached to the surface should also decrease. If the hypothesize proposed above is true then decreasing the FAD loading on the surface should increase the biocatalytic oxidation of glucose. The glucose oxidation of the copolymerization of different ratios of ABA to ANI is shown in Figure 4.8. From the figure, as the concentration of ABA decreases the catalytic efficiency also decreases. It appears that the binding of apo-GOx to FAD in the current approach to assemble the anode is optimal and no steric effects are present.

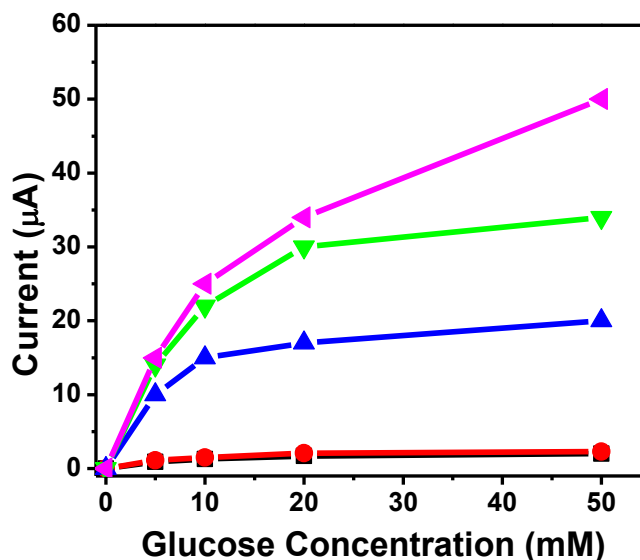


**Figure 4.8:** Biocatalytic oxidation of glucose with different densities of boronic acid groups: (magenta) ABA/ANI = 1, (green) ABA/ANI = 0.75, (blue) ABA/ANI = 0.5, (red) ABA/ANI = 0.25 and (black) 0% ABA/ANI = 0

### 4.2.3. Glucose oxidation of enzyme immobilized MWNT arrays

As mentioned, the assembly of ssDNA/MWNT on the gold electrode may not be optimal, thus leading to the high overpotential seen. It is possible that when forming the monolayer of ssDNA/MWNT on the surface, most of the ssDNA/MWNTs are attached to the surface of the electrode where the longitudinal axis is parallel to the electrode surface. In this case, a large portion of the ssDNA/MWNT is not used for immobilization of the enzyme, thus decreasing enzyme loading efficiency. In addition, the electrostatic immobilization

of the ssDNA/MWNT to the electrode may also introduce large contact resistance between the tubes and the electrode surface. To solve this problem, we purchased vertically aligned MWNT arrays directly grown on a metallic surface (NanoLab) and used them as our electrode surface. The SEM image of the aligned MWNT arrays is shown in Figure 4.9. The surface of the aligned arrays is fully covered with MWNTs and has a very high surface area, allowing more enzymes to be immobilized. It is expected that the MWNT arrays will help increase the enzyme loading, catalytic efficiency and lower the overpotential.

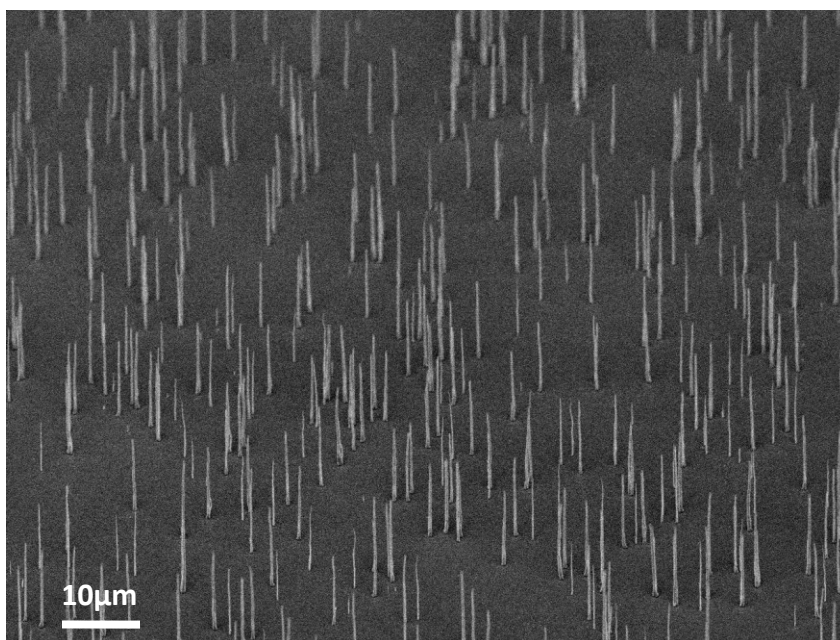


**Figure 4.9:** SEM image of MWNT array



The polymerization of ABA and the immobilization of FAD were performed using the same approach for the dispersed ssDNA/MWNT. The CV for the FAD modified MWNT array is shown in Figure 4.10. Using the Laviron analysis, the FAD electron transfer rate was determined to be  $\sim 500\text{s}^{-1}$ , which is much faster than that reported in literature [15].

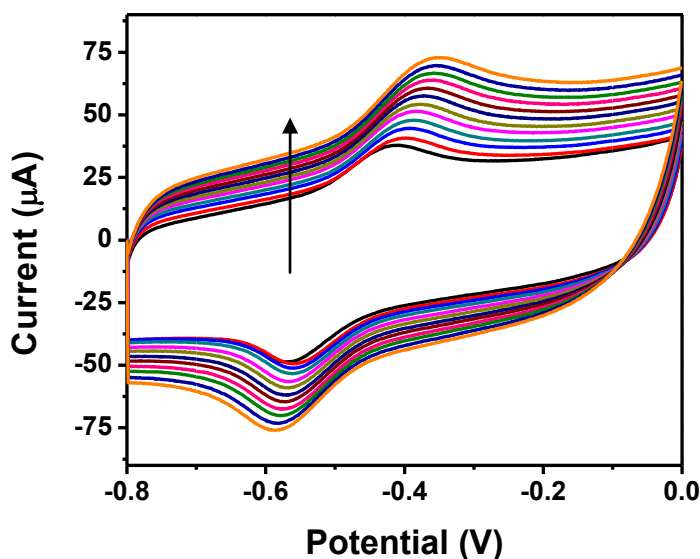


**Figure 4.10:** CV of FAD modified MWNT array at different scan rates. Scan rates are from 9-20V/s. The direction of the arrow in the figure indicates increasing scan rate.

The biocatalytic oxidation of glucose was also tested for the enzyme immobilized MWNT array. The results are shown in Figure 4.11. In Figure 4.11a, the current obtained for the glucose oxidation is  $\sim 3$  orders higher than the dispersed ssDNA/MWNT shown in Figure 4.7. In addition, the overpotential is less than that of the dispersed ssDNA/MWNT approach. Glucose oxidation is

shown to occur at  $\sim 0.35\text{V}$  for the array, which is  $150\text{mV}$  less positive than the dispersed ssDNA/MWNT constructed electrodes. Although there is an improvement, the overpotential is still fairly large. Figure 4.11b shows the Michaelis-Menten graph of glucose oxidation using the MWNT array. In enzyme kinetics, the turnover rate or  $k_{\text{cat}}$  can be determined from  $V_{\text{max}}$  and the enzyme concentration. Using the figure and the total surface coverage of enzymes molecules, the  $k_{\text{cat}}$  for the MWNT array was determined to be  $\sim 3 \times 10^4 \text{s}^{-1}$ . The turnover rate is  $\sim 6$  times larger than that reported by Xiao *et al* [6].

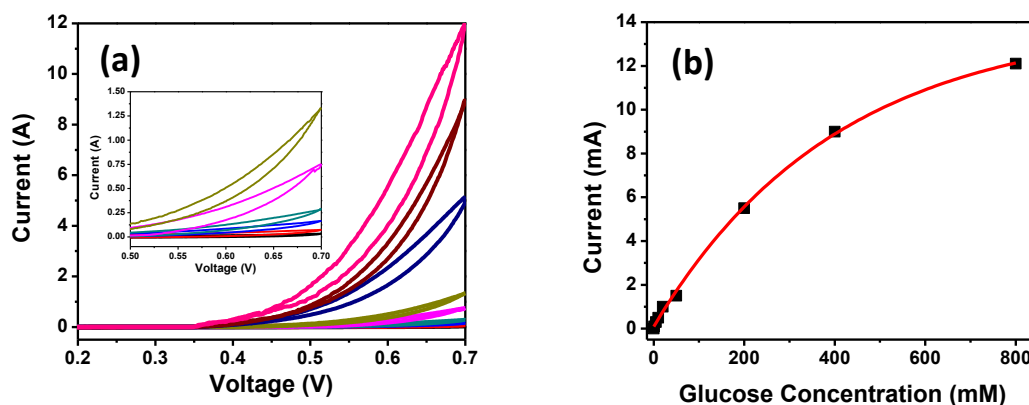


**Figure 4.11:** (a) Biocatalytic oxidation of glucose using the MWNT array at different glucose concentrations: (black) 0mM, (red) 1mM, (blue) 5mM, (green) 10mM, (magenta) 20mM, (olive) 50mM, (blue) 200mM, (brown) 400mM, and (pink) 800mM. The inset shows a zoom in image of the biocatalytic oxidation at lower glucose concentrations. (b) Michaelis-Menten graph of biocatalytic oxidation of glucose using the MWNT array.

#### 4.2.4. Effect of enzyme orientation on glucose oxidation

It is well known that the orientation of the enzyme when binding with a substrate is very important for its catalytic efficiency. Inspired by this, we controlled the orientation of glucose oxidase immobilized on the electrode surface and studied their biocatalytic efficiency. This was accomplished by orienting the FAD molecule in different positions and immobilizing it to the surface. Figure 4.12 shows the structure of FAD. The anode that was assembled for glucose oxidation combined the boronic acid group of PABA and the diol group of FAD to form a boronate ester. Buchmann *et al* [29] have shown that FAD can be modified at the adenosine. Using this approach, Katz *et al* [30] modified the adenosine with a ferrozine and use it for glucose oxidation. The ferrozine acted as a mediator for electron transfer to the electrode surface. Motivated by the number of places that FAD can be modified, we believe that it can be immobilized on the electrode in different ways. The orientation which FAD is used to immobilize onto the electrode surface can impact the how the enzyme apo-enzyme is oriented as well. This may influence the catalytic efficiency of glucose oxidation.

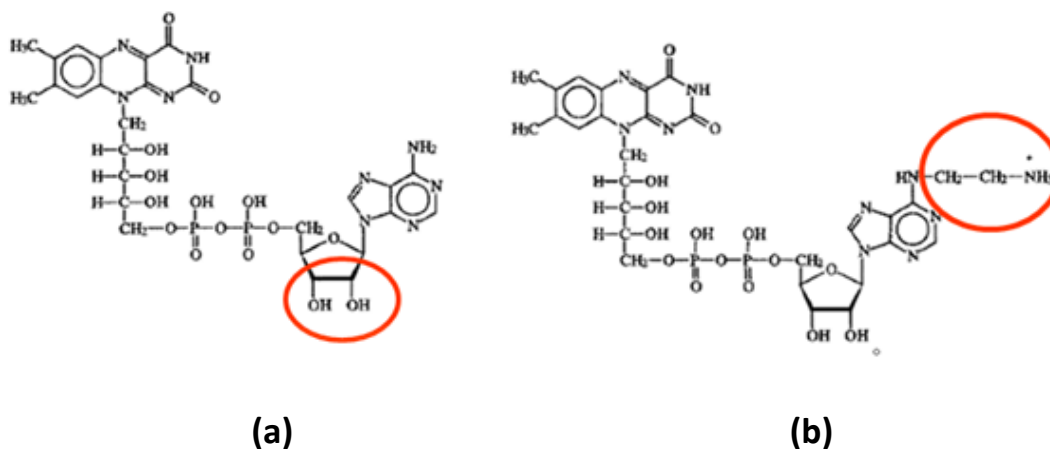


**Figure 4.12:** Chemical structure of (a) FAD and (b) FAD-NH<sub>2</sub>

To test the catalytic efficiency of the enzymes that is oriented differently on the gold electrodes, 3-aminobenzoic acid monomers (ANI-COOH) were used. Structurally, ANI-COOH is similar to ABA. The only difference is that instead of having a boronic acid functional group, ANI-COOH has a carboxyl functional group. The polymerization of the monomer to form the thin layer of polymer on the surface of the ssDNA/MWNT was the same. The immobilization of FAD onto the electrode, however, is different. FAD was first modified at the adenosine group to obtain N6-(2-aminoethyl)-FAD (FAD-NH<sub>2</sub>). Using EDC/NHS coupling chemistry, FAD-NH<sub>2</sub> was covalently attached to the PANI-COOH backbone. Using impedance spectroscopy, the resistance from both FAD and the apoglucose oxidase was kept the same. This implies that if the orientation does not

influence the glucose oxidation efficiency then the results from both samples should be similar.

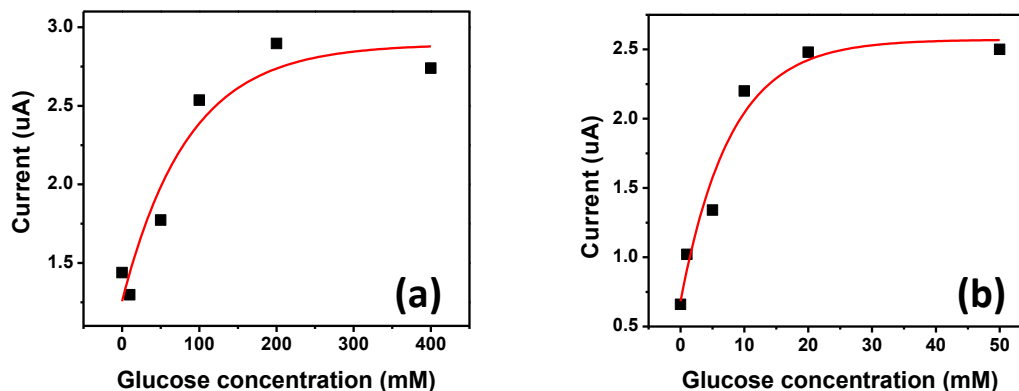


**Figure 4.13:** Michaelis-Menten graphs of enzyme modified gold electrodes using (a) ABA monomers and (b) ANI-COOH monomers

The biocatalytic oxidation of glucose was performed using both assembled anodes and the Michaelis-Menten graphs are shown in Figure 4.13. Based on the data, it appears that the approach using ANI-COOH has a higher catalytic efficiency (lower glucose concentrations are needed to obtain same current). Therefore by changing the orientation of the FAD immobilized on the surface of the electrode, we can possibly improve the overpotential further. Since the resistance between the active site and the electrode surface is kept the same, the changes seen are due to orientation effect on glucose oxidation efficiency. The Michaelis-Menten constant ( $K_m$ ) can also be obtained from the graph. Based on the  $K_m$ , glucose binding with glucose oxidase is stronger for the approach

using PANI-COOH than PABA. Further studies are needed for a deeper understanding of the interesting phenomenon shown.

## 4.3 Conclusion

In summary, we have developed an approach to assemble the anode of a biofuel cell with high electron transfer efficiency. This was accomplished by using ssDNA/MWNT/PABA composites. Thin layer polymer composites have the advantage of high conductivity due to a low contact resistance and high surface area for enzyme loading. It was also found that parameters such as the thickness of polymer layer, thickness of MWNT layer and the linker used to modify the electrodes can affect the electron transfer rate. Using all the optimized conditions the biocatalytic oxidation of glucose showed a turnover rate of  $3500\text{s}^{-1}$ . To improve the efficiency and overpotential, vertically aligned MWNT arrays were used. The MWNT arrays have a higher surface area than the dispersed ssDNA/MWNT and its surface is fully covered with MWNTs. The same approach was used to assemble the MWNT array and the biocatalytic oxidation was studied. The MWNT array showed a turnover rate of  $3 \times 10^4\text{s}^{-1}$ , which is much higher than those reported in literature. Through surface modification, the enzymes were immobilized onto the surface with different orientations. It was shown that the FAD immobilized through the adenosine moiety had a higher catalytic efficiency than FAD immobilized through the diol moiety of the ribose sugar. Using the studies shown in this chapter, biofuel cells with very high

catalytic efficiencies and power output can be made through surface engineering of carbon nanotubes.

## 4.4 Experimental

### 4.4.1. Reagents

3-aminophenylboronic acid hemisulfate salt, 3-aminobenzoic acid, potassium fluoride, 4-aminothiophenol, molecular sieves (3Å), 3-mercaptopropionic acid, MES hydrate, ammonium sulfate, sodium acetate, sodium chloride, potassium phosphate monobasic, potassium phosphate dibasic trihydrate, glucose oxidase, flavin adenine dinucleotide disodium salt, and N-(3-Dimethylaminopropyl)-N'-ethylcarbodiimide hydrochloride were all purchased from Sigma Aldrich. N-Hydroxysulfosuccinimide sodium salt was purchased from Fluka Analytical. Sodium hydroxide and ethyleneimine were purchased from Fischer Scientific. Sulfuric acid was purchased from pharmco-aaper. Beta-D-Glucose was purchased from MP Biomedicals. Single walled carbon nanotubes were purchased from Unidym. Multiwalled carbon nanotubes were purchased from Nanolab. All chemicals purchased were used without further purification. Single stranded DNA with sequence d(T)<sub>30</sub> (ssDNA(30T)) was purchased from Integrated DNA Technologies.



#### 4.4.2. Dispersion of CNTs into aqueous solution

CNTs were dispersed into deionized water using a method previously described by Zheng *et al* [31]. Briefly, a suspension of CNTs and DNA underwent high powered sonication using a Sonics Vibra-Cell VCX 130 in deionized water. The sonication process was performed in an ice-water bath to prevent local heating of the CNT which may cause unnecessary scission of CNT. After sonication, the sample was centrifuged with a Beckman J2-21 centrifuge at 6000g to remove undispersed CNT. To remove free DNA, the solution was dialyzed with a Microcon YM-50 centrifugal filter unit (Millipore) for 2 hours. The resulting solution consists of highly dispersed and functionalized DNA-CNTs with a mass concentration of 200-500mg/L. The electronic structure of the dispersed DNA-CNTs was characterized by UV-Visible spectroscopy.

#### 4.4.3. Preparation of ssDNA/MWNT functionalized gold electrodes

ssDNA/MWNTs were immobilized onto the gold electrode surface through electrostatic interactions. This was accomplished by placing the gold electrode surfaces into a solution containing 30mM of 4-aminothiophenol and left to react overnight. The gold surfaces were then rinsed with deionized water, placed in a solution of ssDNA/MWNT and left to react overnight. The gold electrode surfaces were dried and cleaned, leaving a monolayer of ssDNA/MWNT.

#### 4.4.4. In-situ fabrication of self-doped ssDNA/MWNT/polymer nanocomposite

An aqueous solution of 2.5mM ABA (or 2.5mM ANI-COOH) monomer and 40mM KF prepared with 0.05M sulfuric acid was subsequently added to the surface of the immobilized ssDNA/MWNT functionalized gold electrode surfaces. It was allowed to react for 2hrs. The modified gold electrodes were then washed and dried. Afterwards, 100uL of 0.05M sulfuric acid solution was added to the gold surface and the polymerization was initiated by APS, the oxidizing agent. A total of 13uL APS (40mM) was slowly added over the course of 2hrs. The polymerization reaction was performed at low temperatures (4°C) to obtain highly conjugated PABA and to prevent side reactions such as polymer branching. After the last addition of APS, the sample was left to further polymerize for an additional hour. The ssDNA/MWNT/polymer gold surface was then washed with deionized water to remove free monomers, APS, KF, and other non-bound materials.

#### 4.4.5. Characterization of self-doped CNT/polymer nanocomposite on gold substrate

The MWNT/polymer nanocomposites were characterized using cyclic voltammetry (CV). The electrochemical cell was assembled using the composite modified gold electrode as the working electrode. To verify that polymers were formed, the potential was scanned from -0.2V to 0.7V. The presence of characteristic oxidation and reduction peaks in this potential range were used to confirm the formation of both polymers (PANI-COOH and PABA) on the ssDNA/MWNT surface.

#### 4.4.6. Immobilization of FAD and FAD-NH<sub>2</sub> on ssDNA/MWNT/polymer composite modified gold surface

##### 4.4.6.1. Immobilization of FAD on ssDNA/MWNT/PABA

8mM FAD was prepared using 0.1M PBS solution (pH 7.0). The FAD solution was added onto the ssDNA/MWNT/PABA modified gold surface and allowed to react for 2hrs. During this time, the boronic acid moiety on the PABA backbone reacts with the diol moiety of FAD and a boronate ester is formed. After immobilization of FAD, the modified electrode was rinsed with 0.1M PBS solution (pH 7.0) to remove unreacted FAD.

#### 4.4.6.2. Immobilization of FAD-NH<sub>2</sub> on ssDNA/MWNT/PANI-COOH

An EDC/NHS mixture (1 to 2.5 ratio) was added to the ssDNA/MWNT/PANI-COOH modified gold surface and allowed to react for 1hr. During this process, the carboxyl group on the polyaniline backbone becomes activated. A solution of N<sup>6</sup>-(2-Aminoethyl)-FAD (FAD-NH<sub>2</sub>) (prepared as described in reference [32]) in 0.1M PBS (pH 7.0) was added to the EDC/NHS mixture and allowed to react for an additional 2hrs. The activated carboxyl group will covalently link with the primary amine group of the FAD-NH<sub>2</sub>. After immobilization of FAD-NH<sub>2</sub>, the modified electrode was rinsed with 0.1M PBS solution (pH 7.0) to remove unreacted FAD-NH<sub>2</sub>.

#### 4.4.7. Characterization of FAD and FAD-NH<sub>2</sub> modified gold electrodes

The FAD and FAD-NH<sub>2</sub> modified electrodes were characterized using cyclic voltammetry (CV). To verify that FAD was attached to the CNT/polymer composite on the gold electrode, the potential was scanned from -0.8V to 0V. The presence of a characteristic oxidation peak at ~-0.45V indicates the presence of FAD and FAD-NH<sub>2</sub>.

#### 4.4.8. Preparation of apo-glucose oxidase

Apo-glucose oxidase was prepared using a method previously reported by Swoboda [32]. Briefly, saturated ammonium sulfate solution was prepared. The solution was acidified to a pH of 1.4 using concentrated sulfuric acid. 10mg/L of glucose oxidase was slowly added with stirring to 5mL of the acidified ammonium sulfate solution at 4°C. The acidic ammonium sulfate solution causes the FAD cofactor to detach from the glucose oxidase enzyme, making it inactive. The FAD was removed by centrifugation at 15,000 rpm for 15 mins. The precipitate was dissolved and neutralized with sodium acetate (2.5M) and the process was repeated until the supernatant was clear. The final product was dissolved in 0.1M PBS buffer (pH 7.0).

#### 4.4.9. Reconstitution of apo-glucose oxidase

Apo glucose oxidase was added to the FAD modified gold electrode and allowed to react for 5hrs. During this process, the FAD binds back to the apo-glucose oxidase and activates the enzyme again. After immobilization, the enzyme modified electrode was rinsed with 0.1M PBS solution to remove unreacted apo-glucose oxidase.

#### 4.4.10. Glucose oxidation

The electrochemical cell was set up again using the reconstituted apo-glucose oxidase modified gold electrode. Glucose oxidation was monitored using CV measurements and the potential range used was from 0V to 0.7V. 0.1M PBS (pH 7.0) was used as the electrolyte solution. The CV was measured for the different concentrations of glucose added.

#### 4.4.11. Characterization

##### 4.4.11.1. UV-Visible Spectroscopy

All UV spectra were acquired with a Cary 500 UV-Vis-NIR spectrophotometer. The spectra were collected over the range of 200-1100 nm. In preparing the samples for UV-Vis spectral analysis, an aliquot of the solution was taken and diluted in 3 mL of de-ionized water.

##### 4.4.11.2. Atomic Force Microscopy

AFM images were obtained with a tapping mode atomic force microscope (Nanoscope III A, Digital Instruments). Samples were prepared by depositing 5 $\mu$ L of solution onto freshly cleaved mica surface. After incubating for 5 minutes, the mica surface was rinsed with de-ionized water and dried with nitrogen.

#### 4.4.11.3. 4-probe conductance measurements

Percolation-like conductive behaviors of the ssDNA/MWNT composites were studied using a 302 manual four point resistivity probe (Lucas Laboratories). Films with different thickness were prepared by vacuum filtration using an Anodisc 47 Inorganic membranes with a 200nm pore (Whatman Ltd). After filtration, the thin films were dried in vacuum for 15-20 mins prior to sheet conductance measurements.

#### 4.4.11.4. Electrochemical measurements

Cyclic voltammetry and electrochemical impedance measurements were carried out with a CH Instrument 760C series electrochemical station. The electrochemical reactions were performed in a homemade Teflon cell ( $0.25\text{cm}^2$ ) using a typical three-electrode cell system. Modified gold substrate (prepared by depositing 100nm gold on a Si wafer with a 10nm Ti buffer layer) was used as the working electrode, a platinum wire was used as the counter electrode, and a silver wire was used as the reference electrode (silver electrode was calibrated against the standard Ag/AgCl reference electrode). The electrolyte used in the impedance study of FAD immobilization is PBS buffer. Redox probes  $\text{K}_3\text{Fe}(\text{CN})_6$  was added to study the impedance of apo-glucose immobilization.

## 4.5 References

1. Baravik, I., et al., *Electrical Contacting of Redox Enzymes by Means of Oligoaniline-Cross-Linked Enzyme/Carbon Nanotube Composites*. Langmuir, 2009. **25**: p. 13978-13983.
2. Granot, E., et al., *Enhanced bioelectrocatalysis using single-walled carbon nanotubes (SWCNTs)/polyaniline hybrid systems in thin-film and microrod structures associated with electrodes*. Electroanal., 2006. **18**: p. 26-34.
3. Patolsky, F., Y. Weizmann, and I. Willner, *Long-range electrical contacting of redox enzymes by SWCNT connectors*. Angew. Chem. Int. Ed., 2004. **43**: p. 2113-2117.
4. Willner, B., E. Katz, and I. Willner, *Electrical contacting of redox proteins by nanotechnological means*. Curr. Opin. Biotechnol., 2006. **17**: p. 589-596.
5. Willner, I., et al., *Integrated Enzyme-Based Biofuel Cells - A Review*. Fuel Cells, 2009. **9**: p. 7-24.
6. Xiao, Y., et al., *"Plugging into enzymes": Nanowiring of redox enzymes by a gold nanoparticle*. Science, 2003. **299**: p. 1877-1881.
7. Yan, Y.M., et al., *Integrated Electrically Contacted Glucose Oxidase/Carbon Nanotube Electrodes for the Bioelectrocatalyzed Detection of Glucose*. Journal of Physical Chemistry C, 2008. **112**: p. 17883-17888.
8. Yehezkeli, O., et al., *Nano-engineered Flavin-Dependent Glucose Dehydrogenase/Gold Nanoparticle-Modified Electrodes for Glucose Sensing and Biofuel Cell Applications*. ACS Nano, 2011. **5**: p. 2385-2391.
9. Zayats, M., B. Willner, and I. Willner, *Design of amperometric biosensors and biofuel cells by the reconstitution of electrically contacted enzyme electrodes*. Electroanal., 2008. **20**: p. 583-601.
10. Guiseppi-Elie, A., C. Lei, and R.H. Baughman, *Direct electron transfer of glucose oxidase on carbon nanotubes*. Nanotechnol., 2002. **13**: p. 559-564.
11. Liu, Y., et al., *The direct electron transfer of glucose oxidase and glucose biosensor based on carbon nanotubes/chitosan matrix*. Biosens. Bioelectron., 2005. **21**: p. 984-988.
12. Tsai, T.-W., et al., *Adsorption of Glucose Oxidase onto Single-Walled Carbon Nanotubes and Its Application in Layer-By-Layer Biosensors*. Anal. Chem., 2009. **81**: p. 7917-7925.
13. Yan, Y., et al., *Carbon Nanotube Based Glucose/O<sub>2</sub> Biofuel Cells*. Adv. Mater., 2006. **18**: p. 2639-2643.
14. Granot, E., et al., *Enhanced Bioelectrocatalysis Using Au-Nanoparticle/Polyaniline Hybrid systems in Thin Films and Microstructured Rods Assembled on Electrodes*. Chem. Mater., 2005. **17**: p. 4600-4609.



15. Shi, L., Y. Xiao, and I. Willner, *Electrical contacting of glucose oxidase by DNA-templated polyaniline wires on surfaces*. *Electrochem. Commun.*, 2004. **6**: p. 1057-1060.
16. Wang, Z., et al., *Detection of Glucose Based on Direct Electron Transfer Reaction of Glucose Oxidase Immobilized on Highly Ordered Polyaniline Nanotubes*. *Anal. Chem.*, 2009. **81**: p. 1639-1645.
17. Leger, C., et al., *Enzyme Electrokinetics: Using Protein Film Voltammetry to Investigate Redox Enzymes and Their Mechanisms*. *Biochem.*, 2003. **42**: p. 8653-8662.
18. Ma, Y., et al., *Improved Conductivity of Carbon Nanotube Networks by In Situ Polymerization of a Thin Skin of Conducting Polymer*. *ACS Nano*, 2008. **2**: p. 1197-1204.
19. Ma, Y.F., et al., *In-situ Fabrication of A Water-Soluble, Self-Doped Polyaniline Nanocomposite: the Unique Role of DNA Functionalized Single-Walled Carbon Nanotubes*. *J. Am. Chem. Soc.*, 2006. **128**: p. 12064-12065.
20. Springsteen, G. and B. Wang, *A detailed examination of boronic acid-diol complexation*. *Tetrahedron*, 2002. **58**: p. 5291-5300.
21. Bard, A.J. and L.R. Faulkner, *Electrochemical Methods: Fundamentals and Applications*, ed. E. Swain and D. Harris. 2001: Wiley & Sons.
22. Laviron, E., *General expression of the linear potential sweep voltammogram in the case of diffusionless electrochemical systems*. *J. Electroanal. Chem.*, 1979. **101**: p. 19-28.
23. Willner, I., et al., *Electrical Wiring of Glucose Oxidase by Reconstitution of FAD-Modified Monolayers Assembled onto Au-Electrodes*. *J. Am. Chem. Soc.*, 1996. **118**: p. 10321-10322.
24. Bonanos, N., B.C.H. Steele, and E.P. Butler, *Impedance Spectroscopy Theory, Experiment, and Applications*, ed. E. Barsoukov and J.R. Macdonald. 2005: Wiley & Sons.
25. Yuan, X.-Z., et al., *Electrochemical Impedance Spectroscopy in PEM Fuel Cells: Fundamentals and Applications*. 2010: Springer.
26. Willner, I. and E. Katz, *Bioelectronics: From Theory to Applications*. 2005: Wiley-VCH.
27. K'Owino, I.O. and O.A. Sadik, *Impedance Spectroscopy: A Powerful Tool for Rapid Biomolecular Screening and Cell Culture Monitoring*. *Electroanal.*, 2005. **17**: p. 2101-2113.
28. Withey, G.D., et al., *Ultra-high redox enzyme signal transduction using highly ordered carbon nanotube array electrodes*. *Biosens. Bioelectron.*, 2006. **21**: p. 1560-1565.
29. Buckmann, A.F., V. Wray, and A. Stocker, *Synthesis of N6-(2-Aminoethyl)-FAD, N6-(6-Carboxyhexyl)-FAD, and related compounds*. *Methods Enzymol.*, 1997. **280**: p. 360-375.
30. Katz, E. and I. Willner, *A Biofuel Cell with Electrochemically Switchable and Tunable Power Output*. *J. Am. Chem. Soc.*, 2003. **125**: p. 6803-6813.

31. Zheng, M., et al., *DNA-assisted dispersion and separation of carbon nanotubes*. Nat. Mater., 2003. **2**: p. 338-342.
32. Swoboda, B.E.P., *The relationship between molecular conformation and the binding of flavin-adenine dinucleotide in glucose oxidase*. Biochim. Biophys. Acta, 1969. **175**: p. 365-379.

## **Chapter 5**

# **Carbon Nanotube Plasmon: Sensitive and selective detection of Fe (III)**

## **5.1 Introduction**

Iron is an important trace element that is widely found in nature. It is essential for the growth and metabolism of all organisms. Despite its abundance found in the earth's crust (5.6%) [1], dissolved iron is found in extremely low concentrations in many oceans and aquatic systems (0.05-2nM) [2-3]. The availability of iron limits the primary ecological productivity of marine phytoplankton and the associated uptake of carbon dioxide for about 40% of the world's oceans. This would disrupt and have a huge impact on the carbon cycle [2, 4]. Therefore, changes in ocean iron supply may have a significant effect on atmospheric carbon dioxide concentrations and cause global climate change. Water erosion, rainwater and atmospheric dust are some of the important sources of iron that fertilize the oceans [4-7].

Currently, the selective detection of iron in the atmosphere as well as in the oceans is extremely challenging. This is mainly due to its low concentrations and the presence of many other metal ions which can cause interference during the detection process [2]. Furthermore, in situ sampling and measurement of iron is important for ocean ecological studies because it helps maintain sample

integrity, thus providing more accurate data. Therefore, large and vibration-sensitive instruments such as atomic absorption spectroscopy (AAS) and inductively coupled plasma-mass spectroscopy (ICP-MS) are not suitable, despite their high sensitivity and multi-element analyses capability. Consequently, methodologies for iron determination having high sensitivity, selectivity, reliability, and portability are being developed.

Over the past years, different methods for iron determination have been proposed. Some of these methods include adsorptive cathodic stripping voltammetry (AdCSV) [8], flow injection analysis coupled with fluorescence spectroscopy (FIA/F) [9], and online preconcentration coupled with spectrophotometry (OP/S) [10]. In most detection methods, which includes the three mentioned, a tedious approach involving the preconcentration of iron ions is required. In AsCSV, iron is first extracted from the sample by complexation with a binding ligand. This iron-ligand complex is then adsorbed onto the working electrode for stripping analysis. Similarly, in both FIA/F and OP/S, an extraction and preconcentration of iron is necessary. Sayour *et al.* [9] have demonstrated that the use of fluorescent binding ligands can be used to determine iron concentration. Once the iron-ligand complex was formed, fluorescence quenching was observed. Although all these methods are innovative and have fairly high sensitivity, their detection limits are insufficient for determining the low iron concentration in oceans. In addition, extraction and preconcentration of iron in the original sample is required.

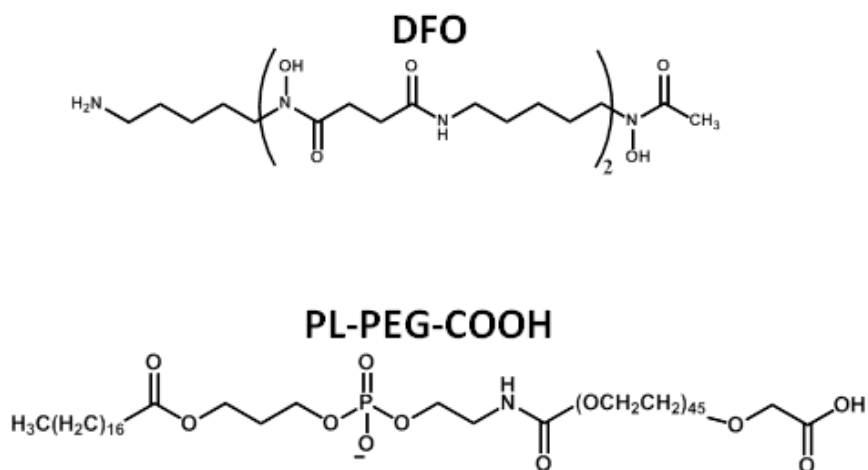
In this chapter of the thesis, **we have developed a highly sensitive and selective method for Fe (III) detection that does not require preconcentration of the sample and can detect iron in the picomolar range.**

This was accomplished by surface modification of the carbon nanotube surface with a selective Fe (III) siderophore. We observed that the plasmon band of SWNT showed high sensitivity upon complex formation with iron. To the best of our knowledge, this is the first case where the plasmon band of SWNTs is used for the detection of iron. Although the data presented are preliminary findings, we envision that it can be used to develop other sensing devices when specific binding chelators are attached to the carbon nanotube surface.

## 5.2 Results and Discussion

### 5.2.1. DFO iron chelator

In response to iron limited environments, certain bacteria and fungi are able to synthesize large amounts of siderophores. Siderophores are low molecular weight molecules with high affinity and specificity for iron. Due to these attractive features, various natural and synthetic siderophores have been used for selective and sensitive detection of Fe (III). One of the most common siderophores is deferoxamine (DFO). It is a natural bacterial siderophore that can form a very stable hexadentate iron chelate complex with a stability constant of about  $10^{31} \text{ M}^{-1}$  [11-12]. The structure of DFO and its complex with iron is shown in Figure 5.1. Note that the DFO siderophore change its conformation upon binding with Fe (III) [13].



**DFO-Fe (III) Complex**

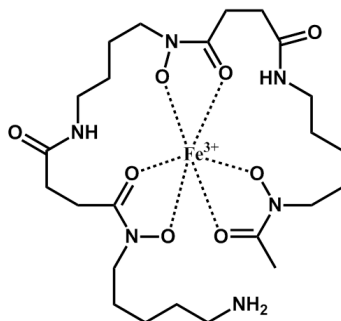


**Figure 5.1:** Structures of DFO, PL-PEG-COOH, and DFO-Fe (III) chelate complex

The binding of DFO to Fe (III) forms a chelate complex with a high molar absorptivity, and thus can be monitored using spectrophotometric techniques [2]. The UV-Vis spectrum (Figure 5.1, red curve) of the chelate complex shows a characteristic peak at ~430nm and is attributed to ligand-to-metal charge transfer (LMCT) [14]. From Figure 5.2, it can clearly be seen that the detection sensitivity for free DFO binding to Fe (III) is low (micromolar range) and an extremely high concentration (300 $\mu$ M) is needed to show a distinct absorption.

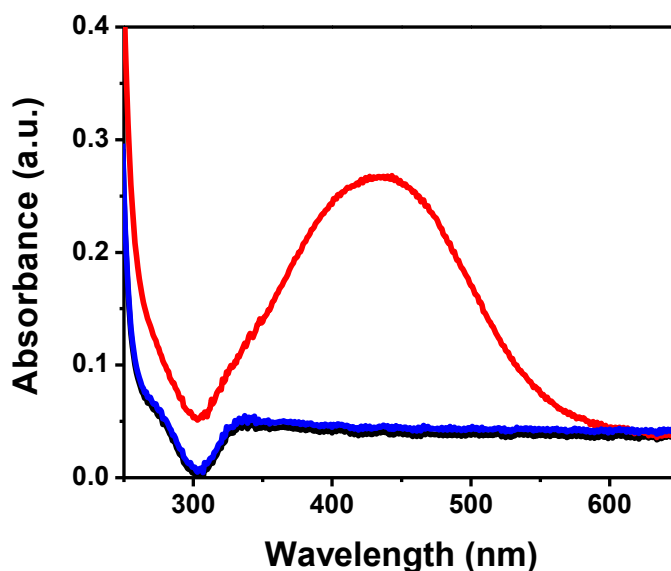


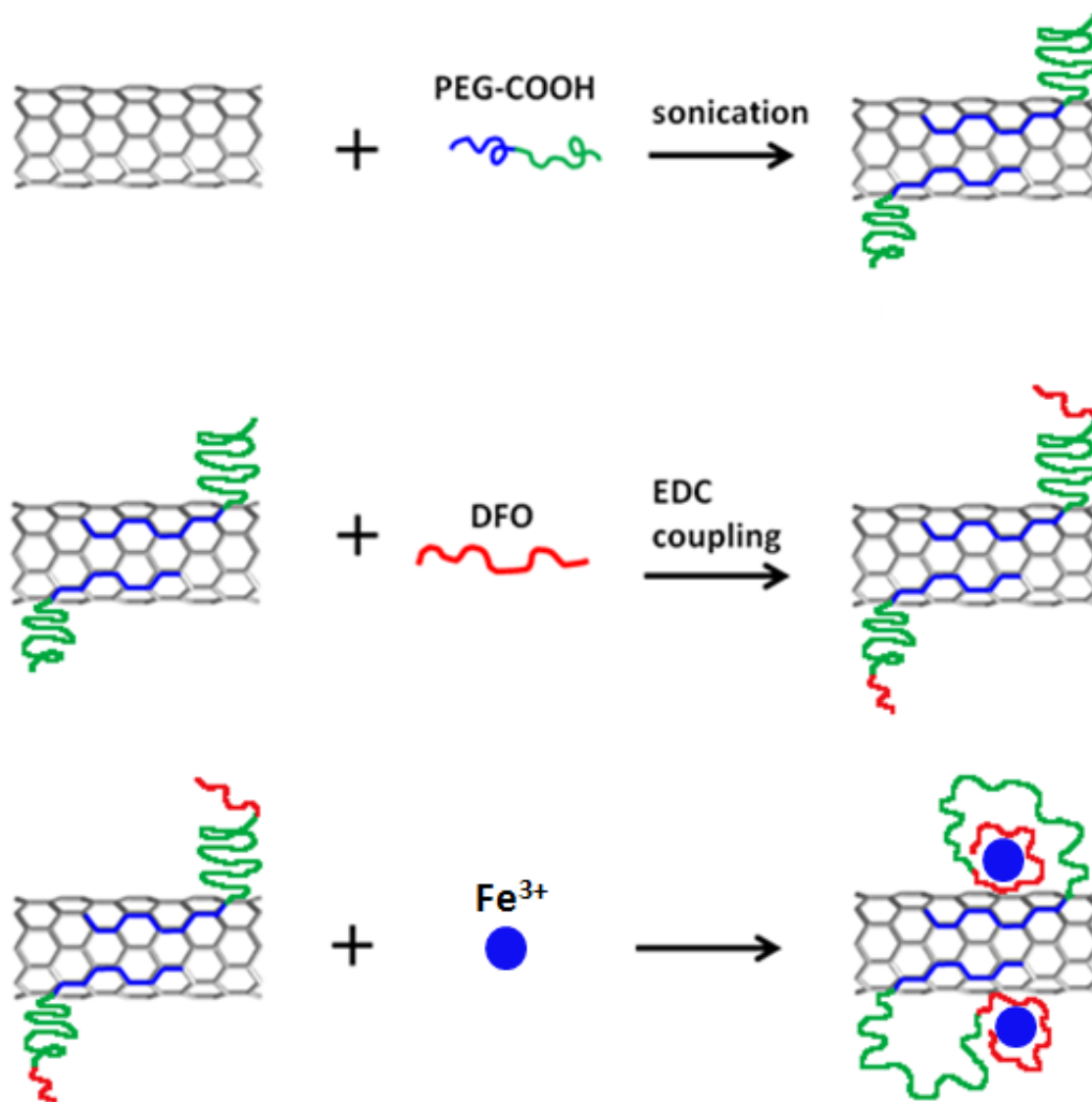
**Figure 5.2:** UV-Visible spectrum showing (black) DFO dissolved in nitric acid, (blue) DFO with 10nM Fe (III) in nitric acid and (red) DFO with 300μM Fe (III) in nitric acid.

### 5.2.2. Preparation of characterization of PL-PEG-COOH/SWNT

To improve the detection limit, we turn our attention to the use of single walled carbon nanotubes (SWNTs). Their unique structure and electronic properties have attracted researchers over the past decade to study and develop SWNT based sensors. Utilizing the high surface area of SWNTs, DFO molecules were attached onto the SWNT surface through surface functionalization. This method is illustrated in scheme 5.1. To preserve the electronic properties of the SWNTs, phospholipid polyethylene glycol with a carboxyl functionality (PL-PEG-COOH) (structure shown in Figure 5.1) were adsorbed onto the SWNT surface



using a method previously proposed by Kam *et al.* [15]. As shown in the scheme, the hydrophobic phospholipid tail is absorbed onto the SWNT surface and the hydrophilic portion is exposed to the aqueous environment.



**Scheme 5.1:** Scheme showing the surface modification of carbon nanotubes for sensitive and selective detection of Fe(III). Pristine SWNTs are first dispersed with PL-PEG-COOH by probe sonication method followed by EDC/NHS coupling with DFO. This method ensures that the electronic properties of the SWNTs are intact and high concentrations of DFO are on the SWNT surface.

The attachment of PL-PEG-COOH to the SWNT surface results in individually dispersed and functionalized SWNTs as seen in the AFM images (Figure 5.3a). From the image, the PL-PEG-COOH/SWNTs were mostly single nanotubes with a few small bundles. The height of the SWNTs was measured to be approximately 1.5nm and the lengths ranged from 50 to 200nm.

The electronic structure of PL-PEG-COOH dispersed SWNTs was also studied using UV-Vis-NIR spectroscopy. Figure 5.3b displays the characteristic spectrum of the PL-PEG-COOH dispersed SWNTs. There are two extremely strong absorptions peaks located at the UV region with absorption maximum at 246 nm and 275 nm, respectively. For the first time ever, we will exploit these two strong absorptions to develop a sensitive and selective approach to detect Fe (III) ions. These two peaks have been observed and studied by several groups; however, their origin is of great interest and is still widely debated [16]. It is known that graphite exhibit two  $\pi$  plasmon bands (collective oscillations of  $\pi$  electrons) in the ultraviolet frequency region, which are originated from the anisotropic optical properties of graphite [17-18]. The imaginary parts of the dielectric function in the direction perpendicular to the c-axis of graphite ( $\text{Im}\{\epsilon_{\perp}\}$ ) has a maximum at 4.5 eV (275.8 nm) and the other in the direction parallel to the c-axis ( $\text{Im}\{-\epsilon_{\parallel}^{-1}\}$ ) is at  $\sim 5.25$  eV (236 nm) [18]. These two peaks are commonly observed in carbon materials such as carbon nanotubes, fullerenes, and amorphous carbon [19-26]. The peak positions may vary depending on the geometries of the carbon nanomaterials, the existence of defects, and the

interaction between the carbon nanomaterials with its environment. The absorption maximum at 275 nm and 246 nm in PL-PEG-COOH/ SWNTs may originate from the maxima in  $I_m\{\epsilon_{\perp}\}$  and  $I_m\{-\epsilon_{\parallel}^{-1}\}$  of the graphite and correspond to orientations parallel and perpendicular to the SWNT axis, respectively.

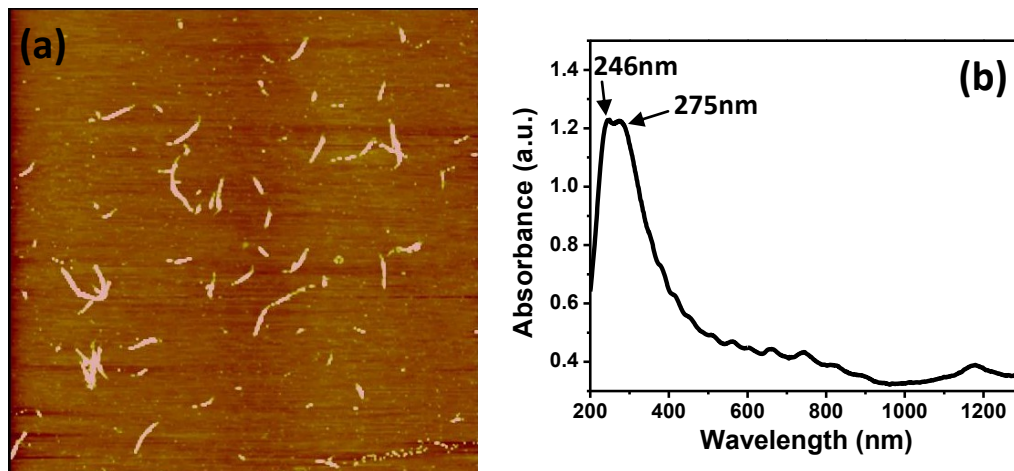


**Figure 5.3:** (a) AFM image of PL-PEG-COOH dispersed SWNT. (b) UV-Vis spectrum of PL-PEG-COOH dispersed SWNT.

Similar to ssDNA/SWNT, the UV-Vis-NIR spectrum of PL-PEG-COOH/SWNT also shows fairly strong van Hove singularities from 400 nm to the NIR region. This part of spectrum is dominated by the absorptions from inter band transitions, which have been the focus of both fundamental and applied studies due to its possible application in various *in vitro* and *in vivo* bioimaging. The first van Hove singularity transition of semiconducting SWNTs ( $sE^{11}$ ) is in the wavelength range of 800 to 1600 nm. Their second van Hove transition ( $sE^{22}$ ) is from 550 to 900 nm, which slightly overlaps with the first transition. The first van

Hove singularity transition for the metallic SWNTs( $mE^{11}$ ) falls in the range of 400 to 600nm. Notice that the van Hove singularities are not extremely prominent as in the case of ss-DNA dispersed SWNTs, indicating that small bundles may exist as confirmed in the AFM image (Figure 5.3a).

Another interesting phenomenon worth mentioning is that this part of spectrum also shows small while obvious background absorption from the SWNTs. This background has been attributed to the non-collinear  $\pi$ -plasmon absorption at  $\sim 5.25$  eV extending into the lower energy region and therefore is an intrinsic optical property of SWNTs originating from the corresponding property of graphite parallel to its c-axis ( $I_m\{-\epsilon_{\parallel}^{-1}\}$ ). So the overall spectrum in this region (from 400 nm to 1200 nm) is a superposition of absorptions due to the various van Hove singularity transitions and the  $\pi$  plasmon backgrounds.

### 5.2.3. Sensitive detection of Fe (III) using PL-PEG-COOH/SWNT/DFO complex

The DFO iron chelator was covalently attached to the individually dispersed PL-PEG-COOH/SWNT by EDC/NHS coupling chemistry. EDC/NHS coupling activates the carboxyl group of PL-PEG-COOH and covalently links it to the amine group of DFO. UV-Vis spectroscopy was then used to detect Fe (III) using the formed PL-PEG-COOH/SWNT/DFO complex. Solutions were prepared in low pH (pH 2) for efficient Fe (III) – DFO binding [27]. Different concentrations

of Fe (III) were added to the PL-PEG-COOH/SWNT/DFO and the UV spectrum was obtained (Figure 5.4). The peak intensity at  $\sim 430\text{nm}$  was absent but surprisingly, the absorption from 246 and 275nm decreased as the concentration of iron was increased. This response is highly sensitive to Fe (III) that even picomolar concentrations of Fe (III) can be detected. Since there was no precipitate formed after the addition of Fe(III), the absorption decrease is most likely not due to the formation of aggregates and most likely a response from the binding interaction between the PL-PEG-COOH/SWNT/DFO with the Fe(III).

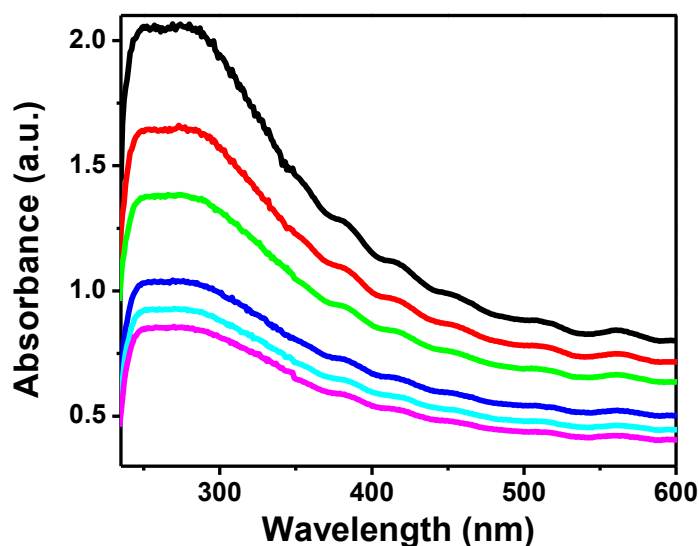


**Figure 5.4:** UV spectrum of PL-PEG-COOH/SWNT/DFO in the presence of (black) 0pM, (red) 10pM, (green) 30pM, (blue) 50pM, (cyan) 70pM, and (magenta) 90pM of Fe (III) standard solution.

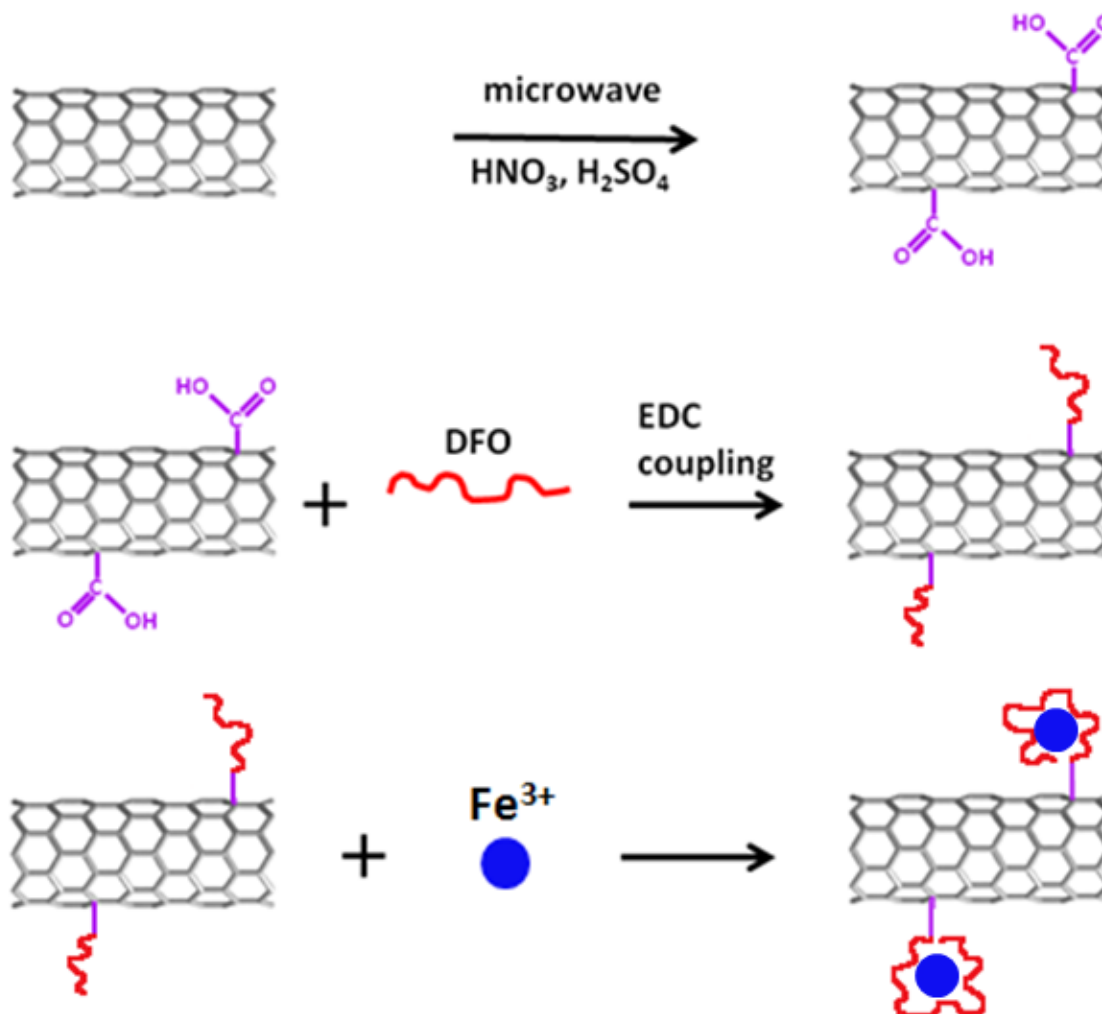
### 5.2.4. Proposed Mechanism

Based on the data, we hypothesize that the decrease in the absorption band centered at ~260-270nm is a result of the interaction between the plasmon band of SWNT and Fe (III) ions. Recently, Choi *et al.* [28] have shown that plasmonic resonance energy transfer (PRET) can occur between highly selective metal–ligand complexes and the plasmon band of gold nanoparticles. It was suggested that PRET can occur when the electronic absorption band of the metal–ligand complex matches the Rayleigh scattering frequency of the gold nanoparticle. In a similar manner, we believe that PRET can occur between SWNTs and DFO-Fe (III) complexes. Although the plasmon band of SWNT does not directly match that of the electronic absorption of DFO-Fe(III) complex, PRET is still possible due to its highly dispersive nature. As stated earlier, the plasmon band of SWNT can be extend to the lower energy regions, which is the main optical backgrounds for the van Hove singularity transitions from 400nm to the NIR range (400 nm-1200nm). Therefore, the mechanism for the detection of Fe (III) using PL-PEG-COOH/SWNT/DFO complex may be due to PRET. In addition, we believe that the PL-PEG-COOH may contribute to the Fe (III) detection sensitivity. The long and flexible PEG chain may be able to bring the DFO-Fe (III) complex closer to the surface, therefore increasing the PRET efficiency and sensitivity as shown in scheme 5.1. In addition, PL-PEG-COOH is noncovalently adsorbed onto the SWNT surface. This preserves the conjugated

structure and electronic properties of the SWNTs, including their strong  $\pi$  plasmon band.

### **5.2.5. Detection of Fe (III) using MF-SWNT/DFO complex**

To investigate if PL-PEG-COOH plays an important role in the sensitive detection of Fe (III), the procedure used in scheme 5.1 was modified. Rather than dispersing SWNT in the presence of PL-PEG-COOH, microwave radiation was used to induce carboxyl groups on the SWNT surface (scheme 5.2). Microwave treatment of SWNT in concentrated acid solution converts the  $sp^2$  hybridized carbon surface to  $sp^3$  hybridized. After the introduction of carboxyl groups to the SWNT surface, EDC/NHS coupling was used to covalently link DFO molecules to the microwave functionalized SWNTs (MF-SWNT).



**Scheme 5.2:** Scheme showing the surface modification of carbon nanotubes for the detection of Fe(III) using microwave radiation approach. Pristine SWNTs are first treated with microwave radiation in concentrated acid. This allows the formation of  $-\text{COOH}$  groups on the surface of the SWNT. Unlike the approach in scheme 1, the surface of the SWNTs is destroyed using microwave radiation. Carboxylation of SWNT was followed by EDC/NHS coupling with DFO.

The detection of Fe (III) with MF-SWNT/DFO is shown in Figure 5.5. The figure shown is different from the one seen previously and this is due to the different baselines used. In the previous spectra, nitric acid solution was used as



the baseline and the decrease in absorption seen remains in the positive region. In this case, the MF-SWNT/DFO complex itself was used as a baseline. The main reason for this is to clearly show that the changes seen in the spectrum after the addition of Fe (III) is directly due to the interaction with iron and nothing else. Similar to Figure 5.4, as the iron concentration is increased, the absorption band at ~260nm decreases. This data suggests that the plasmon band is indeed interacting with Fe (III). However the detection sensitivity is decreased compared to that of PL-PEG-COOH/SWNT/DFO. This helps support the idea that different surface and electronic modification of SWNTs can affect the sensitivity. Furthermore, the electronic structure of PL-PEG-COOH/SWNTs was largely preserved by noncovalent binding between PL-PEG-COOH and SWNTs. The long and flexible PEG chain allows the formed DFO-Fe (III) complex access to the SWNT surface, facilitating PRET. In contrast, although short bonds are formed on the surface of MF-SWNT, they are rigid and prevent the DFO-Fe (III) complex from the surface (scheme 2), reducing PRET efficiency. The other possibility is that covalent functionalization induced by microwave radiation disrupts the plasmon of SWNT and therefore affects its sensitivity for Fe (III).

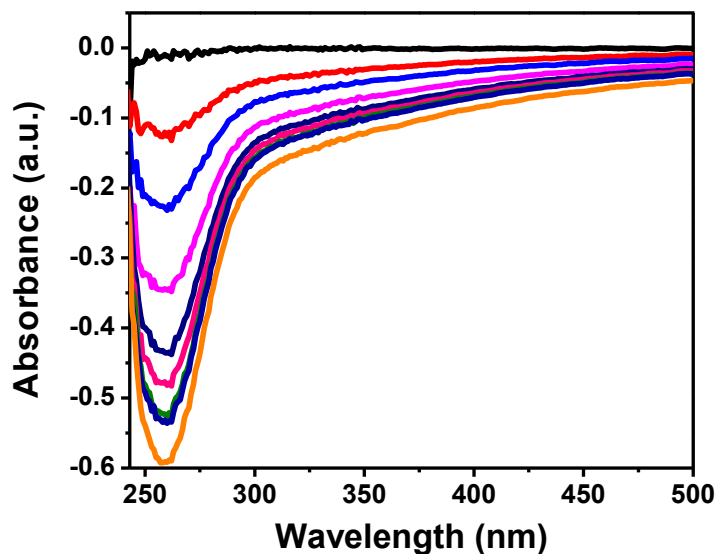


**Figure 5.5:** UV spectrum showing MF-SWNT/DFO in the presence of (black) 0pM  $\text{Fe}^{3+}$ , (red) 120pM  $\text{Fe}^{3+}$ , (blue) 240pM  $\text{Fe}^{3+}$ , (pink) 480pM  $\text{Fe}^{3+}$ , (navy) 720pM  $\text{Fe}^{3+}$ , (magenta) 960pM  $\text{Fe}^{3+}$ , (green) 1.08nM  $\text{Fe}^{3+}$ , (violet) 1.08nM  $\text{Fe}^{3+}$  + mixture, and (orange) 1.20nM  $\text{Fe}^{3+}$ . The mixture contains: 3.3nM  $\text{Fe}^{2+}$ , 3.3nM  $\text{Cu}^{2+}$ , 3.3nM  $\text{Mg}^{2+}$ , 3.3nM  $\text{Pb}^{2+}$ , and 3.3nM  $\text{Ni}^{2+}$ . Baseline used is PL-PEG-COOH/DFO, therefore absorptions are negative.

### 5.2.6. Selective detection of Fe (III)

Metal Ions	Pb2+	Fe3+	Fe2+	Ni2+	Cu2+	Zn2+	Cd2+	Al3+	Ca2+	Mg2+
Stability Constant (log k)	10.5	30.6	7.2	10.9	14.1	10.1	7.9	24.1	2.64	4.1

**Table 5.1:** Stability constants for different DFO-metal ion complex. Values were obtained from [29]

In the previous sections, we have found that surface modification of SWNT with DFO can increase the sensitivity for Fe (III) detection and detection in the picomolar range can be achieved. In this section, the selectivity will be tested. It should be noted that despite the strong binding affinity of DFO to Fe (III), other metal ions such as those listed in Table 1 can also bind to DFO but with a lower binding affinity. The other metal ions can cause interference and lower the sensitivity, which is why extraction and preconcentration of iron is usually necessary in literature [2, 8-10, 30]. In Figure 5.5, the effect of introducing different metal ions is shown for MF-SWNT/DFO. Clearly, different concentrations of Fe (III) cause a decrease in the plasmon band. However, when other ions were added, the absorption intensity remained essentially constant without further decreasing the absorption of the plasmon bands. This suggests that the approach used is highly selective to Fe (III) detection.

The PL-PEG-COOH/SWNT/DFO complex was also tested for its selectivity. In this case, a more systematic approach was studied. Based on Table 5.1, the metal ion with the highest binding constant to DFO, besides Fe (III), is Al (III) ( $\sim 10^{24}$ ). In atmospheric dust, the molar ratio of Al to Fe is  $\sim 3.5$  [31]. Therefore, Al (III) may interfere with the detection of Fe (III), despite having a stability constant that is 6 orders lower. Before testing the interference of Al (III), the binding of Al (III) to DFO was tested. The detection of Al (III) using PL-PEG-COOH/SWNT/DFO is shown in Figure 5.6a. Notice that with increasing concentrations of Al (III) the plasmon absorption intensity also decreases. This

suggests that PL-PEG-COOH/SWNT/DFO can also be used to detect Al(III). Figure 5.6b shows the relative intensity decrease of the plasmon band for both Fe (III) and Al (III) detection. The decrease in the plasmon band for the Al (III) detection is much smaller than that of Fe (III) detection. This can be due to the difference in complex stability between Fe and Al with DFO. Since Fe (III) forms a more stable complex with DFO than Al (III), its interaction with the plasmon band is stronger thus giving a larger decrease in absorption. This also indicates that Al (III) may be able to compete with Fe and cause interference in the detection process.

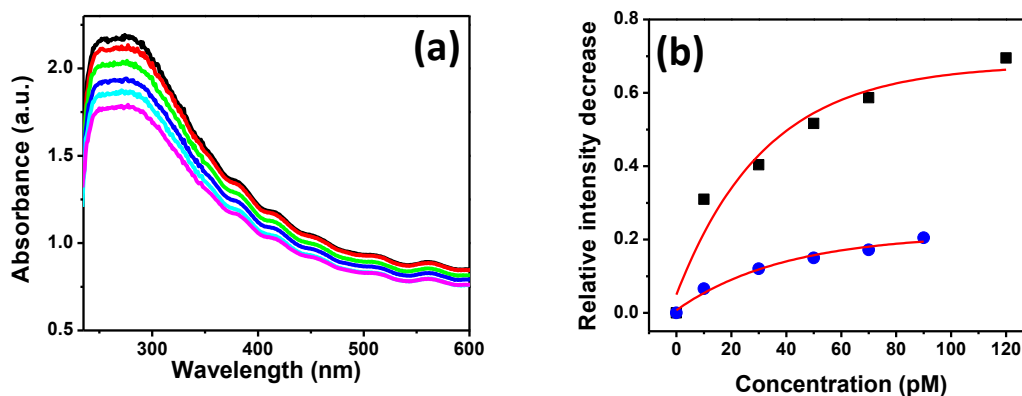


**Figure 5.6:** (a) UV spectrum of PL-PEG-COOH/SWNT/DFO in the presence of (black) 0pM, (red) 10pM, (green) 30pM, (blue) 50pM, (cyan) 70pM, and (magenta) 90pM of aluminum standard solution. (b) Comparison between the relative intensity decrease of (black) Fe(III)-DFO complex and (blue) Al(III)-DFO complex. The red line represents the best fit curve.

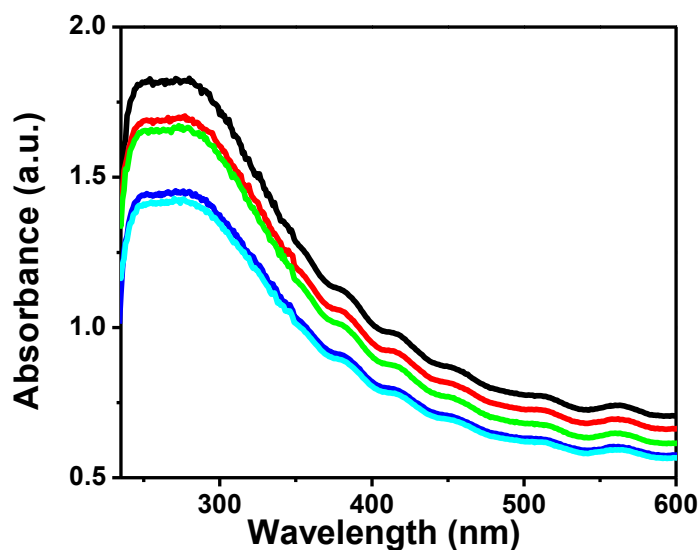


**Figure 5.7:** UV spectrum of PL-PEG-COOH/SWNT/DFO in the presence of (black) 0pM Fe (III), (red) 10pM Fe(III), (green) 100pM Al(III), (blue) 30pM Fe(III), and (cyan) 300pM Al(III) solution

To verify this, both Fe(III) and Al(III) were added to PL-PEG-COOH/SWNT/DFO and the plasmon change was studied (Figure 5.7). Unlike the previous studies where the UV-Vis spectrum was taken after 1 minute reaction with iron, all spectra were taken 20-30secs after reaction with iron. The purpose of this is to study the competitive binding of Fe and Al. As expected, the addition of 10pM of Fe(III) causes the absorption band at ~260-270nm to decrease. This was followed by the addition of 100pM of Al(III), which will compete with unbound Fe (III) in solution. Due to the higher binding affinity of Fe (III) to DFO, the absorption remains relatively unchanged. This process was repeated again with an addition of 30pM of Fe(III) followed by 300pM of Al(III). Once again, the

absorption intensity decreases upon addition of Fe(III) but changes only slightly with high concentrations of Al(III). This helps confirm that the plasmon absorption intensity decrease seen is mainly due to Fe (III) and interference from Al (III) is minimal.

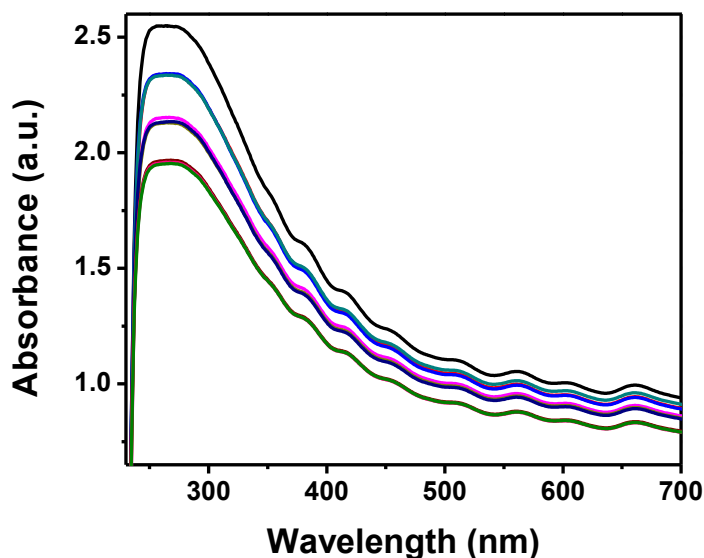


**Figure 5.8:** UV spectrum of PL-PEG-COOH/SWNT/DFO in the presence of (black) 0pM  $\text{Fe}^{3+}$ , (red) 10pM  $\text{Fe}^{3+}$ , (blue) 10uM  $\text{Ca}^{2+}$ , (dark blue) 10uM  $\text{Mg}^{2+}$ , (pink) 30pM  $\text{Fe}^{3+}$ , (olive) 10nM  $\text{Cu}^{2+}$ , (violet) 10nM  $\text{Zn}^{2+}$ , (brown) 50pM  $\text{Fe}^{3+}$ , (magenta) 10nM  $\text{Cd}^{2+}$ , (green) 10nM  $\text{Pb}^{2+}$

It should also be noted that despite the high affinity of DFO for Fe (III), it can also bind to other ions such as Cu (II), Zn (II), Ni (II), as well as other ions listed in Table 1 to form complex structures [32]. Besides Al (III), the interference from other ions was also tested and is shown in Figure 5.8. Similarly, only the addition of Fe (III) showed noticeable decrease in absorption. All other metal ions show relatively no response even with fairly high concentrations.

### 5.2.7. Fe (III) detection of natural rainwater

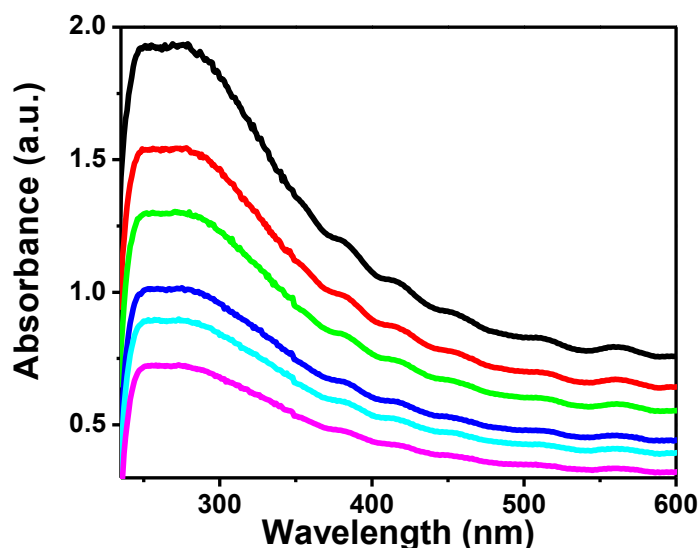


**Figure 5.9:** UV spectrum of PL-PEG-COOH/SWNT/DFO in the presence of (black) 0pM, (red) 10pM, (green) 30pM, (blue) 50pM, (cyan) 70pM, and (magenta) 90pM of Fe (III) rain water.

In order to determine the feasibility of this iron detection approach for practical applications, we attempted to detect the iron concentration in collected rainwater. The concentrations of all ions present in the collected rain water were determined using atomic absorption spectroscopy (AAS) (data was provided by Prof. Yuan Gao from the Department of Environmental Science, Rutgers Newark). The rain water was diluted accordingly to obtain the concentrations used for the detection of Fe standard solution shown in Figure 5.4. The detection of iron at different concentrations is shown in Figure 5.9. As expected, the plasmon absorption band decreased with increasing concentrations of iron. More

interestingly, the absorption decrease for each Fe(III) addition is comparable to that of the Fe standard case, indicating that this method is highly reproducible.

## 5.3 Conclusion

In summary, the novel Fe detection approach presented here is highly selective, highly sensitive, and does not require preconcentration of the original sample. This allows for in-situ sampling without disturbing the sample itself. The sensitive detection of iron was accomplished by utilizing the plasmon band of SWNT. Although the data presented are preliminary findings, we envision that it can be used to develop other sensing devices when specific binding chelators are attached to the carbon nanotube surface.



## 5.4 Experimental

### 5.4.1. Reagents

*N*-Hydroxysulfosuccinimide sodium salt (NHS), *N*-(3-Dimethylaminopropyl)-*N*'-ethylcarbodiimide hydrochloride (EDC), Deferoxamine mesylate salt (DFO), MES hydrate buffer, iron standard solution, and aluminum standard solution were purchased from Aldrich and used as received without further purification. Calcium chloride dihydrate and nickelous chloride 6 hydrate were purchased from J.T. Baker and used as received. Zinc chloride, copper reference standard solution, cadmium reference standard solution, and lead reference standard solution were purchased from Fisher and used as received. Magnesium chloride hexahydrate was purchased from EM science Merck kGaA and used as received. Rain water sample was obtained from Prof. Yuan Gao from the Department of Environmental Science, Rutgers Newark. Highly purified single-walled carbon nanotubes (SWNTs) were prepared by the HiPCO process and obtained from Carbon Nanotechnologies. 1,2-distearoyl-*sn*-glycero-3-phosphoethanolamine-*N*-[carboxy(polyethylene glycol)-2000] (ammonium salt) (PL-PEG-COOH) was purchased from Avanti Polar Lipids Inc. All solutions were prepared using deionized water (18.2 M) (Nanopore water, Barnstead).

### 5.4.2. Dispersion of CNTs into aqueous solution

SWNTs were dispersed into aqueous solution using a method previously described by Kam *et al.* [15]. Briefly, single walled carbon nanotubes were suspended in an aqueous solution containing PL-PEG-COOH. The mixture was sonicated using a Sonics Vibracell (Model VCX 130) for 90 minutes. The sonication process was performed in an ice-water bath to prevent local heating of the CNT which may cause unnecessary scission of CNT. After sonication, the sample was centrifuged using a Beckman J2-21 centrifuge (Eppendorf 5415C) at 6000rpm to remove insoluble materials, leaving PL-PEG-COOH dispersed single walled carbon nanotubes (PL-PEG-COOH/SWNT). The PL-PEG-COOH/SWNT solution was dialyzed using an Amicon Ultra-15 centrifugal filter (Millipore) with 0.1M MES buffer to adjust its pH to 4.5 prior to EDC coupling. The resulting solution consists of highly dispersed and functionalized PL-PEG-COOH/SWNT with a mass concentration of 200-400mg/L. The electronic structure of the dispersed PL-PEG-COOH/SWNT was characterized using UV-Visible spectroscopy.

### 5.4.3. Preparation of microwave-assisted functionalization (carboxylation) of carbon nanotubes.

The highly purified SWNTs were processed into water using a method previously described by Wang *et al.* [33]. In a typical reaction, the as-received SWNTs were added into a 1:1 mixture of 70% nitric acid and 97% sulfuric acid aqueous solution. The mixture was then placed in a CEM “Discover” microwave reactor and subjected to microwave radiation for 1 min. The resulting mixture was washed, filtered through a 0.2 $\mu$ m pore size filter (Whatman Anodisc), and redispersed into deionized water. The resulting solution consists of highly dispersed and microwaved functionalized SWNT (MF-SWNT) with a mass concentration of 200-300mg/L. The electronic structure of the dispersed MF-SWNT was characterized using UV-Visible spectroscopy.

### 5.4.4. Characterization of Fe-free carbon nanotube solution

To ensure that the PL-PEG-COOH/SWNTs and the MF-SWNTs used were free of Fe catalysts, DFO was added into an aliquot of carbon nanotube water solution and mixed. The mixture was then left to react for 2hrs and dialyzed to remove free DFO. The UV-Vis spectrum of the filtrated solution (which contains no carbon nanotubes) was used to monitor the absorption band at 430 nm, which

is attributed to binding between DFO and iron (III). The above process was repeated several times until the absorption at 430 nm disappeared.

#### 5.4.5. Preparation of PL-PEG-COOH/SWNT/DFO and MF-SWNT/DFO complexes

PL-PEG-COOH/SWNT/DFO and MF-SWNT/DFO complexes were prepared by EDC/NHS mediated coupling. Briefly, PL-PEG-COOH/SWNT and MF-SWNT with a concentration between 200mg/L to 250mg/L was mixed with NHS and EDC (2.5 to 1 ratio) in 0.1M MES buffer (pH 4.5). The reaction was allowed to proceed for 1 hour. Upon activation of the carboxyl group, the amide bond was formed by adding DFO to the mixture and allowing it to react for 2 hours. The resulting mixture was subjected to extensive centrifugation and dialysis to remove free DFO, NHS, EDC, and unreacted SWNTs.

#### 5.4.6. Characterization of PL-PEG-COOH/SWNT/DFO and MF-SWNT/DFO complexes.

The PL-PEG-COOH/SWNT/DFO and MF-SWNT/DFO were characterized using a tapping mode Nanoscope IIIa atomic force microscope (AFM) (Veeco instrument) in air. AFM samples were prepared by dropcasting diluted DFO complexed SWNT solution onto cleaned mica surfaces. The samples were

incubated for 3-5 minutes, rinsed with deionized water, and dried in vacuum prior to AFM measurements.

#### 5.4.7. Iron detection in PL-PEG-COOH/SWNT/DFO and MF-SWNT/DFO complexes.

The detection of Fe was monitored using a Cary 500 UV-Vis-NIR spectrophotometer. In preparing the sample for UV-Vis-NIR analysis, an aliquot of PL-PEG-COOH/SWNT/DFO or MF-SWNT/DFO was diluted in nitric acid (pH 2). The UV-Vis-NIR spectrum was acquired after the addition of various concentrations of Fe in nitric acid. The samples were allowed to react with iron for 1 minute before the spectra were obtained.

### 5.4.8. Characterization

#### 5.4.8.1 Ultraviolet-Visible-Near Infrared Spectroscopy

Spectra were acquired with a Cary 500 UV-Vis-NIR spectrophotometer. The spectra were collected over the range of 200-800 nm. In preparing the samples for UV-Vis spectral analysis, PL-PEG-COOH/SWNT/DFO or MF-SWNT/DFO was diluted to 3mL with pH 2 nitric acid.

#### 5.4.8.2 Atomic Force Microscopy

AFM images were obtained with a tapping mode atomic force microscope (Nanoscope III A, Digital Instruments). Samples were prepared by depositing 5 $\mu$ L of solution onto freshly cleaved mica surface. After incubating for 5 minutes, the mica surface was rinsed with de-ionized water and dried with nitrogen.

## 5.5 References

1. Taylor, S.R., *Abundance of chemical elements in the continental crust: a new table*. Geochim. Cosmochim. Acta, 1964. **28**: p. 1273-1285.
2. Achterberg, E.P., et al., *Determination of iron in seawater*. Anal. Chim. Acta, 2001. **442**: p. 1-14.
3. Archer, D.E., *A Model of the iron cycle in the ocean*. Global Biogeochem. Cycles, 2000. **14**: p. 269-279.
4. Boyd, P.W., *Biogeochemistry: Iron findings*. Nature, 2007. **446**: p. 989-991.
5. Gao, Y., et al., *Seasonal Distributions of Aeolian Iron Fluxes to the Global Ocean*. Geophys. Res. Lett., 2001. **28**: p. 29-32.
6. Gao, Y., S.-M. Fan, and J.L. Sarmiento, *Aeolian Iron Input to the Ocean through Precipitation Scavenging: A Modeling Perspective and Its Implication for Natural Iron Fertilization in the Ocean*. J. Geophys. Res., 2003. **108**.
7. Briat, J.F., *Iron assimilation and storage in prokaryotes*. J. Gen. Microbiol., 1992. **138**: p. 2475-2483.
8. Croot, P.L. and M. Johansson, *Determination of Iron Speciation by Cathodic Stripping Voltammetry in Seawater Using the Competing Ligand 2-(2-Thiazolylazo)-p-cresol (TAC)*. Electroanal., 2000. **12**: p. 565-576.
9. Sayour, H.E.M., T.M.A. Razek, and K.F. Fadel, *Flow Injection Spectrofluorimetric Determination of Iron in Industrial Effluents based on Fluorescence Quenching of 1-Naphthol-2-Sulfonate*. J. Fluoresc., 2011. **21**: p. 1385-1391.
10. Blain, S. and P. Treguer, *Iron (II) and iron(III) determination in sea water at the nanomolar level with selective on-line preconcentration and spectrophotometric determination*. Anal. Chim. Acta, 1995. **308**: p. 425-432.
11. Porter, J.B., *Concepts and goals in the management of transfusional iron overload*. Am. J. Hematol., 2007. **82**: p. 1136-1139.
12. Crumbliss, B.H., *Chemical aspects of siderophore mediated iron transport*. Biometals, 2002. **15**: p. 325-339.
13. Kraemer, S.M., *Iron Oxide Dissolution and Solubility in the Presence of Siderophores*. Aquat. Sci., 2004. **66**: p. 3-18.
14. Monzyk, B. and A.L. Crumbliss, *Kinetics and mechanism of the stepwise dissociation of iron (III) from ferrioxamine B in aqueous acid*. J. Am. Chem. Soc., 1982. **104**: p. 4921-4929.
15. Kam, N.W.S., et al., *Carbon nanotubes as multifunctional biological transporters and near-infrared agents for selective cancer cell destruction*. Proc. Natl. Acad. Sci., 2005. **102**: p. 11600-11605.
16. Itkis, M.E., et al., *Purity Evaluation of As-Prepared Single-Walled Carbon Nanotube Soot by Use of Solution-Phase Near-IR Spectroscopy*. Nano Lett., 2003. **3**: p. 309-314.

17. Taft, E.A. and H.R. Philipp, *Optical Properties of Graphite*. Phys. Rev., 1965. **138**: p. A197-202.
18. Marinopoulos, A.G., et al., *Anisotropy and interplane interactions in the dielectric response of graphite*. Phys. Rev. Lett., 2002. **89**.
19. Marinopoulos, A.G., et al., *Optical absorption and electron energy loss spectra of carbon and boron nitride nanotubes: a first-principles approach*. Appl. Phys. A - Mater. Sci. & Proc., 2004. **78**: p. 1157-1167.
20. Marinopoulos, A.G., et al., *Optical and loss spectra of carbon nanotubes: Depolarization effects and intertube interactions*. Phys. Rev. Lett., 2003. **90**: p. 46402 - 46404.
21. Marinopoulos, A.G., et al., *Ab initio study of the optical absorption and wave-vector-dependent dielectric response of graphite*. Phys. Rev. B, 2004. **69**.
22. Kramberger, C., et al., *Linear plasmon dispersion in single-wall carbon nanotubes and the collective excitation spectrum of graphene*. Phys. Rev. Lett., 2008. **100**.
23. Yoo, S., et al., *Optical anisotropy in single-walled carbon nanotubes*. Opt. Lett., 2005. **30**: p. 3201-3203.
24. Murakami, Y., et al., *Polarization dependence of the optical absorption of single-walled carbon nanotubes*. Phys. Rev. Lett., 2005. **94**.
25. Murakami, Y., et al., *Polarization dependent optical absorption properties of single-walled carbon nanotubes and methodology for the evaluation of their morphology*. Carbon, 2005. **43**: p. 2664-2676.
26. Kelly, M.K., *Optical Transitions of C60 Films in the Visible and Ultraviolet from spectroscopic ellipsometry*. Phys. Rev. B, 1992. **46**: p. 4963-4968.
27. Ihnat, P.M., J.L. Vennerstrom, and D.H. Robinson, *Solution equilibria of deferoxamine amides*. J Pharm Sci, 2002. **7**: p. 1733-1741.
28. Choi, Y., et al., *Selective and sensitive detection of metal ions by plasmonic resonance energy transfer-based nanospectroscopy*. Nat. Nanotech., 2009. **4**: p. 742-746.
29. Kiss, T. and E. Farkas, *Metal-binding Ability of Desferrioxamine B*. J. Inclusion Phenomena and Molecular Recognition in Chemistry, 1998. **32**: p. 385-403.
30. Giokas, D.L., E.K. Paleologos, and M.I. Karayannis, *Speciation of Fe(II) and Fe(III) by the modified ferrozine method, FIA-spectrophotometry, and flame AAS after cloud-point extraction*. Anal. Bioanal. Chem., 2001. **373**: p. 273-243.
31. Tria, J., et al., *Determination of Aluminium in Natural Water Samples*. Anal. Chim. Acta, 2007. **588**: p. 153-165.
32. Farkas, E., et al., *Copper (II), Nickel (II), Zinc (II) and Molybdenum (VI) Complexes of Desferrioxamine B in Aqueous Solution*. J. Inorg. Biochem., 1997: p. 281-286.
33. Wang, Y., Z. Iqbal, and S. Mitra, *Microwave-induced rapid chemical functionalization of single-walled carbon nanotubes*. Carbon, 2005. **43**: p. 1015-1020.



## **Chapter 6**

# **Enhanced Selective Detection and Destruction of Cancer Cells via a Noncovalent Functionalization Approach**

## **6.1 Introduction**

Cancer remains as the second leading cause of death in the United States even though significant progress has been made in both understanding and treatment of cancer during the last thirty years. Non-invasive detection of primary cancers at their earliest stages combined with improved therapeutic protocols could significantly increase the survival rate of patients. Due to their unique optical properties, SWNTs are attractive for early cancer detection and therapy. In particular, SWNTs absorb strongly in the near-infrared (NIR) region due to their electronic transitions between the first and second van Hove singularities [1-2]. SWNTs exhibit strong, stable, and unique Raman scattering and they also emit fluorescence in the NIR spectral window, showing great potential for sensitive detection of cancer cells or markers [3]. Continuous NIR irradiation of SWNTs attached to cancer cells produces excessive heat in the local environment that can be utilized to achieve selective destruction of these cells without harming normal ones [4]. In an effort to improve breast cancer detection and therapy, we have developed a novel method which combines the

advantages of anti-HER2 IgY antibody with the unique properties of SWNTs. We constructed a HER2 IgY-SWNT complex by directly conjugating the anti-HER2 IgY antibody to microwave functionalized SWNTs via covalent bonding. The Raman and NIR optical properties of the complex were explored and its feasibility for detection and selective destruction of cancer cells was tested [5]. We found, however, that the SWNT Raman signal from the G band was relatively low compared to the Raman background from the cancer cells.

To increase detection sensitivity, an extensive literature survey was performed and it was found that the Raman intensity of pristine CNTs can be decreased by a factor of 4 upon oxidation of its sp<sup>2</sup> hybridized surface [6]. Results from a theoretical study by Irle *et al.* [7] also showed large reduction in peak intensities in the calculated Raman spectra, which was attributed to the loss of cylindrical symmetry after introducing oxygen containing groups upon oxidation. In addition, it is known that the Raman signal can be dramatically increased when the incident or scattered photons are in resonance with an optically allowed electronic transition, also known as the Resonance Raman Effect. Due to strong electron–phonon coupling, the cross-section of individual CNTs under resonant conditions has been estimated to be  $\sim 10^{-21} \text{ cm}^2 \text{ sr}^{-1} \text{ molecule}^{-1}$  [8], which is four magnitudes larger than small aromatic ring systems under resonance (typically  $10^{-25} \text{ cm}^2 \text{ sr}^{-1} \text{ molecule}^{-1}$ ) [9]. The changes in the electronic structures of SWNTs arising from covalent modification have been probed by optical absorption spectroscopy [10]. It was shown that chemical

oxidation or molecular modification causes the optical intensity to decrease. Therefore the dramatic decrease in intensity of the Raman bands is possibly due to the reduced optical absorption intensity of the chemically modified tubes.

It was known that the conjugated structures of carbon nanotubes dispersed by microwave irradiation is largely disrupted by covalent modification [11]. Consequently, the exceptional low Raman signal from the IgY HER2 antibody/SWNT complex we constructed earlier is due to the loss of cylindrical symmetry and the lack of resonance due to largely deteriorated optical absorption. In this chapter, we will retain the intrinsic electronic structure and properties of SWNT by directly dispersing highly purified SWNTs with a COOH terminated phospholipid–polyethylene glycol (PL–PEG). The phospholipid will bind to the nanotube surface via hydrophobic interactions. The PEG chain imparts SWNTs water solubility, biocompatibility, and stability against aggregation in serum. We chemically conjugate the IgY HER2 antibody to the distal end of the PEG chain at the carboxyl group. Our preliminary studies demonstrated that the resultant IgY-SWNT complex display improved optoelectronic properties for its application in the detection and selective destruction of breast cancer cells.

## 6.2 Results and Discussion

### 6.2.1. Functionalization effects on the electronic structure of SWNT

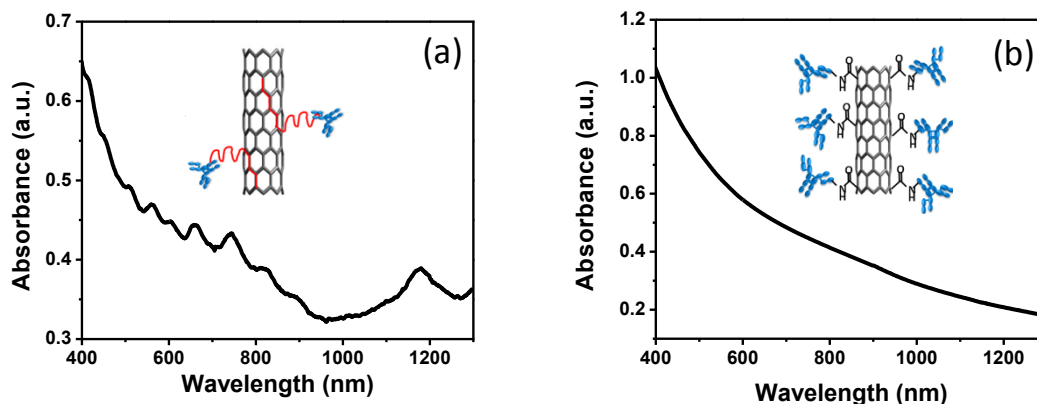


**Figure 6.1:** UV-Vis-NIR spectrum of (a) PL-PEG-COOH/SWNT and (b) MF-SWNT

The UV-Vis-NIR spectra for the covalent functionalization of SWNT and the noncovalent functionalization of SWNT are shown in Figure 6.1. There is a clear difference between these two spectra in the Visible-NIR region. The van-Hove singularities can be seen in the SWNT dispersed with PL-PEG-COOH but not for microwave treated SWNTs. The noncovalent functionalization of SWNT preserves its electronic structure. In contrast, covalent functionalization of SWNT causes a disruption in the electronic structure [12] as  $sp^2$  hybridized carbons on the SWNT surface are changed to  $sp^3$ . As seen in the UV spectrum (Figure

6.1b), covalent functionalization causes the loss of the distinctive features normally seen for individual SWNTs.

### 6.2.2. Effect of surface modification of SWNT on Raman

The Raman spectrum of both MF-SWNT and PL-PEG-COOH/SWNT is shown in Figure 6.2. In both cases, characteristic bands at  $\sim 200\text{-}300\text{cm}^{-1}$  attributed to the radial breathing mode,  $\sim 1300\text{cm}^{-1}$  attributed to the defects on the nanotube, and  $\sim 1600\text{cm}^{-1}$  attributed to the tangential mode corresponding to the stretching along the SWNT surface are seen. The Raman spectrum for both covalent and noncovalent functionalized SWNT also shows a large difference. The G band intensity for the PL-PEG-COOH/SWNT (noncovalent) is much stronger than that of MF-SWNT (covalent) at the same SWNT concentration. This suggests that the electronic structures of SWNTs via noncovalent functionalization were largely preserved during functionalization and thus a strong Raman intensity is seen. Covalent functionalization of SWNT, however, disrupts the electronic structure of SWNT which in turn disrupts the resonance Raman Effect causing the intensity of G band to decrease. Another difference seen in the Raman spectrum is the D band. The D band for MF-SWNT is much higher than that of PL-PEG-COOH/SWNT. Since the D band is usually representative of the defects on the nanotubes, this confirms that the covalent functionalization of SWNT not only disrupts the electronic structure but also creates more defects.

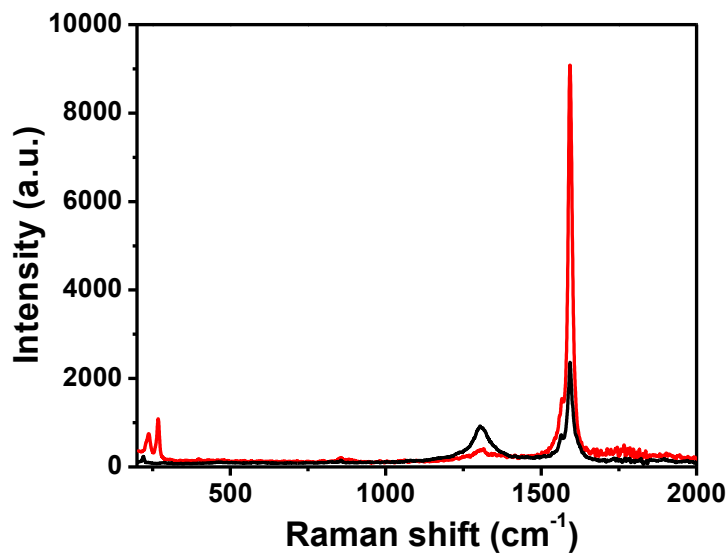


**Figure 6.2:** Raman spectrum of (red) PL-PEG-COOH/SWNT and (black) MF-SWNT

Based on the data and discussion above, we believe that the noncovalent functionalization of SWNT antibodies can enhance the Raman signal of the G band and subsequently be used for the detection of cancer cells.

Previously we have modified the surface of the carbon nanotubes by microwave radiation. This introduced carboxyl groups to the CNT surface and EDC/NHS coupling was used to conjugate the antibodies through its amine groups. SKBR3 and MCF7 cells were treated with the anti-HER2 IgY antibody functionalized SWNT (anti-HER2/SWNT) complex and the Raman spectrum was obtained (Figure 6.3). As shown, the Raman signals of the two cell lines are

extremely large and spans from  $1000\text{cm}^{-1}$  to  $2000\text{cm}^{-1}$ . Furthermore, the Raman spectra of receptor negative MCF7 cell line, untreated SKBR3, and SKBR3 treated MF-SWNT (antibody-free) were all similar. The only spectrum that showed a difference in the Raman is the SKBR3 cell line treated with the anti-HER2/MF-SWNT complex. From the figure, a small peak at  $\sim 1590\text{cm}^{-1}$  is seen and is attributed to the G band of SWNTs. This shows the high selectivity of the anti-HER2/MF-SWNT complex for SKBR3 cell lines. Although the G band of the SWNT can be seen in Figure 6.3, its signal is almost completely covered by the Raman backgrounds from the cancer cell lines.

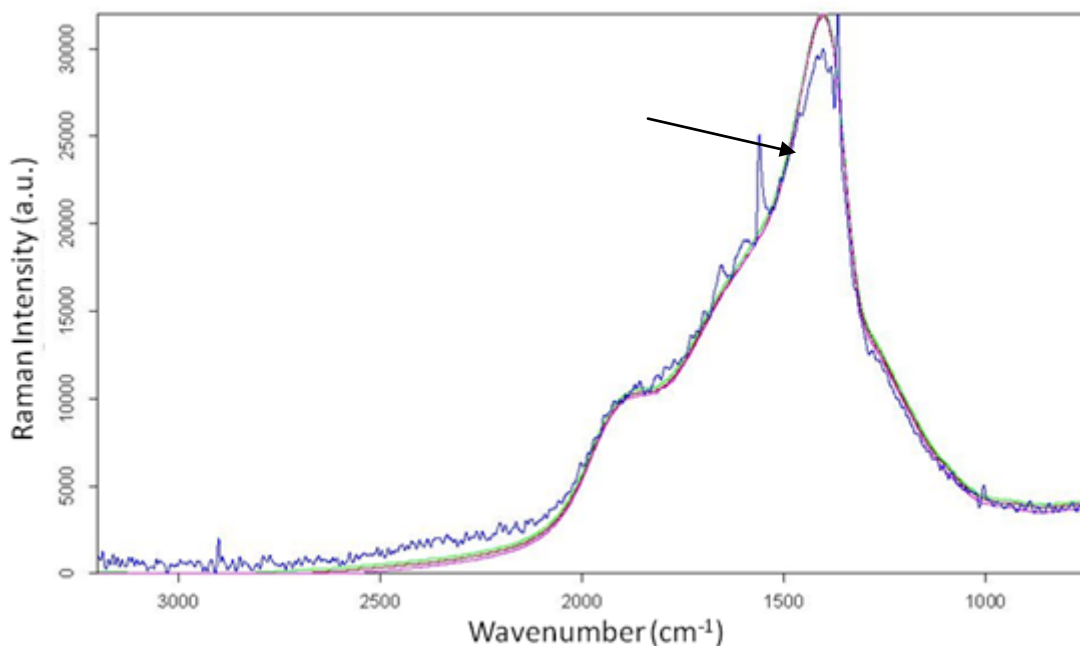
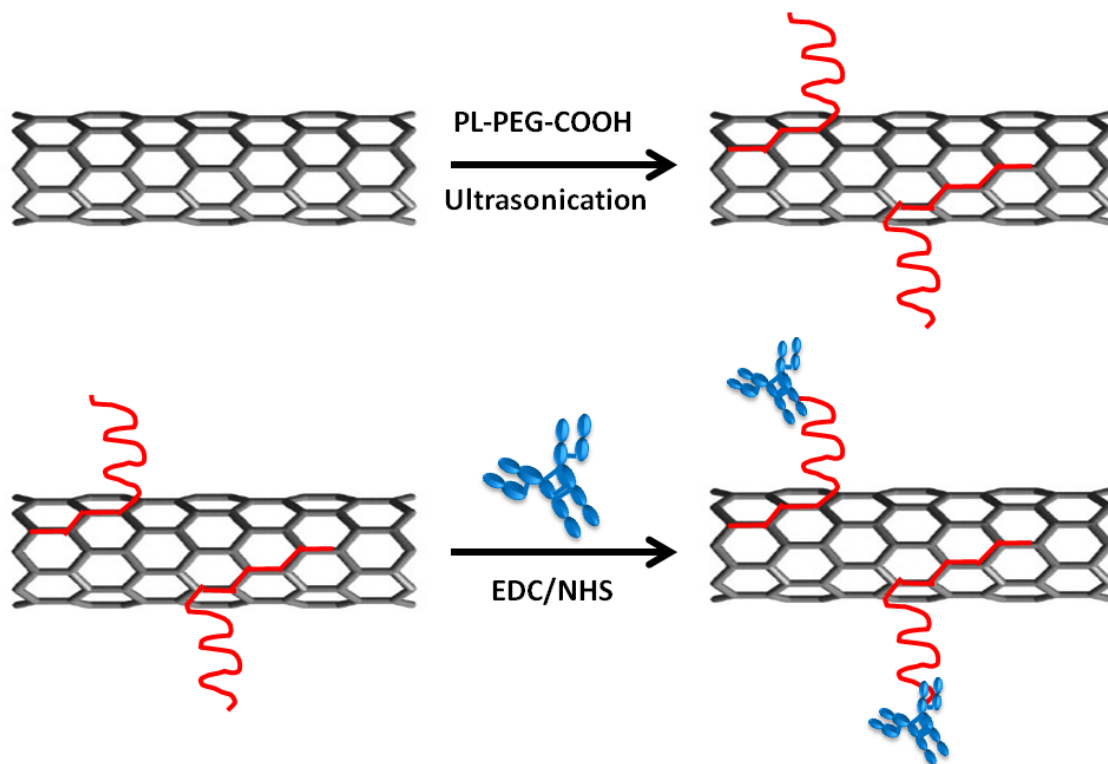


**Figure 6.3:** Raman spectra of (blue) SKBR3 cell line treated with antibody/SWNT complex, (brown) SKBR3 cell line treated with PL-PEG-COOH/SWNT, (magenta) untreated SKBR3 cell line, and (brown) MCF7 cell line treated with antibody/SWNT complex. Image was obtained from [5] for comparison purposes

### 6.2.3. Raman intensity of anti-HER2/PEG-SWNT



**Scheme 6.1:** schematic approach for the noncovalent functionalization of SWNT and anti-HER2 IgY antibody.

Scheme 6.1 shows the approach used to noncovalently functionalize SWNT and the antibodies. The noncovalent functionalization of SWNT with PL-PEG-COOH is described in the previous chapter. The attachment of antibodies to the SWNT was achieved by EDC/NHS coupling. EDC/NHS was used to activate the carboxyl group of the PL-PEG-COOH for 1hr in MEF buffer with a pH of 4.5. After activation of the carboxyl group, the pH of the solution must be changed to 6.3 to facilitate antibody binding to the PL-PEG-COOH/SWNT.



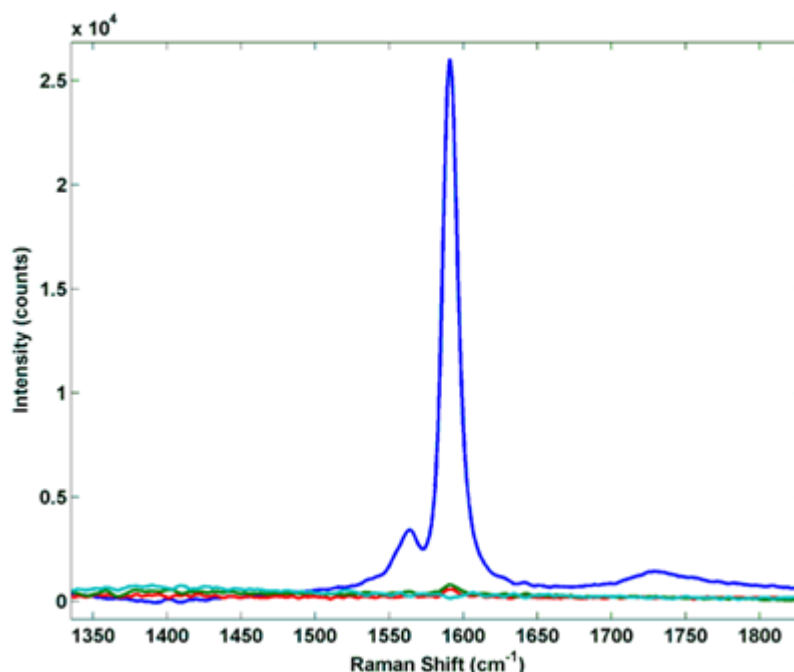


**Figure 6.4:** Raman spectra of (blue) SKBR3 cells treated with anti-HER2/PEG-SWNT, (red) MCF7 cells treated with anti-HER2/PEG-SWNT, (green) SKBR3 cells treated with PL-PEG-COOH/SWNTs only without conjugation of the anti-HER2, and (cyan) untreated SKBR3 cells

The Raman spectra of HER2 specific cancer cells (SKBR3) and HER2 negative cancer cells (MCF7) treated with anti-HER2/PEG-SWNT are shown in Figure 6.4. For comparison, the Raman spectra of SKBR3 cells without any treatment and treated with only PL-PEG-COOH/SWNT (no antibody) are also shown in Figure 6.4. The untreated SKBR3 cancer cell line show no SWNT Raman signal from SWNTs, as expected. The Raman spectra of receptor negative MCF7 cell line treated with anti-HER2/PEG-SWNTs and receptor positive SKBR3 treated with only the PL-PEG-COOH modified SWNT (antibody-

free) are similar, showing very low intensity of G band, indicating extremely low level of non-specific binding. It is clear that very strong G band shows up only on the SKBR3 cells treated with anti-HER2/PEG-SWNTs, demonstrating that the noncovalent functionalized SWNTs have high selectivity for the cancer cells. Notice that the intensity of the G band is so strong that it is easily identified from the Raman backgrounds of the cell lines, which is in sharp contrast to that of the microwave functionalized SWNTs [5].

#### 6.2.4. Selective destruction of cancer cells

Six different samples were prepared and subjected to NIR radiation. The confocal fluorescence images after NIR radiation of the six samples are shown in Figure 6.5. The green color indicates that the cells are still alive and the red color indicates that the cells are dead. NIR radiation of both cell lines shows no effect on the cancer cells. In addition, adding only the antibody or the SWNT also have no effect of the cancer cells after NIR radiation. MCF7 cells were also treated with the anti-HER2/SWNT complex and irradiated with NIR light but the cancer cells remained alive. Only SKBR3 cells treated with the anti-HER2/SWNT complex showed the destruction of cancer cells after NIR radiation.

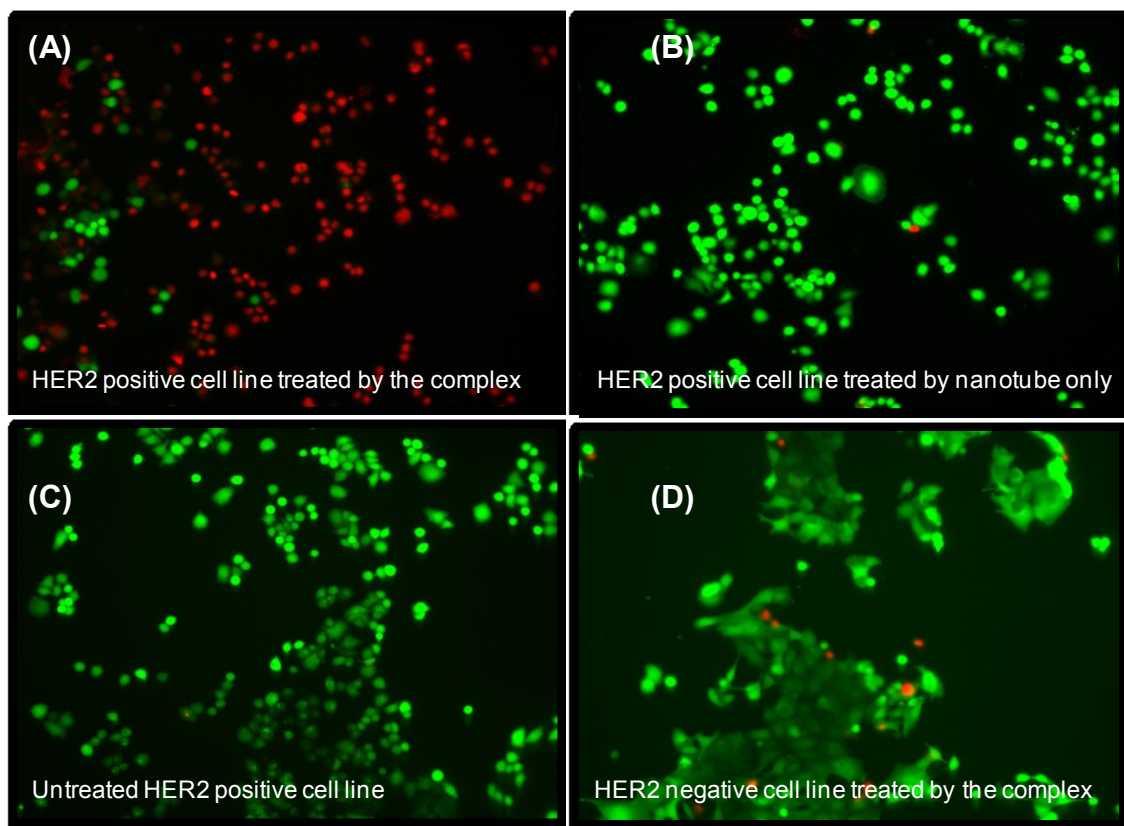


**Figure 6.5:** Fluorescence images of (a) SKBR3 cells treated with anti-HER2/SWNT complex (b) SKBR3 cells treated with PL-PEG-COOH/SWNT (no antibody), (c) untreated SKBR3 cells (d) Receptor negative MCF7 cells treated with anti-HER2/SWNT complex. Cells with green fluorescence are alive and cells with red fluorescence are dead.

## 6.3 Conclusion

In summary, preserving the electronic structure of SWNTs during dispersion and functionalization is critical for developing highly sensitive and selective sensors for early detection and selective destruction of cancer cells. In this work, the sensing complexes were constructed with a lipid-PEG polymer during the SWNT dispersion step. The PEG component not only imparts SWNT

water solubility, it also confers the dispersed SWNTs biocompatibility and the ability to prevent nonspecific binding or attachment of other big molecules such as proteins, large amount of which exist in vitro and in vivo environments. The sensing complexes developed in this work have large potentials for in vitro and in vivo applications for early cancer diagnosis.

## 6.4 Experimental

### 6.4.1. Reagents

*N*-Hydroxysulfosuccinimide sodium salt (NHS), *N*-(3-Dimethylaminopropyl)-*N*'-ethylcarbodiimide hydrochloride (EDC), MES hydrate buffer, were purchased from Aldrich and used as received without further purification. Highly purified single-walled carbon nanotubes (SWNTs) were prepared by the HiPCO process and obtained from Carbon Nanotechnologies. 1,2-distearoyl-*sn*-glycero-3-phosphoethanolamine-*N*-[carboxy(polyethylene glycol)-2000] (ammonium salt) (PL-PEG-COOH) was purchased from Avanti Polar Lipids Inc. All solutions were prepared using deionized water (18.2 M) (Nanopore water, Barnstead).

### 6.4.2. Dispersion of SWNTs into aqueous solution

SWNTs were dispersed into aqueous solution using a method previously described by Kam *et al.* [4]. Briefly, single walled carbon nanotubes were suspended in an aqueous solution containing PL-PEG-COOH. The mixture was sonicated using a Sonics Vibracell (Model VCX 130) for 90 minutes. The sonication process was performed in an ice-water bath to prevent local heating of the CNT which may cause unnecessary scission of CNT. After sonication, the sample was centrifuged using a Beckman J2-21 centrifuge (Eppendorf 5415C) at

6000rpm to remove insoluble materials, leaving PL-PEG-COOH dispersed single walled carbon nanotubes (PL-PEG-COOH/SWNT). The PL-PEG-COOH/SWNT solution was dialyzed using an Amicon Ultra-15 centrifugal filter (Millipore) with 0.1M MES buffer to adjust its pH to 4.5 prior to EDC coupling. The resulting solution consists of highly dispersed and functionalized PL-PEG-COOH/SWNT with a mass concentration of 200-400mg/L. The electronic structure of the dispersed PL-PEG-COOH/SWNT was characterized using UV-Visible spectroscopy.

### 6.4.3. Conjugation of anti-HER2 IgY antibody

Anti-HER2 igY antibody was conjugated onto SWNT surface by the following method: A solution of PL-PEG-COOH was mixed with NHS and EDC (2.5 to 1 ratio) in 0.1M MES buffer (pH 4.5). The mixture was incubated for 1hr at room temperature. The mixture was dialyzed with a Microcon YM-50 centrifugal filter unit (Millipore) to remove EDC, NHS, and other byproducts. The purified and carboxyl activated PL-PEG-COOH was then redissolved in 0.1M MES buffer solution (pH 6.3). Afterwards, anti-HER2 IgY antibody, which was prepared as described previously [13], was added into the mixture and allowed to react for 2hrs. The mixture was centrifuged at 18,000 g for 15 mins to remove unreacted materials. The precipitate was recovered and redissolved in 0.1M PBS buffer (pH 7.4). The result is anti-HER2 igY antibody functionalized SWNT (anti-

HER2/SWNT). The concentration of the antibody conjugated onto the SWNT surface was determined using BCA protein assay (Pierce, Rockford, IL) and was characterized using UV-Visible spectroscopy.

#### 6.4.4. NIR radiation of cancer cells using antibody/SWNT

Two different breast carcinoma cell lines were used, SKBR3 and MCF7. The samples were irradiated with a Spectra-Physics diode laser for 2 mins using a laser diode wavelength of 808nm at 5.0 W/cm<sup>2</sup>.

#### 6.4.5. Characterization

##### 6.4.4.1. Raman Spectroscopy

Raman spectra were acquired using a Kaiser Optical Systems Raman Microprobe. The spectra were collected using a 785nm diode laser over the range of 700-4000cm<sup>-1</sup>.

##### 6.4.4.2. Confocal laser scanning microscopy

Samples were obtained using a Confocal Fluorescence Microscope (Leica TCS SP5, DM6000). A 405nm diode laser was used as the excitation source.

## 6.5 References

1. O'Connell, M.J., et al., *Band Gap Fluorescence from Individual Single-Walled Carbon Nanotubes*. Science, 2002. **297**: p. 593-596.
2. Bachilo, S.M., et al., *Structure-Assigned Optical Spectra of Single-Walled Carbon Nanotubes*. Science, 2002. **298**: p. 2361-2366.
3. Cheung, W. and H.X. He, eds. *Carbon Nanotubes: In Vitro and In Vivo Sensing and Imaging*. Biosensor Nanomaterials, ed. S.J. Li, et al. 2011, WILEY-VCH Verlag GmbH & Co KGaA: Weinheim. 127-159.
4. Kam, N.W.S., et al., *Carbon Nanotubes as Multifunctional Biological Transporters and Near-Infrared Agents for Selective Cancer Cell Destruction*. Proc. Natl. Acad. Sci., 2005. **102**: p. 11600-11605.
5. Xiao, Y., et al., *Anti-HER2 IgY antibody-functionalized single-walled carbon nanotubes for detection and selective destruction of breast cancer cells*. BMC Cancer, 2009. **9**: p. 351-361.
6. Mews, A., et al., *Raman investigation of single oxidized carbon nanotubes*. Israel J. Chem., 2001. **41**: p. 15-22.
7. Irle, S., A. Mews, and K. Morokuma, *Theoretical study of structure and Raman spectra for models of carbon nanotubes in their pristine and oxidized forms*. J. Phys. Chem. A, 2002. **106**: p. 11973-11980.
8. Mews, A., et al., *Raman imaging of single carbon nanotubes*. Adv. Mater., 2000. **12**: p. 1210-1214.
9. Kneipp, K., et al., *Ultrasensitive Chemical Analysis by Raman Spectroscopy*. Chem. Rev., 1999. **99**: p. 2957-2975.
10. Takenobu, T., et al., *Stable and controlled amphoteric doping by encapsulation of organic molecules inside carbon nanotubes*. Nat. Mater., 2003. **2**: p. 683-688.
11. Wang, Y., Z. Iqbal, and S. Mitra, *Rapidly Functionalized, Water-Dispersed Carbon Nanotubes at High Concentration*. J. Am. Chem. Soc., 2006. **128**: p. 95-99.
12. Chen, R.J., et al., *Noncovalent functionalization of carbon nanotubes for highly specific electronic biosensors* Proc. Natl. Acad. Sci., 2003. **100**: p. 4894-4989.
13. Xiao, Y., et al., *Quantitation of HER2 and telomerase biomarkers in solid tumors with IgY antibodies and nanocrystal detection*. Int. J. Cancer, 2008. **122**: p. 2178-2186.



## Curriculum Vitae

Date of Birth                                      September 16, 1984

Place of Birth                                    New York, United States

### Educational Background

2002-2006                                      **State University of New York at Binghamton**

Degree obtained: B.A. in Chemistry

Degree obtained: B.A. in Mathematical Sciences

2006-2012                                      **Department of Chemistry, Rutgers University-Newark**

Degree sought: Ph.D. in Chemistry, Advisor: Huixin He

### Publications

- 1) Schadt, M. J.; **Cheung, W.**; Luo, J.; Zhong, C. J. Molecularly Tuned Size Selectivity in Thermal Processing of Gold Nanoparticles. *Chem. Mater.* **2006**, 18, 22, 5147-5149.
- 2) Ma, Y.; **Cheung, W.**; Wei, D.; Bogozzi, A.; Chiu, P.L.; Wang, L.; Pontoriero, F.; Mendelsohn, R.; He, H. Improved Conductivity of Carbon Nanotube Networks by In Situ Polymerization of a Thin Skin of Conducting Polymer. *ACS Nano* **2008**, 2, 6, 1197-1204.

- 3) **Cheung, W.**; Chiu, P.L.; Parajuli, R.R.; Ma, Y.; Ali, S.R.; He, H. Fabrication of high performance conducting polymer nanocomposites for biosensors and flexible electronics: summary of the multiple roles of DNA dispersed and functionalized single walled carbon nanotubes. *J. Mater. Chem.* **2009**, 19, 6465-6480.
- 4) Zhang, M.; Parajuli, R.R.; Mastrogiovanni, D.; Dai, B.; Lo, P.; **Cheung, W.**; Brukh, R.; Chiu, P.L.; Zhou, T.; Liu, Z.; Garfunkel, E.; He, H. Production of Graphene Sheets by Direct Dispersion with Aromatic Healing Agents. *Small.* **2010**, 6, 10, 1100-1107.
- 5) **Cheung, W.**; Pontoriero, F.; Taratula, O.; Chen, A.M.; He, H. DNA and carbon nanotubes as medicine. *Adv. Drug Deliv. Rev.* **2010**, 62, 6, 633-649.
- 6) **Cheung, W.**; He, H. "Carbon Nanotubes: In vitro and in vivo sensing and imaging" in Biosensor Nanomaterials. **2011** (book chapter)